UNIVERSIDAD DE BARCELONA
Facultad de Física
Departamento de Electrónica

ION BEAM SYNTHESIS OF SILICON-CARBON STRUCTURES AND RELATED MATERIALS

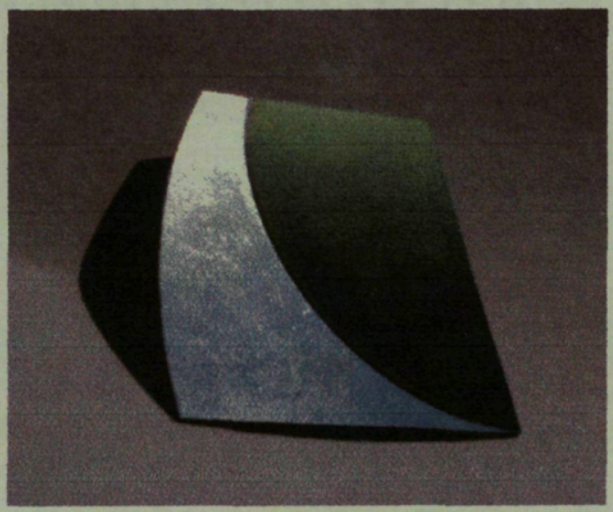

Lorenzo Calvo Barrio

UNIVERSIDAD DE BARCELONA
Facultad de Física
Departamento de Electrónica
Laboratorio de Ingeniería y Materiales Electrónicos

ION BEAM SYNTHESIS OF SILICON-CARBON STRUCTURES AND RELATED MATERIALS

Memoria presentada por Lorenzo Calvo Barrio
para optar al grado de Doctor en Física

Director de Tesis: Dr. Alejandro Pérez Rodríguez

Programa de doctorado:
Micro i Optoelectrónica Física (bienio 92/94)

Barcelona, Mayo de 1999

Deseo expresar mi gratitud hacia el Dr. Joan Ramon Morante, Director del Departamento de Electrónica, por haberme permitido disponer de todos los medios necesarios para la realización de este trabajo. Del mismo modo, expresar mi más profundo agradecimiento al Dr. Alejandro Pérez sin cuya constante dirección e inestimable ayuda no habría sido posible llevar a cabo esta tesis. También me gustaría mostrar mi reconocimiento a la labor de colaboración y consejo de los Drs. Albert Romano y Christophe Serre. A destacar la excelente colaboración con el Forschungzentrum Rossendorf de Dresden liderado por el Dr. Wolfang Skorupa. Por último, agradecer la simpatía y profesionalidad que en todo momento ha manifestado el personal de los Servicios Científico-Técnicos, donde se ha realizado gran parte de este trabajo.

No puedo acabar estas palabras de agradecimiento sin mencionar y agradecer el constante apoyo de aquellos que han estado más cerca en todo momento. A los amigos de facultad, que desde aquellos tiempos, año tras año, han vivido las anécdotas y vicisitudes de este trabajo. A los compañeros del departamento, con los que empecé y he seguido. Al reciente grupo de buenos amigos y compañeros de trabajo en los SCT. A mis padres, y a mi familia. Para Arantxa por todo y más (con un beso).

CONTENTS

PREFACE

The goal of this dissertation is the study and characterisation of high dose Carbon (C) implantation processes into Silicon (Si) and related materials for the synthesis of Silicon Carbide (SiC). The attainment of well-characterised multilayer structures useful to fabricate sensor and electronic devices based on them constitutes the main objective of this work.

SiC constitutes a very promising semiconductor, thermally and chemically stable with excellent physical properties, which has started to be successfully applied in some of the most outstanding fields in electronics. Electronic devices of SiC can operate at high temperatures, in chemically aggressive conditions and even under extreme radiation, dissipating heat excesses, and as a result, proportioning enormous benefits over electronic devices based on the other available semiconductors. Among the amount of applications, the optoelectronic, high temperature electronic, hard radiation electronic, high power and high frequency devices are worth remarking. Operable devices such as three colour LEDs, power MOSFETs, bipolar transistors, photodiodes or rectifiers have successfully been fabricated. Additionally, the high mechanical and chemical stability, and the high stiffness of SiC in relation to Si, are also interesting properties to develop complete Micro-Electro-Mechanical systems (MEMS), where sensing devices, signal processing and even actuators are integrated in the same substrate.

The synthesis of good quality and cheaper SiC structures is required to develop its technology. This implies the growth of SiC on the cheap and useful Si substrate. The traditional methods for obtaining SiC have been CVD and MBE, but some drawbacks such as the degree of reproducibility and the higher temperatures used in these processes can constitute a problem. In this sense, ion implantation constitutes a suitable alternative process for the direct synthesis of SiC, totally compatible with Si technology. This technique allows a high degree of control in the synthesis, offering enormous possibilities for obtaining complex structures.

By ion implantation, the properties of the synthesised material strongly depend on the implantation and annealing parameters. The perfect design of the implantation process will have repercussions on the characteristics of the resulting structure. Moreover, the amount of implanted C plays an important role in the way in which C is incorporated in the system. The incorporated C can take different places in de Si network, what will finally affect the structural characterisation of the synthesised material.

A complete group of analysis techniques has been used in order to characterise adequately the materials studied along this work. Among them, it may be mentioned the Raman and FTIR spectroscopies, mainly used in structural studies and to determine phases, XPS, which has allowed the measurement of the in-depth implanted C distribution and the study of the different bond configurations in the implanted layer, and finally TEM, which is used for the direct observation of the synthesised structures. The interpretation of all these data makes it possible to deep in the knowledge of the physical mechanisms involved in these processes.

As far as the contents are concerned, the thesis is structured in five chapters, each one containing its own references to other works. The introductory part, chapter 1, is divided in 3 sections. The first one contains all the basic data related to SiC. The second section deals with the ion implantation as a method of SiC synthesis. A description of the analysis techniques used along this work is presented in the last section.

Chapter 2 is devoted to the synthesis and recrystallisation of amorphous SiC. Previously, it has been studied the behaviour of the 6H-SiC commercially available in front of implantation processes, taking into account the role played by the temperature of implantation, the implanted dose and the temperature of annealing. Once performed this characterisation, the study of amorphous Si implanted with C at room temperature (RT) is carried out. The detailed disposition of existing chemical bonds as a function of the amount of introduced C has been an object of interest. Finally, the recrystallisation of this material by thermal processes and by IBIEC (a dynamic process that involves high-energy implantation) has been considered.

The direct synthesis of crystalline SiC by C implantation in a Si crystalline substrate is the subject of chapter 3. The procedure is to implant at a high enough temperature, 500°C, to avoid the Si amorphisation. This part of the chapter has been divided attending to the value of the implanted dose.

Firstly, samples implanted at doses below the threshold dose needed to reach a stoichiometric SiC composition at the implanted peak have been analysed. The study of these samples has allowed to characterise the main processes involved in the ion beam synthesis of crystalline SiC. Then, a multiple step implantation has been defined to obtain a continuous stoichiometric SiC layer. The analysis of the implanted samples has corroborated the formation of such a layer, with abrupt interfaces with the surface and substrate Si regions.

Chapter 3 finishes with a detailed study of the etch-stop properties of the ion beam synthesised layers. The excellent etch selectivity between these layers and the Si regions has allowed the fabrication of test micromechanic structures such as membranes, bridges and other self-standing simple structures. The attainment of these kinds of structures based on the ion beam synthesised layers constitutes an important conclusion, as it demonstrates its ability for the development of micromachined devices.

The study of the ion beam synthesis of SiC is extended to SiGe substrates in Chapter 4. In principle, the aim of this study is to improve the understanding of the mechanisms involved, in order to determine the influence of parameters such as the chemical composition, strain and bond length of the target material. Moreover, the possible modification of the synthesised phases by the incorporation of Ge atoms in a $Si_{1-x-y}Ge_xC_y$ ternary alloy is also investigated. This study is performed in a way similar to that previously done in Si. Firstly, the synthesis and recrystallisation of amorphous layers is investigated. After that, the analysis of high temperature processes in crystalline substrates is performed.

Finally, some general conclusions are written in chapter 5.

Preface

CHAPTER 1

INTRODUCTION

The aim of this introductory chapter is to expose the state of art of the field where this work is included, firstly presenting all the necessary previous knowledge, and secondly describing the different analytical techniques that have been used along the work.

The chapter begins with a comprehensive review of Carbon (C) into Silicon (Si) and other related materials. This work is mainly concerned with the study of SiC, so a special emphasis is given to this material. After this, some of the theory and technology associated with the Ion Implantation technique is introduced and illustrated with several data coming from the implantation machines used to obtain the samples studied in this work. A review of the fundamental ideas and works in the ion beam synthesis of SiC and related materials is also presented. This part can be considered a formal starting point to all the work. The section is closed with some comments on computational simulation of ion implantation by TRIM program.

A wide range of analytical techniques can be applied to characterise these complex materials and structures. Non destructive spectroscopies, such as Raman and FTIR, together with destructive techniques XPS and TEM are the most important. The introductory chapter also includes a description of these techniques, emphasising the principles they are based on and their technological configuration.

1.1 CARBON INTO SILICON AND RELATED MATERIALS

To introduce C by ion implantation in Si and other related group-IV materials allows to synthesise different useful structures, more or less stable depending on the optimisation of the technological parameters. In the following, SiC and C alloys are generically introduced, while the potential of the ion implantation technique for the synthesis of those materials will be exposed in the next section.

1.1.1 SILICON CARBIDE (SiC)

Natural SiC was isolated for the first time by Moissan in 1905 from an iron meteorite found in Canyon Diabolo, Arizona[1]. Although its constituents are abundant and the compound is chemically and thermally stable, large deposits of SiC have never been found. Since then, SiC has been studied and applied to very different industrial fields because of its outstanding physical properties. Nevertheless, the actual revolution promoted by this material happened when microelectronics proposed the possibility of the utilisation of SiC in devices working under extreme conditions.

The SiC processing is very complex, due to the pronounced tendency of SiC to crystallise into many different modifications, the so-called polytypes. However, the achievement of one or other polytype, allows to work with a certain range of band gap values. This useful electronic characteristic together with other remarkable properties makes SiC a material chosen for multiple device applications. The promising applications that are continuously appearing have motivating to go on developing and improving methods of growth, not only in bulk and epitaxial layers but also more complex structures where the SiC is buried and located in specific zones. However, synthesis as well as processing of SiC is complicated in comparison to other typical electronic materials such as Si, GaAs and other III-V compounds.

This section is divided in two parts. The first part gathers the sçtructure and properties of SiC, and the second part deals with its synthesis and the processing.

1.1.1.1 STRUCTURE AND PROPERTIES

SiC is the only chemically stable compound that forms in the binary phase diagram of the C/Si system[2]. It crystallises in a multitude of different modifications called polytypes[3]. Polytypism is a one-dimensional polymorphism or disorder that results from the stacking sequence. The building unit of all these polytypes consists of a close packed stacking of double layers of Si and C atoms. One set of atoms, Si or C, is shifted along the main axis of symmetry by a quarter of the distance between the nearest similar layers. The Si-C bonding is 88% covalent and 12% ionic with a distance between the Si and C atoms of 1.89 Amstrongs (A). Four C or Si atoms in strong tetrahedral sp^3-bond surround each Si or C atom. The tetrahedra are arranged in such a way that all the atoms lie in parallel planes on the nodes of regular hexagonal networks. The stacking of the double layers follows one of three possible relative positions, arbitrarily labelled A, B and C.

The only difference between the various polytypes is the stacking order of these elementary tetrahedra, being two basic sequences possible. If the projections of Si atoms in three successive layers are in three different positions, the only cubic structure also called 3C-SiC or β-SiC is formed. Then, this structure has a stacking sequence of ABCABC... On the other hand, a hexagonal or rhombohedral lattice results from the coincidence of the projection of the atoms in the third Si layer with the position of the Si atoms in the first one. The appearance of one structure or another depends on the exact stacking order. In fact, more than 250 different polytypes have been reported to exist, being the most common structures the cubic β-SiC, and both hexagonal 6H-SiC and 4H-SiC. Figure 1.1 tries to visually represent all these crystallographic concepts.

Some of the basic physical properties of SiC are the following[4]. Density at Room Temperature (RT) density ranges from 3.166 to 3.249 $g \cdot cm^{-3}$ depending on the polytype. The lattice parameter 'a' is 4.3596A for the cubic structure, while 6H structure has lattice parameters 'a' of 3.0806A and 'c' of 15.1173A. The acoustic velocity is of about 1300 m/s, and the value of the Young's modulus is 445 GPa for a 2mm thick free-standing cantilever.

As it has already been mentioned, the physical and electronic properties of SiC make it the foremost semiconductor material for different devices. An appreciation of this potential can be gained by examining Table I-I, in which some relevant properties of both hexagonal (6H, 4H) and cubic SiC are compared with other popular semiconductors such as Si, GaAs and diamond.

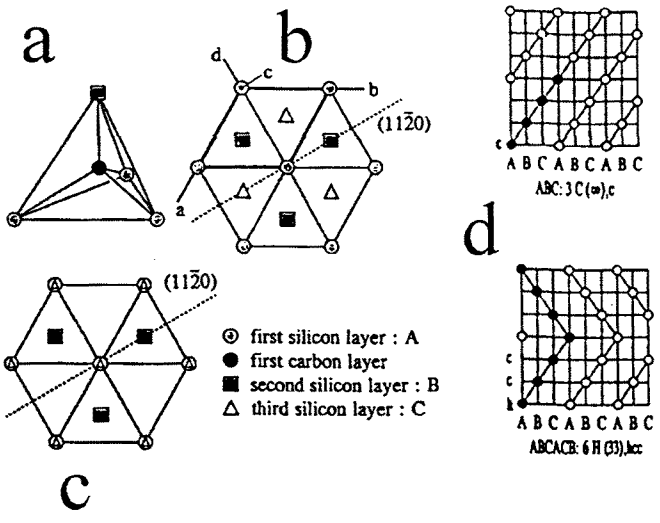

Figure 1.1 (a) Elementary SiC-tetrahedron and (b) projection of the different positions of the Si atoms in the cubic structure, (c) and the hexagonal structure. (d) Position of Si atoms in planes where all relevant atoms lie for both cubic and hexagonal (6H) polytypes.

To summarise the ideas contained in the table, the electronic devices formed in SiC can operate at very high temperatures without suffering from intrinsic conduction effects because of the wide energy band gap. Also, this characteristic allows the emission of high-energy wavelength light, for instance blue light. Its excellent chemical stability allows SiC to work under very chemically aggressive environments, even under extreme radiation. Apart from that, SiC can withstand an electric field over 8 times greater than Si or GaAs without undergoing avalanche breakdown. This high breakdown electric field enables the fabrication of very high-voltage, high-power devices such as diodes or power transistors. Additionally, the devices can be placed very close together, providing a high device packing density for integrated circuits.

On the other hand, SiC is an excellent thermal conductor. Heat will flow more readily through SiC than through any other semiconductor material. In fact, SiC has a higher thermal conductivity at RT than any metal. This feature enables devices to operate at high power levels and still being capable of dissipating the large amount of generated heat. Finally, because of their high saturated electron drift velocity, SiC devices can operate at high frequencies (microwave).

PROPERTY	Si	GaAs	Diamond	3C-SiC	6H-SiC	4H-SiC
Band gap (eV)	1.1	1.42	5.5	2.3	3.0	3.2
Melting Point (K)	1690	1510	Phase change	Sublimes	>2100	> 2100
Physical and Chemical stability	Good	Fair	Very Good	Excellent	Excellent	Excellent
e-mobility (cm^2/Vs)	1100	6000	2200	750	370	800
h-mobility (cm^2/Vs)	420	320	1600	40	90	115
Breakdown voltage (10^6 V/cm)	0.6	0.6	10	2	3.2	3
Thermal conductivity (W/cm·K)	1.5	0.5	20	4.9	4.9	5
Sat. electron drift velocity (10^7 cm/s)	1	2	2.7	2.5	2	2
Dielectric constant (K)	11.8	12.8	5.5	9.7	9.6	10.3

Table I-1 Comparison of important semiconductor properties at RT.

Collectively, these properties make SiC devices to have tremendous benefits over other available semiconductor devices in a large number of industrial device applications[5], which will be reported in the following section.

1.1.1.2 SYNTHESIS AND PROCESSING

Initially, large-scale synthesis of SiC was mainly done from non-stoichiometric Si-C melts by vapour grow processes or sublimation. However, melt growth processes are complicated because of the small C solubility in Si at temperatures below 2000°C as well as its small change with temperature and the high vapour pressure of Si, in the order of 0.1atm at this temperature. As a consequence, high temperature processes are necessary and the SiC grown by this method is not adequate for practical applications because of its size, quality and purity. On the other hand, sublimation processes were reported firstly by Lely[6] in 1955, as good methods to obtain higher purity bulk SiC single crystals. Since then, the technique has continuously improved and, at present, the types of 6H and 4H polytypes produced can be controlled by the growth temperature, making it possible to obtain 2 and 3 inches high purity commercial wafers[7].

Although significant advances have been achieved in the field of bulk crystal growth, the wafers still contain a great variety of defects. Among the problems to be solved, the investigation of the relationship between the occurrence and concentration of these defects and the kind of polytype, as well as the effect of the growth parameters on the concentration of defects, are of fundamental interest. The high density of defects together with the small size and the high prices of commercially available wafers constitute severe drawbacks that have to be solved before the SiC possibilities could be fully exploited.

The growing of SiC single crystal films on other substrates constitutes an alternative and interesting approach. In principle, this would allow the fabrication of β-SiC films with the potential advantage of the lower price of the different substrates, for instance Si. However, several problems arise in obtaining SiC on Si, being remarkable the degradation of the crystalline quality due to the lattice mismatch and the formation of Si voids at the SiC/Si interface. In this sense, the chiefly technique[8] for growing SiC films on Si is, at present, chemical vapour deposition (CVD). Typical sources are high purity Silane and Propane. Usually, the deposition is carried out by the simultaneous flow of gases at atmospheric pressure and at a temperature ranging from 1100°C to 1600°C.

Another promising way of producing SiC epitaxial layers seems to be molecular beam epitaxy (MBE). This technique has a number of advantages compared to CVD, such as lower growth temperatures (<1100°C), clean growth ambient (UHV conditions) and layer by layer deposition[9].

The first MBE experiments were done by gas source (GSMBE), using disilane and acetylene gas molecular beams. However, the strong absorption and incorporation of atomic H at low temperature produced by the decomposition of the gas phase reactants lead to lattice imperfections. Thus, the growth rate has to be lower than the H desorption rate, which implies very low deposition rates.

A different approach to produce SiC is sputtering, being of special interest when two targets of both Si and C are used. This way of production can contribute to a free-hydrogen amorphous or polycrystalline layer, but great efforts need to be made to control and select the characteristics of the materials by the sputtering conditions[10].

Finally, high-dose C implantation into Si in combination with either subsequent or in situ annealing can produce β-SiC layers[11]. The versatility of this technique allows a high degree of control of the process, making possible the direct synthesis of a complex multilayer structure. Depending on the implanted and annealing conditions, high crystalline quality material can be synthesised. In next section, properties of the material obtained by ion implantation will be reviewed in detail.

As far as the SiC processing is concerned, some material properties make it rather complex. Thermal oxidation or HCl etching is commonly used to remove surface damage. The formation of patterned structures is done by plasma-based dry etching processes in combination with lithography, such as reactive ion etching (RIE) due to the extremely high chemical stability of SiC. A combination of ion beam induced amorphization and wet chemical etching can also be used for patterning, but this method has hardly been systematically investigated. For the future, ion induced sputtering, either with suitable mask or maskless, seems to be a research field of interest[12].

With respect to the ohmic contact formation, transition metals forming silicides or carbides give the best results. However, reproducibility is poor, playing a tremendous role the surface quality. High level surface doping of the substrate by ion implantation may bring further success. Moreover, selective doping by diffusion is hardly applicable due to the small diffusion coefficients of the dopants in SiC and the high temperature required. Ion implantation is a good alternative, but the connection between residual defects and the resulting properties, as well as the reduction of these defects in order to optimise the processing parameters, should be more investigated[13]. Although high temperature implantation allows a significant decrease of residual damage, the efficient removal of the damage still needs a high temperature annealing of 1500 °C or even higher.

OPTOELECTRONICS
Applications: air quality monitoring equipment, UV spectroscopy, dosimetry and solid state flame detectors for combustion control, light emitting diodes, incoming ballistic missile detection and imaging. Benefits: great responsitivity, sensitivity and efficiency under hard operating condition.
HIGH TEMPERATURE ELECTRONICS
Applications: automotive sensors, jet engine and industrial process measurement, control instrumentation, spacecraft power conditioning electronics and sensors. Benefits: sensor output signal amplification, reduce need for cooling, reliable sensing and control in aggressive and not current environments, improve device reliability.
RADIATION HARD ELECTRONICS
Applications: signal amplification and processing, defence and space based nuclear power, power circuits analogue multiplexing, low resolution A/D and D/A conversion. Benefits: more resistant to neutron and gamma radiation than Si devices.
HIGH POWER/HIGH FREQUENCY DEVICES
Applications: electronic for space power systems, smart actuators, power generation systems, automotive electronics, communication systems, high frequency power supplies and military industry. Benefits: more devices per unit area and power density respect to Si devices, reduced system volume, weight and cooling requirements, excellent transient characteristics.

Table I-II Applications notes of 6H-SiC

To end this section, it is interesting to mention some of the numerous electronic applications that have been proposed based on SiC's basic properties, being the four foremost: optoelectronic devices, high temperature electronics, radiation hard electronics and high power/high frequency devices. Operable devices such as three colour light emitting diodes (LEDs), power MOSFETs, bipolar transistors, photodiodes or rectifiers have been fabricated successfully by different companies with both 6H-SiC and 3C-SiC. In particular, CREE industry proposes different actual applications on these fields[14]. It seems clarifying to gather them and their benefits the table I-II.

In addition to this, the high mechanical and chemical stability and high stiffness of SiC in relation to Si are also interesting to obtain a material to develop complete Micro-Electro-Mechanical systems (MEMS), where sensing devices, signal processing and even actuators are integrated in the same substrate. In this sense, SiC has been reported to be an interesting material for sensing devices such as pressure and gas sensors, and different devices have already been fabricated and demonstrated[15-19].

1.1.2 SILICON BASED ALLOYS: $Si_{1-y}C_y$ AND $Si_{1-x-y}Ge_xC_y$

Band gap engineering in semiconductor structures through group IV alloying has recently shown great technological promise for the fabrication of high performance electronic devices. In this respect, significant advances have been made in the growth of new binary and ternary materials such as Si, Ge and $Si_{1-x}Ge_x$ strained layers alloyed with small quantities of C. The addition of C into Si or $Si_{1-x}Ge_x$, layers leads to a new degree of freedom in manipulating mechanical and electrical properties. Before considering the topic of these new compounds, it may be useful to comment briefly on the Si/Ge binary system.

The Si/Ge system is of particular interest due to the possibility of modifying the band gap and band offsets to Si, controlling the strain and the layer composition[20]. Various growth techniques such as CVD and MBE are currently being employed to produce epitaxial $Si_{1-x}Ge_x$ films on Si. Alternatively, it is possible to produce SiGe alloys by implanting Ge in preamorphised Si and, subsequently, making a solid phase epitaxial growth (SPEG).

Si and Ge are fully miscible and form an almost ideal solid solution, with an enthalpy of formation of 0.034 eV per bond. Both Si and Ge share a common crystal structure, the diamond cubic lattice, but they do not have the same lattice parameter. According to Vegard's law, the lattice constant of $Si_{1-x}Ge_x$ alloy is given by,

$$a_{SiGe_x} = (1-x)\cdot a_{Si} + x \cdot a_{Ge}$$

and it goes from 5.431 A (x=0) to 5.657 A (x=1). Consequently, the alloy cannot be grown epitaxially on a Si substrate, and initially tends to adapt it in-plane lattice constant in such a way to form a coherent interface with the substrate. This type of growth is referred to as pseudomorphic or commensurate growth. The lattice space along the direction of growth, perpendicular to the interface, $a_{\perp}$, is larger than the lattice spacing parallel to the interface, $a_{\parallel}$, which is given by the lattice constant of the Si substrate for a fully strained layer. Both parameters are related to the elastic constant of the material. The compressive biaxial strain of the layer is determined by the following expression,

$$\varepsilon_{\parallel} = \frac{a_{\parallel} - a_{SiGe}}{a_{SiGe}}$$

where a_{SiGe} is the above mentioned lattice constant for the SiGe fully-relaxed layer. This corresponds to the lattice constant of the crystal in the absence of strain, and it is given by,

$$a_{SiGe} = a_{\perp}\left(1 - \frac{2\nu}{1+\nu}\frac{a_{\perp} - a_{\parallel}}{a_{\perp}}\right)$$

where ν is the Poisson coefficient of the material. Moreover, the lattice mismatch, m, is defined as,

$$m = \frac{a_{SiGe} - a_{Si}}{a_{Si}}$$

Taking into account all previous data, the epitaxial SiGe layers grown on Si can be under a considerable compressive strain. The inherent strain and the composition of the pseudomorphic $Si_{1-x}Ge_x$ layers affect strongly the band structure, the nature of conduction and the band offsets.

Moreover, because of the strain, the alloyed layers are stable only to a certain equilibrium thickness (for instance with x=0.2 up to t=200A), beyond which they become metastable and tend to relax during post-growth heat treatments. The chief mechanism of strain relief is via formation of misfit dislocations at the alloy/substrate interface. Clearly, the dislocations will have adverse effects on device performance and reliability.

Therefore, it is of high technological importance to find effective means of reducing the strain and increasing the mechanical stability of these heterostructures. Strain relaxation is conventionally achieved by growing $Si_{1-x}Ge_x$ layers on a graded buffer layer.

A promising alternative of overcoming the strain-related problems of the $Si_{1-x}Ge_x$ layers is by introducing C atoms. C has low bulk solubility in Si and Ge (in the order of 10^{17} atoms/cm^3) and, as the C covalent radius is much smaller than the one for Si (0.77A for 1.17A), the alloy containing Ge may be lead almost strain counterbalancing[21]. In fact, for a Ge:C ratio of 8.3, the lattice constant in the direction of growth proves to be equal to that of the Si substrate, which is indicative of a lack of macroscopic strain. In this case, the alloy layer will have the diamond cubic structure of Si.

A deeper understanding of C role in the formation of strain-compensated $Si_{1-x-y}Ge_xC_y$ alloys has been gained by studying the behaviour of highly saturated substitutional C in Si, and the properties of the resulting tensile-strained $Si_{1-y}C_y$ layers. It must be pointed out that the formation of a $Si_{1-y}C_y$ compound with y different from 0.5 is thermodynamically impossible, according to the C/Si phase diagram, and therefore can be achieved only via non-equilibrium processes such as MBE, CVD or ion implantation. As the mismatch between Si and C is about ten times larger than between Si and Ge, very small amounts of C are sufficient to achieve discernible strain. Layers with substitutional C contents up to 3% have been obtained. For higher C contents, the strain accumulation in the lattice around C atoms is too high and this probably prevents the incorporation of C in the Si lattices, promoting formation of C complexes and even SiC precipitates. Precipitation of C as SiC also limits the thermal yield. For processing temperatures of T>800°C, relaxation of $Si_{1-x-y}Ge_xC_y$ layers has been observed, related to the diffusion of substitutional C to instertitial positions and the SiC precipitation[22].

1.2 ION IMPLANTATION OF CARBON

Ion implantation is an outstanding technique to dope materials, to obtain useful structures and to synthesise new and interesting compounds. Particularly, by introducing C in Si and related materials it is possible to make up different structures such as $Si_{1-y}C_y$ and $Si_{1-x}Ge_xC_y$ alloys and SiC stoichiometric layers on Si substrate, which might be useful for different electronic and sensor applications.

This section is organised as follows. Firstly, for a better comprehension of the work, the basis of ion implantation is presented, together with some comments about technological characteristics of the used implant machines. Secondly, the knowledge about ion beam synthesis of SiC is reviewed, covering with particular emphasis the attempts to get the material with substoichiometric and stoichiometric C content. Finally, the last section deals with the simulator program that reaches the first approximation to the distribution of implanted ions in the target material.

1.2.1 THEORY AND TECHNOLOGY

In the ion implantation technique, the material surface is bombarded with a beam of previously accelerated ions, under vacuum conditions. Acceleration energies range from a few keV to some MeV. As a result, a great part of the incident ions goes into the material up to a certain depth. While penetrating, the ions are basically stopped by two mechanisms: inelastic electronic collisions and elastic nuclear collisions.

In the inelastic collisions, the incident ions lose their energy via the ionisation of the atoms of the target, which is usually a crystalline structure. The movement direction of the ions is almost not affected by this kind of collision. On the other hand, ions also lose their energy via elastic collisions with the atom nucleii in the crystalline network. This process changes the ion direction drastically. In fact, ions are dispersed randomly in an actual amorphous target, or identically, in a crystal whose crystallographic direction has been deflected with respect to the implanted direction.

Moreover, in these conditions, the atoms that have been collided are moved from their network positions, originating intrinsic defects such as vacancies, interstitials and antisites. These displaced atoms also generate secondary collisions with the network atoms, which lead to the generation of a cascade of secondary defects related to the implant process.

Both mechanisms, inelastic electronic and elastic nuclear collisions, occur at different energies. The inelastic mechanism is dominant at higher energies, typically in the order of hundreds of keV, while the elastic one predominates at lower energies. As the process also depends on the mass of the incident ions, it is possible to establish a critical energy E_c related to the ion mass, which marks the boundary between the mechanisms[23].

Figure 1.2 schematically represents the movement of an implanted ion inside an amorphous or a randomly oriented crystalline solid. The way of a high energetic ion essentially is a right line up to the end where some degree of dispersion exists because of the nuclear collisions. On the other hand, moderated ion energies led to trajectories with more dispersion as a consequence of the sharing out of the loss energy between mechanisms, the nuclear and the electronic one. So, a certain distribution of the implanted ions exists in both cases.

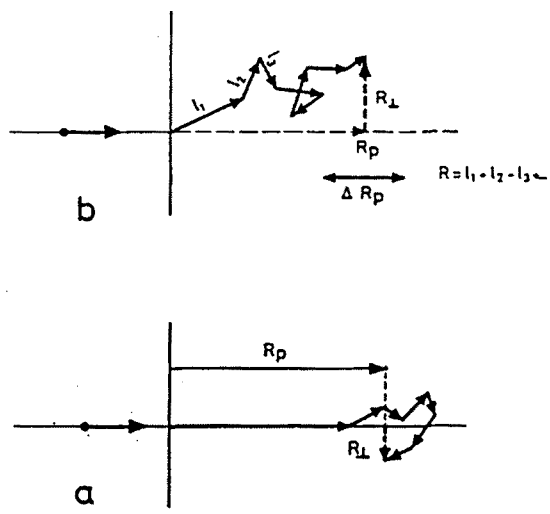

Figure 1.2 Trajectories of high-energy (a) and moderated energy (b) ions inside a random oriented solid.

In a first approach, the ion distribution can be estimated by a model based on the Bohr's theory and developed by Lindhard, Scharff and Schiott[24-25]. This is known as the LSS model of ion implantation, and allows to estimate the main parameters that characterise any implantation such as all the trajectory of the ion inside the solid, R, and its projections in the incident and perpendicular directions, R_p and $R_\perp$. These parameters are known as the implantation ranges.

As the loss energy mechanisms are independent, R can be written as the average distance gone over the target by an ion with an incident energy, E_i,

$$R = \frac{1}{N}\int_{E_i}^{0} \frac{dE}{S_n(E) + S_e(E)}$$

where N is the atomic concentration of the target, $S_n(E)$ and $S_e(E)$ are the stopping powers due to the nuclei and the electronic gas, and E_i is the incident energy of the ion. The nuclear stopping power, $S_n(E)$, can be calculated from a classical description of the two-particles interaction process, considering a Coulomb interaction potential affected by a blinded function. This blinded function is based on the statistical Thomas-Fermi model[26]. For the electronic stopping power, $S_e(E)$, the model supposes a quasi-classical law similar to the stopping law in a viscous medium, which is proportional to the quadratic root of the energy.

Taking into account these models, the final result indicates that R and its projection R_p, also known as the projected range, are practically proportional to the incident energy of the ion, E_i. R_p can be interpreted as the average penetration depth in the solid. In a first approach, the distribution of implanted atoms, n(x), can be described by a gaussian function,

$$n(x) = n(R_p)\cdot \exp\left(-\frac{(x-R_p)^2}{2\Delta R_p^{\,2}}\right)$$

where ΔR_p^2 is the average quadratic (or the standard) deviation of the projected range. ΔR_p is known as the straggling. The implanted dose, ϕ, corresponds to the number of ions introduced into the solid per unit area,

$$\phi = \int_0^\infty n(x)dx$$

Using this expression, the maximum concentration of implanted atoms is given by,

$$n(R_p) = \frac{\phi}{\sqrt{2\pi}\Delta R_p}$$

This model gives an accurate approximation of the distribution of the implanted atoms around the implanted peak. However, some twists can appear due to channelling effects, which happen when the ions move into crystallographic directions and are channelled in directions with low density of host atoms. This leads to a reduction in the number of collisions of the ions with the atoms and hence, to a deeper penetration in the solid. This problem can be solved by choosing the angle of implantation adequately. By this way, for the incident beam of implanted ions the distribution of host atoms appears as random and the possibility of channelling of the ions is drastically reduced.

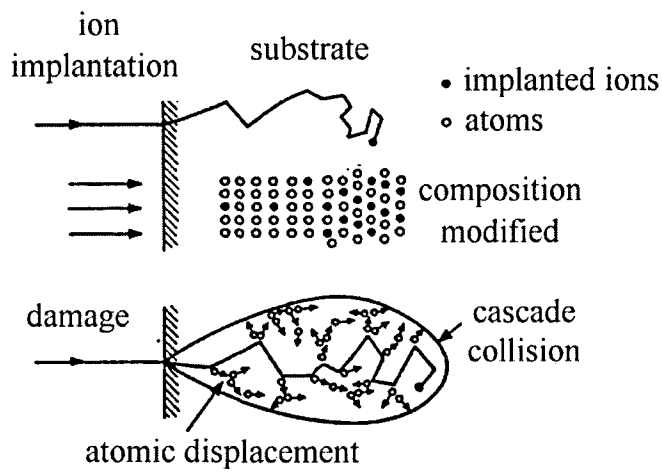

Figure 1.3 Damage and compositional effects in the implanted substrate.

It is important to distinguish between two different effects of the implantation over the material. The first one is the fact that some damage or network modification is created as a consequence of the implantation, visually explained in figure 1.3. The second one is that the implanted specimen can place various positions in the network, such as substitutional or interstitial sites, and can also create aggregates or clusters depending on energetic considerations.

Among the possible types of defects introduced in the network by the implanted ions, vacancies, interstitials and antisites are the most important. While vacancies are the absence of atoms in a network junction, interstitials are the atoms moved up to no-junction positions. Antisites happen in composed structures, where displaced atoms are placing positions that belong to other chemical species. An increase in the implanted dose leads to an increase in the density of defects in the damaged region, and above a certain threshold dose value, amorphisation of the network occurs. In this way, by implanting at high enough doses the substrate can be completely amorphised. The atoms that have been displaced will need an extra energy to return to their stable places in the ordered network. Usually, this energetic recuperation is given by a subsequent thermal treatment, by annealing in a conventional furnace or a more modern Rapid Thermal system.

Ion implantation constitutes one of the main techniques for doping in microelectronic technologies. The distribution of implanted ions is mainly determined by their energy and dose. The damage in the implanted layer can be minimised by increasing the temperature of the substrate during the implantation, although post-implant anneals are currently used to recover from the implant damage and to electrically activate the implanted impurities. Among the advantages of the implantation processes, it has to be pointed out the possibility of a more exact doping even for low concentrations, because of the simplicity for controlling both the incident ion flux and the implantation time. Also, by varying the beam energy, it is possible to control the depth penetration and, together with some dose variations, to produce complex profiles in an easy way. Finally, all elements can be implanted, and the lateral diffusion of implantation is uniform and independent of depth.

Moreover, ion implantation can also be used for the synthesis of complex structures and compounds. When the concentration of the implanted ions exceeds the solubility in the host material, precipitation occurs. In this case, precipitates can be elemental, such as metals in Si, or compounds resulting from the chemical reaction between the implanted ions and the host atoms. This allows the ion beam synthesis of chemical compounds in the host material. By increasing the implanted dose, the concentration and size of precipitates increases, and there is a threshold value above which a continuous layer is formed. For a compound layer, this threshold corresponds to the dose for which a stoichiometric composition is achieved at the implanted peak. Further increase of the dose above the threshold value leads to an increase in the thickness of the compound layer.

The strong flexibility of the ion implantation technique has allowed the synthesis of a wide range of compounds and structures in different substrates, which are summarised in the table I-III[27-33].

TARGET ION	Si	Al	SiO_2	Al_2O_3
O	SiO_2			
N	Si_3N_4	AlN		
O/N			Oxinitrides	
C	SiC			
Metals	Silicides			
Si/Ge			$SiGe_x$	$SiGe_x$
Ga/As	GaAs		GaAs	
In/As	InAs		InAs	
Ga/P	GaP		GaP	
In/P			InP	
Cd/S			CdS	CdS
Cd/Se			CdSe	CdSe
Cd/S/Se			$CdSe_xS_{1-x}$	
Ga/N				GaN
Ti/N			TiN	

Table I-III Main compound synthesis by ion implantation[27-33].

Up to now, the main application of ion beam synthesis has been the fabrication of Silicon-On-Insulator (SOI) structures. SOI substrates can be obtained by implantation of O^+ ions in a Si substrate, and by a subsequent annealing. This technology is known as SIMOX, Separation by Implanted Oxygen. SIMOX wafers are commercially available and are characterised by a high crystalline quality of the top Si film with low density of defects and very abrupt interfaces between the Si and SiO_2 layers.

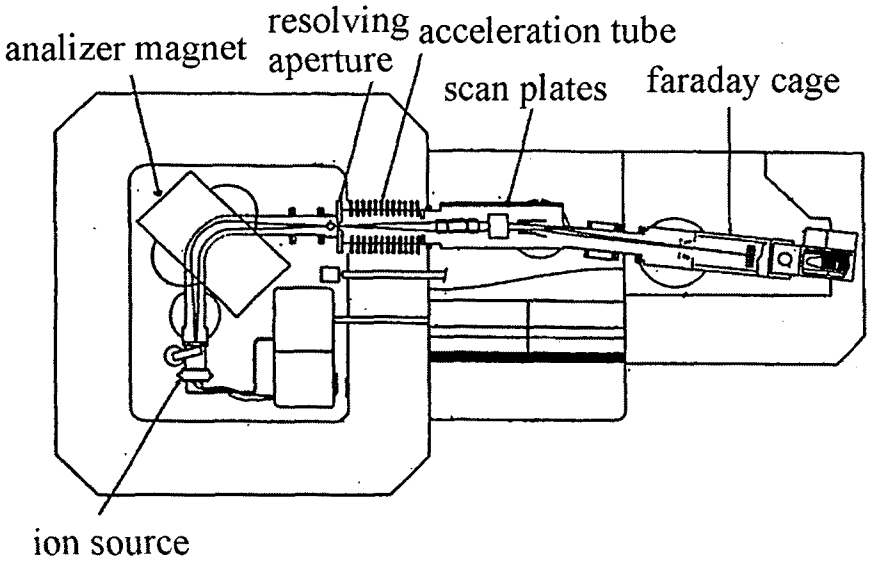

Figure 1.4 Basic scheme of an ion accelerator.

To finish this section, some data about the experimental equipment used in this technique are given. Although very different options can be selected, the implant machines are basically constituted by the elements shown in figure 1.4.

First of all, a gaseous source of appropriate material at high accelerating potential is needed to form the ion beam. An adjustable valve controls the flow of gas to the ion source. A power supply provides energy to the ion source, also at a high potential. The ion source contains ion plasma with the species of interest. A source diffusion pump establishes a low enough pressure for the beam transport with reduced ion-gas scattering. Usually, the implanted element is introduced as a gas, but there is also some furnace equipment to sublimate the solid elements.

The implanted element is ionised by electronic discharge. A low negative potential accelerates the positive ions. The selection of the chosen ions from the wide range of ions present in the source is made by magnetic prisms built in 90° angular sector. The adjustable analyser magnet can select only the ion species of interest and rejects the others, only by varying the intensity of the prism bobbins. It can also increase the amount of ions formed.

The desired ion species pass through a resolving slit or aperture and are injected into the accelerator column. Through the acceleration tube and thanks to an electrical raster composed by x and y deflection scan plates, the beam is ready to reach the target in a uniform way.

The target chamber consists of an area-defining aperture, a Faraday cage and finally a wafer feed mechanism. The Faraday cage allows the precise control over the implanted dose, which is calculated as the implanted flux multiplied by the time of implantation. The flux, ϕ, can be known by the geometric characteristics of the box as the surface of the in-diagram, S, and by the Faraday current in microamperes, I_F,

$$\phi\left(\frac{ion}{cm^2 s}\right) = \frac{I_F}{S \cdot 1.6 \cdot 10^{-19}}$$

Moreover, sometimes together with the Faraday cage there is a retarding field because low energies are necessary to implant some light elements.

Finally, in relation to the technology used in this work, different R+D centres have been involved: ForschungZentrum Rossendord, FZR (Dresden, Germany)[34], Asociación de la Industria Navarra, AIN (Pamplona, Spain)[35] and Centro Nacional de Microelectrónica, CNM (Barcelona, Spain)[36]. Plan Nacional de Materiales (CYCIT), Acciones Integradas Hispano-Alemanas and European Materials Research Society Network III have been the used frameworks of collaboration between these centres and EME laboratory. The implantation processes have been mainly performed at the Forschungzentrum Rossendord. Different implant machines have been used depending on the desired energy, dose and beam current. A High Voltage Engineering Europe 500 keV implant machine, with a hot filament Nielsen source and electrostatical beam scanning, has been used to implant at energies higher than 200 keV and maximum current densities lower than 50 microamperes. On the other hand, the Danfisik 200 keV implanter with a slow magnetic beam scanning allows energies lower than 200 keV and maximum current densities close to 1mA. In both cases, target heating is possible. Moreover, all the implantations have been performed at 7° to minimise the channelling effects.

1.2.2 CARBON IMPLANTATION INTO SILICON: ION BEAM SYNTHESIS OF SiC

This section will focus on reviewing the major aspects and the current understanding of the effects caused by the implantation of C in Si. Studies of this topic can be separated into three somewhat overlapping areas. Firstly, those where the C content is up to or slightly exceeds the equilibrium solid solubility limit. Secondly, those where the C concentration is well above this limit but still below the stoichiometric ratio for SiC. Finally, those where the C volume concentration is high enough to form stoichiometric SiC layers.

Taking C as impurity in bulk Si, just in the first case above mentioned, some basic and interesting physical and chemical characteristics are summarised in tables I-IV, I-V and I-VI. Like Si, C is isovalent (valency 4) with valence electron $2s^2 2p^2$, but it is smaller, more electronegative and chemically reactive. Therefore, C readily tends to incorporate into the Si lattice forming bonds with atoms, possibly in defect complexes, with impurities or by interactions with point defects, due to the reduction of bond length respect to the Si-Si bond. The character of C bonds will be considerably ionic, due to the C high electronegativity. The C solid solubility in bulk Si is quite low, probably because of the strain field induced by its small size. At a given temperature, precipitation occurs when the impurity concentration is higher than the solubility limit and the duration of the heat treatment is long enough. Depending on the phase diagram the equilibrium configuration is either in the form of a precipitate of the natural valency compound or as a pure precipitant.

Atom	Phases	Electronegativity	Covalent radius (A)
C	Graphite/Diamond	6.26	0.77
Si	Diamond	4.80	1.17

Table I-IV Structure of the stable phases, electronegativity, and covalent radius.

Atom	E_i (eV)	U_0 (eV)	E_g (eV)
C	11.26	7.37	5.5
Si	8.15	4.63	1.17

Table I-V First ionisation energy E_i, cohesive energy U_0 and band gap E_g of C and Si.

Bonds	Length (A)	Energy (eV)
C-C	1.43	6.42
C-Si	1.88	3.21
Si-Si	2.35	2.35

Table I-VI Length and energy of some bonds of interest.

Low amounts of C normally occupy substitutional (tetrahedral) sites, although lattice distortion and the presence of defect complexes may result in other configurations being favoured. Covalent C radius is smaller than that of Si and, in the case of a true substitutional location, this leads to a decrease in the lattice constant corresponding to the lattice contraction of about one atomic volume for each C atom incorporated. Lattice contraction may occur only in the case of substitutional dopants whose atomic size is smaller than that of Si, whereas lattice expansion can take place with dopants of larger radius on both substitutional and interstitial sites, as well as, with impurities of smaller radius occupying interstitial sites.

The diffusivity of substitutional C is intermediate with respect to some other elements and point defects in Si. The relatively high activation energy of diffusion and the fact that C is an electrically neutral impurity can both be taken as additional pieces of evidence that the C atoms are mainly located on substitutional lattice sites. Due to this substitutional position, C requires the presence of point defects to diffuse. Moreover, C diffusivity has been shown to be concentration-independent. The high diffusivity of C compared with the Si self-diffusivity implies that C diffuses either via a highly mobile C/self-interstitial complex (CSi_i),

$$C_s + Si_i = (CSi_i)$$

where C_s denotes a substitutional C atom and Si_i is an interstitial Si, or through a kick-out mechanism, involving a highly mobile interstitial C, C_i, whose activation energy for migration is 0.38 eV,

$$C_s + Si_i = C_i$$

C precipitation in Si could result in the formation of crystalline SiC. This process, however, is only possible in a Si_i supersaturation environment, which points towards the existence of a barrier to the initiation of C precipitation, and thus being necessary a nucleation step. Segregation proceeds on a microscopic scale to form very small SiC precipitates. As an alternative to SiC formation, depending on the interface and strain energies, a simple pile-up of C atoms in the form of loose C-Si agglomerates may also take place. Both processes lead to a volume reduction by a factor two, as it is shown in figure 1.5, and are accompanied by absorption of Si_i or emission of Si vacancies (Si_v)[37-38].

The complex nature of the structures resulting from a high-dose C implantation before and after annealing is dealt with in the following[11]. The idea is to present the state of the art for the studies on C implanted Si that fall within the concentration range between the solubility limit and the stoichiometric ratio for SiC. The tendency of C, being a comparatively light ion, is to produce buried amorphous, carbon-rich layers when implanted at moderate energies and doses. The formation of carbon-depleted zones is due to the diffusion of C from the near surface region into the amorphous carbon-rich layer. For energies high enough to form such a layer, the radiation damage after the appropriate annealing is confined to a narrow region, and the superficial Si layer is of high single-crystal quality. The C near-surface concentration can be reduced to values similar to those of the C solid solubility limit in virgin Si.

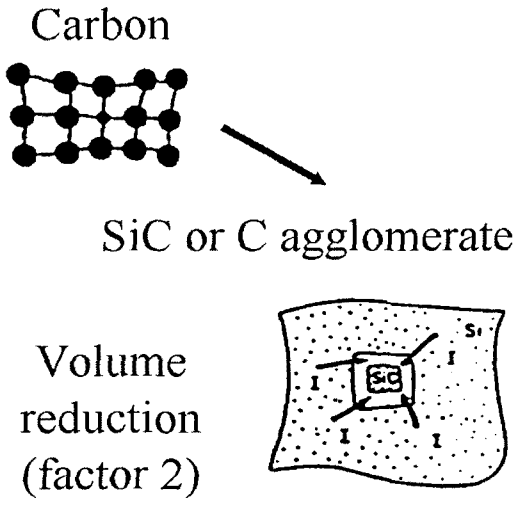

Figure 1.5 Schematic representation of simple volume consideration concerning the formation of SiC precipitates and C agglomerates.

In the as-implanted state, Si-C bonds form microregions of SiC. The full identification proves to be difficult because of the polymorphic nature of these crystallites, the high C content at the Si/SiC interfaces and the radiation damage. Depending on the implant conditions, at moderated annealing temperatures close to 800°C, a transition to β-SiC occurs as a result of the crystallisation of the Si matrix and the misfit strain.

The proximity of the free Si surface is an important factor influencing the process of formation of extended defects. C is able to capture implantation-induced Si interstitials, thus preventing their agglomeration in the form of extended defects. Dislocation elimination is most pronounced if the C distribution and the damage region created by the implant overlap.

Moreover, the C critical concentration necessary to amorphise the Si substrate is about 10^{21} cm^{-3}.

The radiation damage created during implantation can profoundly affect the manner of incorporation of impurities in Si. In general, impurities are more stable in sites where the number of nearest neighbours is equivalent to the natural valence. So, although C atoms are stable in substitutional (tetrahedral) sites in the Si lattice, they could predominantly occupy interstitial sites after the implantation even after annealing at high temperatures. However, interstitial C atoms can be substitutionally incorporated into the Si lattice using appropriate implantation and annealing conditions. In fact, disorder and a high concentration of implanted C reduce the topological constraint of the Si lattice imposed on C atoms, thus making their location in substitutional sites unlikely.

The high C content within the amorphised Si material raised the temperature needed for a proper Solid Phase Epitaxy Growth (SPEG) and reduces the SPE growth rate, thus inhibiting the regrowth of a single-crystal Si from a carbon-amorphised layer. At sufficiently high concentrations, C precipitate to form SiC, which in turn inhibits the SPEG process.

When annealing at high temperatures (up to 1000°C), little redistribution of the implanted C takes place due to the marked stability of the C in-depth profile. However, under certain implant conditions, great redistribution of C may occur during rapid thermal annealing at these high temperatures. On the other hand, the relaxation of the lattice strain in C implanted Si after annealing partly results from the rearrangement of displaced Si atoms and partly from the formation of SiC precipitates.

Finally, some comments about the effect caused by the incorporation of a C volume concentration high enough to form stoichiometric SiC layers. Both surface and buried layers of stoichiometric SiC can be produced by Ion Beam Synthesis (IBS) using high-dose C implantation and subsequent high-temperature annealing. The cubic form, β-SiC, is the equilibrium structure resulting from a topotactic transformation imposed by the Si lattice. The microstructure of the synthesised β-SiC layers depends critically on both the implantation temperature and the annealing temperature.

IBS of SiC layers can constitute an interesting alternative to the other techniques used for heteroepitaxial growing of SiC layers, such as CVD and MBE. In principle, ion beam synthesised layers are free from the voids that appear in the Si substrate region by CVD or MBE growing of SiC layers.

By choosing a suitable combination of implant and anneal parameters, the crystalline quality of the SiC grains can be optimised, avoiding the severe problem related to the high lattice mismatch between both Si and SiC lattices. Moreover, for thick SiC films, the ion beam synthesised layer can also be used as precursor for the heteroepitaxial growth of SiC on Si. Summarising, ion implantation based technology for fabrication of SiC layers can promisingly be used for the development of different kinds of sensors and devices, and the development of such technology constitutes the main goal of this work.

1.2.3 IMPLANT SIMULATOR: TRIM

The most important program that simulates implantation processes is called TRIM (Transport of Ions in Matter). It is based on the Monte Carlo statistical method, whose theoretical calculations come from the analysis of elastic angle scattering. In the last TRIM version, which is called SRIM, have been incorporated some programs that calculate the stopping and range of ions with energies between 10 eV and 2 GeV into matter using a full quantum mechanical treatment of ion-atom collisions.

This calculation is made very efficiently by the use of statistical algorithms that allow the ion to make jumps between the calculated collisions and then averaging the collision results over the intervening gap. During the collisions, ions and atoms have a screened Coulomb collision, including exchange and correlation interactions between the overlapping electron shells. The ion has long range interactions creating electron excitations and plasmons within the target. These are described by including a description of the target's collective electronic structure and interatomic bond structure when the calculation is set up. The charging state of the ion within the target is described using the concept of effective charge, which includes a velocity dependent charge state and long range screening due to the collective electron sea of the target. SRIM accepts complex targets made of compound materials with up to 8 layers from each one. It calculates both the final 3D distribution of the ions and also all the kinetic phenomena associated with the ion's energy loss: target damage, sputtering, ionisation, and phonon production. All target atom cascades can be followed in detail. A full description of the calculation is found in the tutorial books. TRIM results from the original work by Ziegler et al[39], while SRIM was done by Biersack[40]. Different graphics of the simulated data obtained with this program will be presented along the work, because before any attempt to make an actual implant experiment, some previous simulation was performed.

1.3 ANALYTICAL TECHNIQUES

In the following sections, the analytical techniques used in this work will be briefly described, focussing in both the principles and the particular technological configuration. Non destructive Raman and FTIR spectroscopies, together with XPS and TEM are part of the wide group of techniques applied to the characterisation of the different materials[41]. At the end, there is table that summarises the main characteristics of these techniques (in the equipments used in this work). The main methods to study and understand the results will also be comment. All the equipment and used facilities are part of the modern high technologic infrastructure placed on the Scientific-Technical Services, created by the University of Barcelona in order to support the scientific research[42].

1.3.1 VIBRATIONAL SPECTROSCOPIES: RAMAN AND FTIR

Raman and infrared spectroscopies are well suitable vibrational techniques for the characterisation of structures and processes in Si related technologies. Raman scattering gives information on the structural assessment of both amorphous and crystalline layers. Fourier Transform InfraRed (FTIR) technique complements this structural analysis on dielectric layers in Si technology (for instance nitrides and oxides), which have a very low Raman efficiency.

1.3.1.1 RAMAN SPECTROSCOPY

Raman spectroscopy[43] is primarily a structural characterisation tool. The spectrum is more sensitive to lengths, strengths, and arrangements of bonds in a material than to the exact chemical composition. The Raman spectrum of crystals likewise responds more to details of defects and disorder than to trace impurities and related chemical imperfections. The essentials of the Raman scattering experiment are shown in figure 1.6.

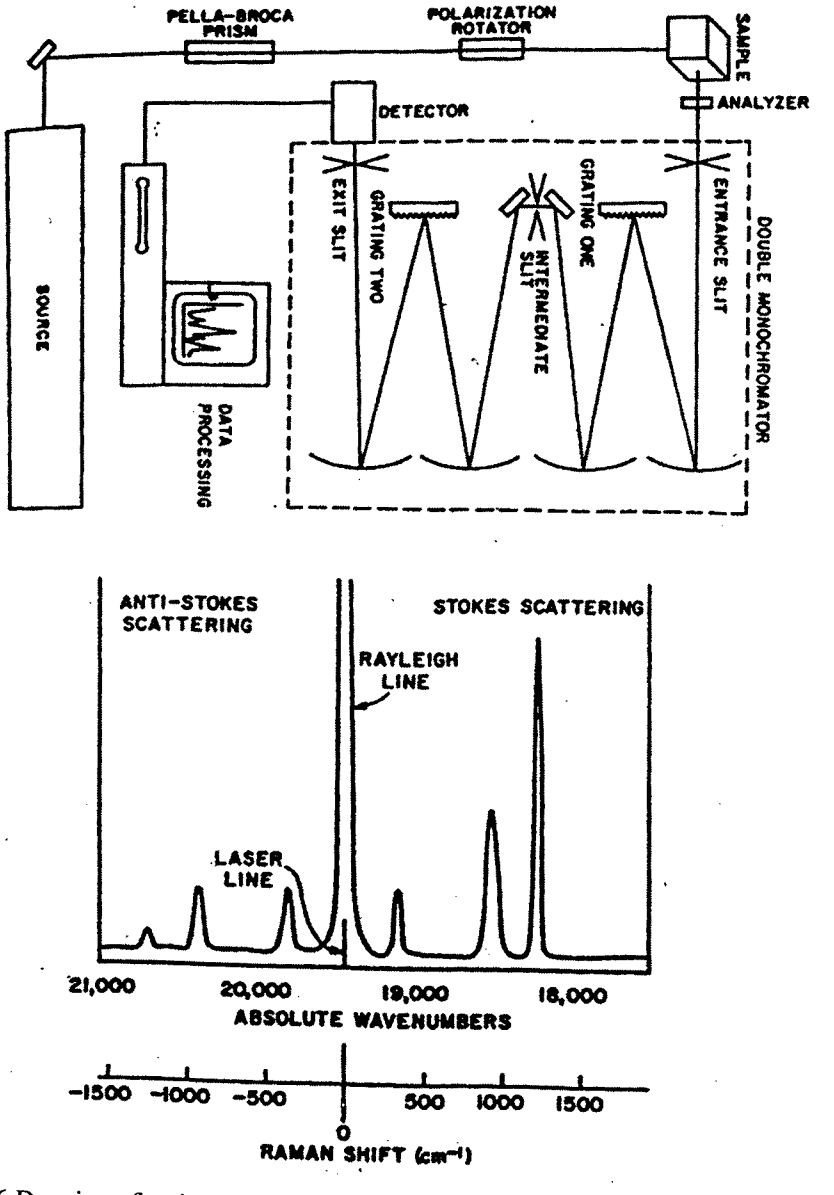

Figure 1.6 Drawing of a single-channel spectrometer with double monochromator (a) and schematic Raman scattering spectrum (b)

An intense monochromatic light beam impinges on the sample. The electric field of the incident radiation distorts the electron clouds that make up the chemical bonds, storing some energy. When the field reverses as the wave passes, the distorted electron clouds relax and the stored energy is irradiated. Although the incident ion beam may be polarised so that the electric field is oriented in a specific direction with respect to the sample, the scattered beam is radiated in all directions, making it possible to consider a variety of scattering geometries. Most of the stored energy is re-radiated at the same frequency as that of the incident exciting light. This component is known as the Rayleigh scattering and gives a strong central line in the scattering spectrum. However, a small portion of the stored energy is transferred to the sample itself, exciting the vibrational modes also called phonons. The vibrational energies are inferred from the energy of the incident beam and weak side bands appear in the spectrum at frequencies less than that of the incident beam. These are the Raman lines. Their separation from the Rayleigh line is a direct measure of the vibrational frequencies of the sample. The reverse process also occurs. Existing vibrations that have been excited by thermal processes can be annihilated by coupling with the incident beam and can add their energies to that of the source. These appear as side bands at higher wavenumbers.

The Raman process that excites molecular and crystal vibrations is called Stokes scattering, while the process that annihilates existing vibrations is called anti-Stokes scattering. The two spectra are mirror images on opposite sides of the Rayleigh line. However, because anti-Stokes scattering depends on the existence of thermally activated vibrations, the anti-Stokes intensities are strongly temperature dependent, whereas the Stokes intensities are only weakly temperature dependent and, for this reason, Stokes scattering is usually measured. On the other hand, the intensity ratio between Stokes and anti-Stokes lines provides a way to optically determine the temperature in the scattering volume.

Because the vibrational frequencies are measured by differences between the frequency of the Raman line and the Rayleigh line, most spectrometers are set up to directly display the frequency difference in wavenumber, defining the exciting frequency as 0. This sometimes causes confusion, because as the displayed Raman wavenumber increases, the true wavenumber decreases. Moreover, the Raman effect is extremely weak, for instance from optically transparent samples it is on the order of 10^{-3}-10^{-5} of the intensity of the Rayleigh line. For this reason, in modern Raman spectrometry intense monochromatic laser sources combined with double monochromator systems for stray light discrimination are needed.

In the present case, Raman scattering measurements were performed in a backscattering configuration, using a Jobin-Yvon T64000 spectrometer coupled with an Olympus metallographic microscope. Excitation was provided by an Ar^+ laser operating at different wavelengths, 457.9 nm, 488 nm and 514 nm, depending on the studied material and its behaviour. For these wavelengths, the depth penetration of scattered light in backscattering configuration is estimated to be of about 300 nm, 600 nm and 800 nm in single crystal Si, respectively. However, for highly defective material there is a significant reduction in these penetration depths, due to the increase in light absorption.

Both the excitation and the collection of the light were performed through the microscope objective. The optical microscope in the Raman spectrometer allows to achieve a high lateral resolution. According to the Rayleigh diffraction criteria, the diameter of the light spot on the sample is given by $1.22\lambda/NA$, being NA the numerical aperture of the microscope objective. Using a x100 objective with NA=0.95, the size spot in the sample can be as low as 0.6μm (λ=457.9 nm), which allows to achieve submicron lateral resolution.

A critical feature when using MicroRaman is related to the excitation power. The small excitation volume achieved with the x100 objective of the microscope (of μm^3) determines a very high power density in the excited surface that can be higher than several Mw/cm^2. This can cause the presence of thermal effects in the spectra. These effects are related to the increasing anarmonic contributions with the temperature in the scattering volume, and determine shifts and asymmetric broadening (related to the presence of temperature gradient) of the peaks. This is specifically important when measuring highly damaged layers, for which optical absorption increases. To avoid such effects, a previous calibration on the presence of thermal effects in the spectra has to be performed. The excitation power density on the sample has been kept below a threshold value, which has been determined for all the analysed samples. This has been done by comparing the spectra performed at different excitation powers. The results show the absence of thermal effects in all the analysed samples when the excitation power is kept below 0.75 Mw/cm^2.

Finally, in order to analyse the different modes related to more interesting Si, Ge and C bonds the spectra were measured in different zones inside a broad spectral region between 50 cm^{-1} and 1900 cm^{-1}. All the measured spectra have been compared with those obtained at the same conditions on not processed (virgin) samples. When possible the peaks in the spectra have been fitted to Lorentzian and Gaussian functions. This has allowed to determine the position of the crystalline peaks with an uncertainty normally better than 0.5 cm^{-1}, and the Full Width at Half Maximum (FWHM) of the different peaks.

1.3.1.2 FTIR SPECTROSCOPY

With respect to Fourier Transform Infrared Spectroscopy (FTIR)[44], the vibrational motions of the chemically bound constituents of matter have frequencies in the infrared regime. The oscillations induced by certain vibrational modes provide means for matter to couple with an impinging beam of infrared electromagnetic radiation and to exchange energy with it when the frequencies are in resonance.

In the infrared experiment, the intensity of the beam of infrared radiation is measured as a function of the light frequency (ω_i) before (I_0) and after (I) it interacts with the sample. Thus, the infrared spectrum is the plot of I/I_0 versus frequency. The identities, surrounding environments and concentrations of the chemical bonds that are present can be determined from these spectra.

The main uses of this non-destructive technique are the qualitative and quantitative determination of chemical species for solids and thin films, as well as, stress and structural inhomogenity measurements. In particular in Si technology, FTIR is one of the main techniques for the quantitative determination of impurities. Moreover, FTIR is also very useful for the chemical and structural analysis of the dielectric layers used in Si technology, such as oxide and nitride ones. In these materials, the main vibrational modes are affected by features such as stoichiometry, the presence of strain and structural disorder effects. Finally, FTIR is especially well suited for the analysis of C in Si, due to the good response of the absorption band related to the Si-C stretching bond. The shape and position of this band is determined by structural features, related to the amorphous or crystalline state of the SiC phase. The FTIR spectrum is also extremely sensitive to the presence of C atoms in substitutional positions in the Si lattice, having a characterised Local Vibrational Mode (LVM) at around 605 cm^{-1}.

FTIR transmission measurements were performed with a BOMEM DA3 spectrometer. The spectra were measured in vacuum at room temperature, using normal incidence and with a spectral resolution of 1 cm^{-1}. The absorption spectra from the differently treated samples were extracted by using as reference spectra those measured in the regions of the same samples which were not treated.

1.3.2 ELECTRON EMISSION TECHNIQUES: XPS AND AES

Electron emission techniques[45] are based on the measurement of the energy distribution of the electrons ejected from a material. As the electronic energy of each orbital is discrete and different for the same orbital in distinct atoms, the measurement of the electron binding energies can provide either atomic or chemical state identification, or even both. Moreover, since the energy of the concerning electron falls in the range where they can travel only very short distances without being inelastically scattered, these techniques are very surface sensitive. Profiling analysis can also been obtained by combining ion-beam sputtering with the continuous analysis of the electron ejected as the surface moves into the sample.

1.3.2.1 X-RAY PHOTOELECTRON SPECTROSCOPY (XPS)

X-ray Photoelectron Spectroscopy (XPS)[46], also known as Electron Spectroscopy for Chemical Analysis (ESCA), is widely used to investigate the chemical composition of the surfaces. The possibility to explore the first few atomic layers and assign chemical states to the detected atoms makes XPS a powerful analytical technique.

Surface analysis by XPS involves irradiating a solid in ultra high vacuum (UHV) with monoenergetic soft x-rays and analysing the energy of the emitted electrons. The spectrum is obtained as a plot of the number of detected electrons per energy interval, versus their kinetic energy. Each element has a unique spectrum. The spectrum from a mixture of elements is approximately the sum of the peaks of the individual constituents. Because the mean free path of electrons in solids is very small, the detected electrons originate only from only the few top atomic layers, making XPS a surface-sensitive technique for chemical analysis. Quantitative data can be obtained from peak heights or peak areas, and identification of chemical states can often be made from exact measurement of peak position and separations, as well as from certain spectral features. Apart from that, the use of an ion gun permits to investigate the distribution of the different phases formed in depth, being careful of some of the modifications of the material that may take place after the sputtering.

A photon of sufficiently short wavelength, and as a consequence high energy, can ionise an atom producing an ejected free electron. The kinetic energy KE of the electron, also called photoelectron, depends on the energy of the photon hν expressed by the Einstein photoelectric law,

$$KE = h\nu - BE$$

where BE is the binding energy of the particular electron to the corresponding atom. All the photoelectron spectroscopy is based on this equation. Since hν is known, a measurement of KE determines BE. From a practical point of view, a constant, ϕ_s, is added to the first part of the equation. This value, which in a sense limits the Fermi level, reflects the contribution of the experimental equipment and is called spectrometer work function.

As it is well known, electrons are arranged in orbitals around the nucleus, being bounded to it by the electrostatic attraction. Only two electrons of opposite spin occupy each orbital. The energy levels, or eigenvalues ε, of each orbital are discrete and different for the same orbital in distinct atoms because the electrostatic attraction is different for each nucleus.

In a first approximation, the BE of an electron, which is determined by the amount of energy required to remove it from the atom, is equal to the value of ε. This would be exactly true if, when removing an electron, all the other electrons did not respond in any way. By determining experimentally BE, the value of ε corresponding to the atom can be estimated so the atom can be identified. In figure 1.7, the XPS emission process for a standard atom is described.

It should be noticed that the peak intensities for different transitions are no identical because the probability for photoejection from each orbital, also called the photoionization cross section σ, is different. This probability also varies for a given orbital in different atoms and depends on the x-ray energy used. Thus, the number of peaks in the spectrum corresponds to the number of occupied energy levels in the atoms whose BEs are lower than the x-ray energy and the peak intensities depend on the number of atoms present and the σ values. So, for a correct quantitative analysis, an accurate study of the peak is needed, together with the perfect knowledge of σ and some secondary effects that affect the XPS spectrum, which are due to some physical and instrumental features. Actually, while the photoelectron is leaving the atom the other electrons respond to the hole being created. The responses, known as final state effects, often lead to additional features in the XPS spectrum.

Among these more complex effects it may be mentioned the spin-orbit splitting, the auger lines, the x-ray satellites, the x-ray ghost lines, the shake-up lines, the energy loss lines and the multiplet splitting. Some of these features are sometimes useful analytically.

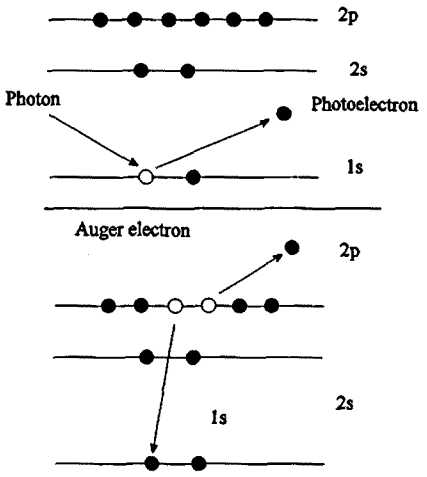

Figure 1.7 XPS and AUGER emission process for a model atom.

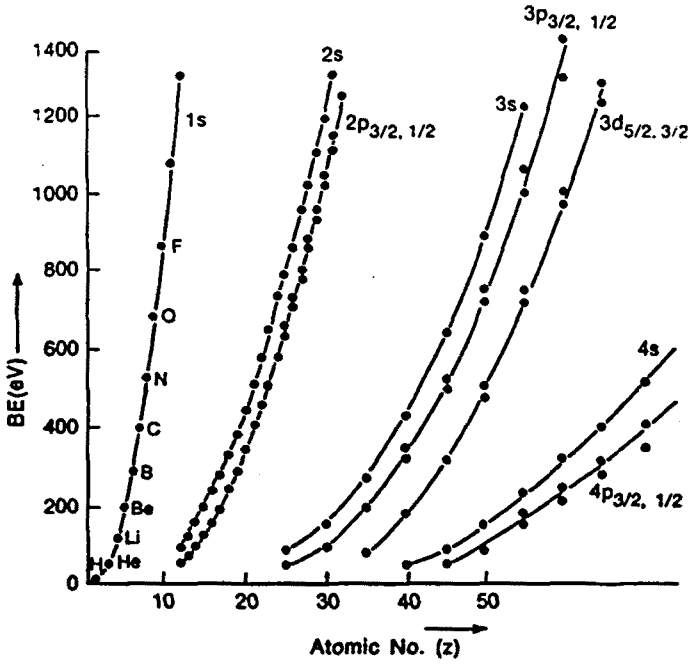

Figure 1.8 Approximate BEs of the different electron shells as a function of Z.

In principle, the electron energy levels of an atom can be divided into two types, core and valence levels. The chemical interaction between atoms to form molecules and compounds takes place via the valence levels, while core levels are nearly independent of the chemical state. Then, all the elements in the periodic table can be identified through their core electrons, except for H and He, and the binding energy for the different orbitals and atomic numbers can be plotted (figure 1.8). Although the chemical environment mainly affects the valence level, the energy of the core levels also changes little but noticeable. These chemical shifts allow the determination of the chemical state. With the simplest classical electrostatic representation of the atom, it is possible to conclude that the BE increases when the charge on the atom increases, in the majority of the cases.

The electrons leaving the sample are detected by an electron spectrometer according to their kinetic energy. The analyser is usually operated as an energy window, referred to as the pass energy, accepting only those electrons having energy within the range of this window. To maintain a constant energy resolution, the pass energy is fixed. Incoming electrons are adjusted to the pass energy before entering the energy analyser. Scanning for different energies are accomplished by applying a variable electrostatic field before the analyser. This retardation voltage may be varied from zero up to and beyond the photon energy. Electrons are detected as discrete events and the number of electrons for a given detection time and energy is stored. In figure 1.9, there is a schematic view of a typical electron spectrometer.

In this work, XPS measurements have been carried out with a Perkin-Elmer PHI 5500 Multitechnique system with AlKα (1486.6 eV) and MgKα (1253.6 eV) radiation. For the used conditions of measurement, FWHM of the Ag $3d_{5/2}$ line was of 1-1.5 eV, and the binding energy for adventitious C was 284.8 eV.

To investigate the distribution of the different phases formed in depth, XPS measurements were performed after sputtering samples to different thickness with an Ar^+ ion beam at 3 keV or 4 keV, depending on the material. In principle, some changes in the structure and composition of the surface region could be expected after Ar sputtering when investigating SiC compound layers, due to the preferential sputtering. However, Petzold et al[47] have observed that these effects depend on the sputter energy, reporting similar surface and bulk compositions in SiC for these ion beam energies. According to these data, no significant sputtering effects are to be expected in the XPS measurements.

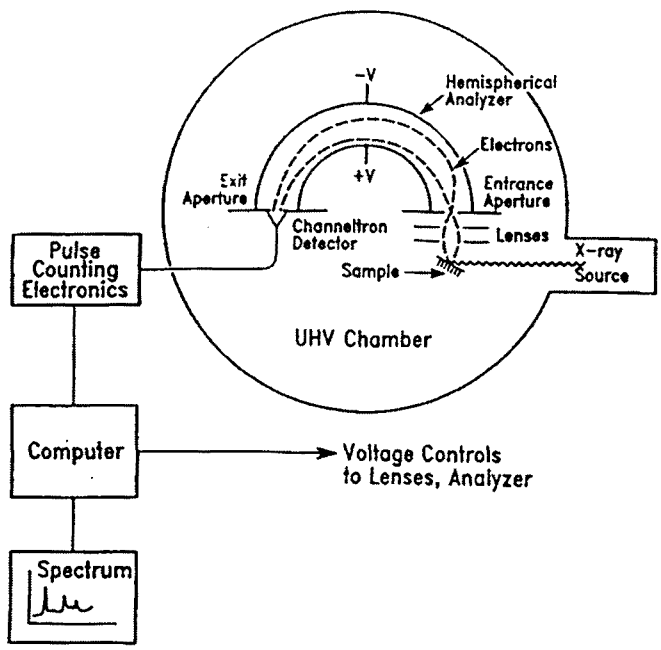

Figure 1.9 Scheme of a typical electron spectrometer with a hemispherical electrostatic electron energy analyser, showing all the necessary components

1.3.2.2 AUGER ELECTRON SPECTROSCOPY (AES)

Auger Electron Spectroscopy (AES)[48] is closely related to XPS. The hole left in a core level after the XPS process is filled by an electron dropping from a less tightly bound level, due to the electronic rearrangement of the excited atom. The energy released in this decay can be used to eject another electron, the Auger electron, whose energy only depends on the energy levels involved and not on what caused the initial core hole (all this was shown in figure 1.7). Unlike XPS, this fact allows to use an electron beam as a probe of the sample surface. However, since all the energy levels involved are core or valence levels, the type of information supplied, like in XPS, is elemental identification from peak positions and chemical state information (in some cases) from peak shifts and variation in line shapes.

The advantages of using AES in front of XPS are that there is an improvement in both lateral and depth resolutions, and an increment in the speed of collecting information, maintaining a good absolute detectability. The high spatial resolution of the electron beam allows AES to perform scanning images and microanalysis of three-dimensional regions of solid samples in UHV. The main drawbacks when using electrons as a primary source are the charging related problems, which can be unsolved when working with insulator materials. Moreover, whereas the extraction of qualitative information is quite simple, quantitative analysis to obtain the concentration of particular species is difficult to implement. Finally, as in the case of XPS, AES can be combined with an ion beam sputtering to remove material form the surface and perform in-depth studies.

AES measurements were carried out with a FISON system, with a LaB_6 filament electron source. For the used conditions of measurement, the FWHM of the Ag $3d_{5/2}$ line was of 1-1.5 eV, and the binding energy for adventitious C was 284.8 eV. Ar^+ sputtering was used to investigate in depth, being the previous XPS discussion also valid here.

1.3.3 ELECTRON MICROSCOPIES: TEM AND SEM

Electron microscopies have been extensively used to structurally characterise solid materials, providing a very magnified image, with good lateral resolution. Several types of electron microscopes and analysing instruments can be distinguished, being TEM (with the analysis of the diffracted electrons) and SEM the two most commonly used.

1.3.3.1 TRANSMISSION ELECTRON MICROSCOPY (TEM)

In Transmission Electron Microscopy (TEM)[49], a highly focussed electron beam incides on a thin sample, less than 200 nm, under vacuum conditions. The beam is energetic enough to propagate through the specimen. The signal is obtained from both undeflected and deflected electrons that penetrate the sample thickness. A series of magnetic lenses at and below the sample position are responsible for delivering the signal to a detector, usually a fluorescent screen, a film plate, or a video camera. Accompanying this signal transmission is a magnification of the spatial information in the signal by as little as 50 times to as much as 10^6 times. This remarkable magnification range is possible thanks to the small wavelength of the incident electrons, which is the key to the unique capabilities associated with TEM analysis.

Figure 1.10 shows a scheme of the ray paths for both unscattered and scattered electrons beneath the sample, while a scheme of a TEM instrument showing the location of a thin sample and the principal lenses within a TEM column is illustrated in figure 1.11.

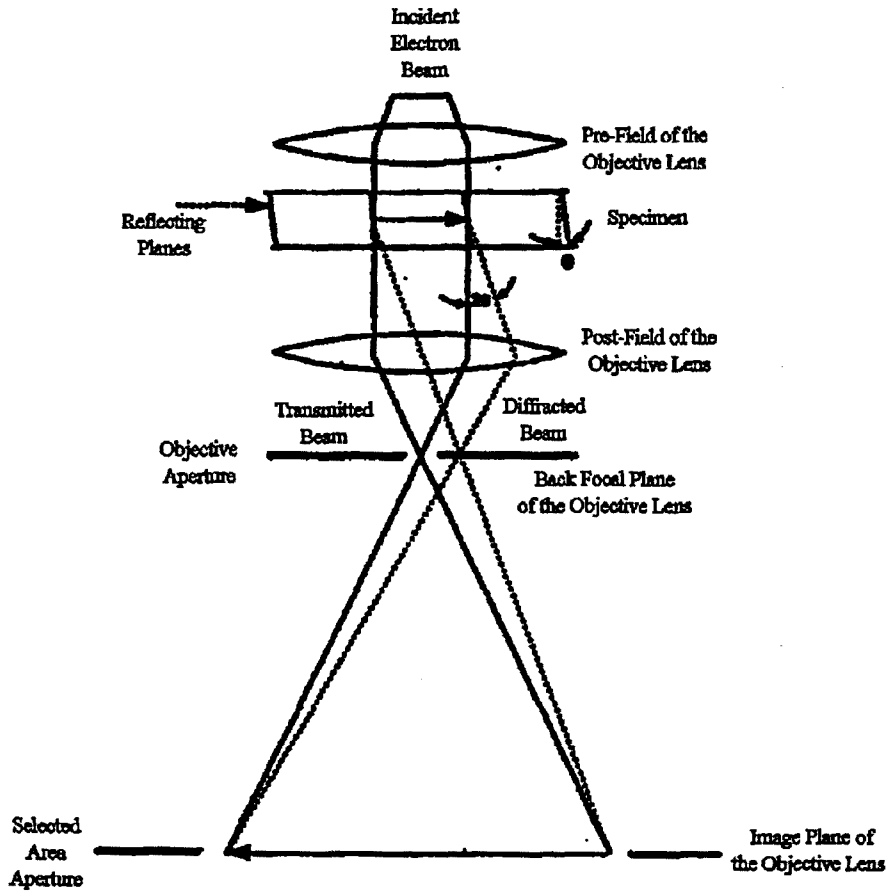

Figure 1.10 Representation for the ray paths of the electrons beneath the sample.

Transmitted electrons form images from small regions of the sample that contain enough contrast, due to the several scattering mechanisms associated with the interaction between electrons and the atomic constituents of the sample. Analysis of transmitted electron images yields information about the defects present in the material.

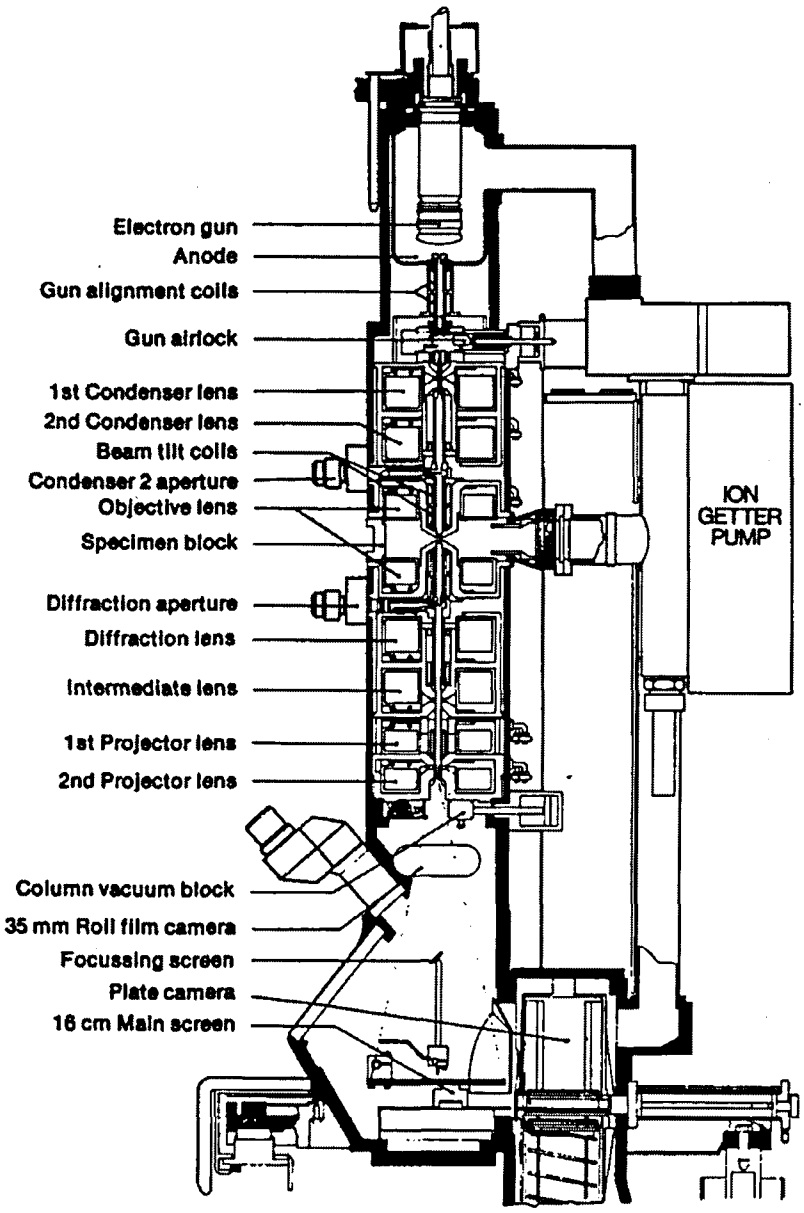

Figure 1.11 Schematic diagram of a TEM instrument.

On the other hand, diffracted electrons are also observed in the form of a diffraction pattern beneath the specimen. This is called Transmission Electron Diffraction (TED)[50] technique. Analysis of this pattern is used to determine the atomic structure. In an amorphous material, diffracted images show rings caused by the incoherent collisions of the electrons, while in a crystalline solid a coherent diffraction exists because of the exact disposition of the different atomic planes and only bright spots are seen. In a polycrystalline system with grains randomly oriented, rings are again observed, but their thickness is lower than in the amorphous case.

TEM measurements were performed by either a Hitachi H-800-NA microscope operated at 200 keV or a Philips CM30 SuperTwin microscope operated at 300 keV. Both microscopes can work with a lateral resolution better than 3 A. TEM involves a complex procedure for preparation of samples with dedicated equipment and systems such as GATAN dimplers, grinders and ion millings. Both planar-view and cross-section configurations have been used to prepare the samples. The type of the chosen preparation becomes definitive for delicate samples[51].

1.3.3.2 SECONDARY ELECTRON MICROSCOPY (SEM)

Scanning Electron Microscope (SEM)[52] is an electron microscopic technique that, in contrast with TEM, does not need sample preparation. Only in special cases, when analysing isolating samples, a thin metal coating is required to prevent charge accumulation. However, it has a lower magnification than TEM. In SEM, an electron beam is focussed into a fine probe and subsequently scanned over a small rectangular area. As the beam interacts with the sample it creates several signals, such as secondary electrons, internal currents and photon emission, all of which can appropriately be detected. These signals are highly localised in the area directly under the beam. By using these signals to modulate the brightness of a cathode ray tube, which is scanned in synchronism with the electron beam, an image is formed with a much greater depth of field than that formed in optical microscopy. With ancillary detectors, the instrument is even capable of doing some elemental analysis.

The main uses of SEM are high magnification imaging and elemental composition mapping. This technique is not destructive, but some electron beam damage is done. The beam energy range is 20-30 keV, although some instruments can work from 0.5 to 50 keV.

The sample requirements in SEM are vacuum compatibility and coating isolate samples with a conducting film. The analysed volume goes from a few nanometers to a few micrometers in depth, depending upon the accelerating voltage and the mode of analysis, and 1-50 nanometers of spatial resolution. Different SEM instruments have been used along this work, mainly a Jeol JSM 840 and a Hitachi S-2300. Magnification ranges go from x10 up to x200000 with an accelerating voltage range between 1 kV and 30 kV and a typical spatial resolution of 6 nm.

1.3.4 ADDITIONAL COMPLEMENTARY TECHNIQUES

In addition to the already described analytical techniques, the detailed study performed on the different structures and processes involved in this work has required the use of other structural and chemical techniques which are briefly described in this section. These techniques, X-Ray Diffraction (XRD), Secondary Ion Mass Spectroscopy (SIMS), Rutherford Backscattering Spectroscopy (RBS) and Atomic Force Microscopy (AFM) have provided the complementary information necessary to complete some parts of the presented work.

1.3.4.1 X-RAY DIFFRACTION (XRD)

X-Ray Diffraction (XRD)[53] constitutes a powerful technique for the structural analysis of crystalline materials. In XRD, a collimated beam of x-rays, with wavelength λ between 0.5 and 2 A, incides on a specimen and is diffracted by the crystalline phases in the specimen according to Bragg's law, $\lambda=2\cdot d\cdot\cos(\theta)$, where 'd' is the spacing between atomic planes in the crystalline phases. The intensity of the diffracted X rays is measured as a function of the diffraction angle 2θ and the specimen's orientation. This diffraction pattern is used to identify the specimen's crystalline phases and to measure its structural properties, including strain which is measured with great accuracy, epitaxy and the size and orientation of crystallites even in small crystallite regions. XRD can also determine concentration profiles, film thickness, atomic arrangements in amorphous materials and multilayers, and characterise defects. It is a non-destructive technique and all elements can be detected. Figure 1.12 shows the basic features of a typical XRD experiment.

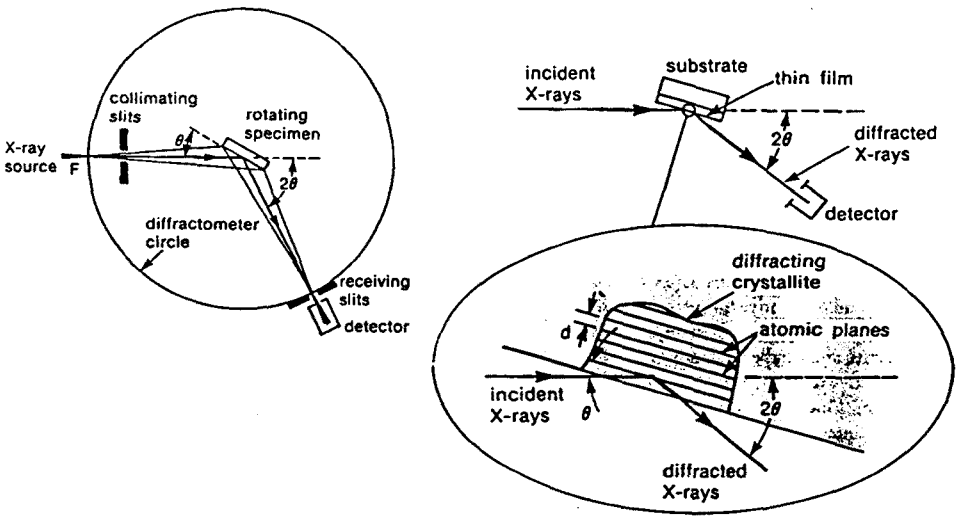

Figure 1.12 Basis of XRD technique in a Bragg diffractometer.

XRD basic spectra have been obtained with a Philips MRD diffractometer with CuKa radiation, while high-resolution spectra have been measured using a Barrel's Ge (200) 4-crystal monochromator. Conventional and texture XRD analyses have been carried out on the samples using the same instrument.

1.3.4.2 CHEMICAL-PHYSICAL TECHNIQUES: SIMS AND RBS

The chemical-physical characterisation of the samples has also been complemented with SIMS and RBS techniques in some cases. In Secondary Ion Mass Spectrometry (SIMS)[54], a solid specimen placed in vacuum is bombarded with a narrow beam of ions sufficiently energetic to cause rejection (sputtering) of atoms and small clusters of atoms from the bombarded regions. Some of the atoms and atomic clusters are ejected as ions. These ions are subsequently accelerated into a mass spectrometer, where they are separated according to their mass-to-charge ratio and counted. The relative quantities of the measured secondary ions are converted to concentrations, by comparison with standards, to reveal the composition and trace impurity content of the specimen as a function of the sputtering time (or depth).

SIMS technique is destructive, but detection limits arrive up to parts per billion, reaching a good depth resolution of about 10 nm. Measurements were performed with an Atomika ADIDA 3000-30 spectrometer, using both O^+ and Ar^+ as primary ion sources.

Rutherford Backscattering Spectrometry (RBS)[55] analysis is performed by bombarding a sample target with a monoenergetic beam of high-energy ions, typically He^+, with an energy of a few MeV. A fraction of the incident ions scatter backwards from heavier atoms in the near-surface region of the target material, and are detected and their energy is measured. The energy of a backscattered ion is related to the depth and mass of the target atom, while the number of ions detected is proportional to the target atomic concentration. This relationship is used to generate a quantitative depth profile of the upper 1-2 μm of the sample. Two types of studies can be done, sample randomly oriented or sample oriented with the alignment of the ion beam with respect to the crystallographic axes of the sample (channelling RBS). This permits crystal damage and lattice locations of impurities to be quantitatively measured. The main RBS applications are the quantitative depth profiling (accuracy of 15%) with a 1% or 1 part per million of detection limits for low and high Z elements, respectively. RBS is considered to be a non-destructive technique but some radiation damage appears after the He exposition. Random and channelling measurements using 1.7 MeV He^+ ions have been performed using the facilities available at the FZR[34].

1.3.4.3 ATOMIC FORCE MICROSCOPY (AFM)

Surface roughness measurements have been measured with Atomic Force Microscopy (AFM)[56]. In the AFM, a sharp tip located within a few A of the surface of the specimen scans the surface of a solid sample. The interaction forces between atoms on the surface and those on the tip cause the deflection of a microfabricated cantilever. Because the magnitude of the deflection strongly depends upon the separation between the surface and tip atoms, it can be used to map out surface topography with atomic resolution in all three dimensions. To summarise the AFM characteristics, it can be said that it is a non-destructive technique with vertical resolution of 0.1 A, lateral resolution from atomic up to 1 nm and accuracy better than 10% in distance. The field of view can be up to 250 μm. As a result, it is an unsurpassed technique like high-resolution three-dimensional profilometry. A Nanoscope III Extended Multimode AFM from Digital Instruments was used. The probe was a Tapping Mode AFM micromachined [100] Si tip supplied by Nanoprobes, Germany, operating in contact mode. The estimated force constant given by the manufacturer lies in a wide range, between 25 and 72 N/m.

TECHN.	MAIN INFORMATION	DEPTH	LATERAL RES.	TRACE CAP.	DESTRUC.
Raman	Structural phase	0.1-10μm	0.5-1μm	Variable	No
FTIR	Structural phase Impurities	100μm	≈cm	10^{13} cm^{-3}	No
XPS	Composition Chemical state	1μm (Res. 5nm)	75μm-1mm	0.01-0.3%	Yes (sputtering)
AES	Composition	5μm (Res. 5nm)	100A-1mm	0.01-0.3%	Yes (sputtering.)
TEM	Morphology Structural phase	<2μm	2A	0.1%	Yes
SEM	Surface morphology	1μm	1nm	0.1%	No
XRD	Structural phase	10-100μm	mm–10μm	3%	No
SIMS	Composition Impurities	100μm	50nm-2μm	Ppb-ppm	Yes (sputtering)
RBS	Composition Structural phase	20μm (Res. 2nm)	1nm-10μm	Ppb-%	No
AFM	Surface morphology	<A	<A-1mm	No	No

Table I-VII Summary of techniques and their main characteristics (in used equipments).

1.4 REFERENCES

1. H. Moissan
C. R. Acad. Sci. Paris *140* p. 405 (1905)

2. *Binary Alloys Phase Diagrams*, Ed. T. B. Masaki
The American Society for Metals, Ohio (1986)

3. *Silicon Carbide: A High Temperature Semiconductor*, Eds. J. R. O'Connors, J. Smiltens
Pergamon Press, New York (1960)

4. *Properties of Silicon Carbide*, Ed. G. L. Harris
Material Science Research Center of Excellence Howard University, Washington (1995)

5. H. Morkoç, S. Strite, G. B. Gao, M. E. Lin, B. Sverdlov, M. Burns
Journal of Applied Physics *76(3)* p.1363 (1994)

6. J. A. Lely
Ber. Dtsch. Keram. Ges. *32* p. 229 (1955)

7. P. G. Neudeck
Journal of Electronic Materials *24* p. 283 (1995)

8. R. F. Davis, G. Kelner, M. Shur, J. W. Palmour, J. A. Edmond
IEEE Proceedings *79* p. 677 (1991)

9. W. Wesh
Nuclear Instruments and Methods in Physics Research B *116* p.305 (1996)

10. J. Bullot, M. P. Schmidt
Physica Status Solidi B *143* p. 345 (1987)

11. W. Skorupa, R. A. Yankov
Materials Chemistry and Physics *44* p. 101(1996)

12. D. Alok, B. J. Baliga
Journal of Electronic Materials *24* p. 311 (1995)

13. V. Heera, J. Stoemenos, R. Kögler, W. Skorupa
Journal of Applied Physics *77* p. 2999 (1995)

14. *Application notes*, CREE Research Inc.
CREE publications, Durham NC (1999)

15. A. Amab, A.Spetz, Q. Wahab, M. Willander, I. Lundström
Sensors and Materials *4* p. 173 (1993)

16. A. Klumpp, U. Schaber, H. L. Offereins, K. Kühl, H. Sandmaier
Sensors and Actuators A *41-42* p. 310 (1994)

17. G. Muller, G. Krötz, E. Niemann
Sensors and Actuators A *43* p. 259 (1994)

18. P. A. Ivanov, V. E. Chelnokov
Semiconductors *23* p. 1003 (1995)

19. G. Krotz, W. Wondrak, M. Eickhoff, V. Lauer, E. Obermeier, G. Cavalloni
Advanced Microsystems for Automotive Applications Proceedings p.223 (1998)

20. S. C. Jain, H. J. Osten, B. Dietrich, H. Rücker
Semiconductor Science Technology *10* p. 1289 (1995)

21. H. J. Osten
Physica Status Solidi A *145* p. 235 (1994)

22. O. González-Varona
M. D. Thesis, University of Barcelona (1998)

23. *Ion Implantation of Semiconductors*, Eds. G. Carter, W. A. Grant
Edward Arnold, London (1976)

24. N. Bohr
Mat. -fys. Medd. Kgl. Dan.Vid. Selsk. *18* p. 8 (1948)

25. J. Lindhard, M. Scharff, H. E. Schiott
Mat. -fys. Medd. Kgl. Dan. Vid. Selsk. *33* p. 14 (1948)

26. *Ion Implantation Science and Technology*, Ed. J. F. Ziegler,
Academic Press, London (1984)

27. W. E. Bayle
The Electrochemical Society Proceedings *13* p. 345 (1992)

28. P. L. F. Hemment
Materials Research Society Symposium Proceedings *53* p. 207 (1986)

29. S. Mantl
Nuclear Instruments and Methods in Physics Research B *81* p. 895 (1993)

30. *Ion Solid Interactions for Material Modification and Processing*, Eds. D. B. Poker, D. Ila, Y. T. Cheng, Ll. R. Harriot
Material Research Society Publications, Pittsburgh (1996)

31. L. Calvo, A. Pérez-Rodríguez, A. Romano-Rodríguez, J. R. Morante, J. Montserrat
Materials Research Society Symposium Proceedings *311* p. 191 (1993)

32. L. Calvo, A. Pérez-Rodríguez, A. Romano-Rodríguez, J. R. Morante, J. Montserrat
Nuclear Instruments and Methods in Physics Research B *84* p. 214 (1994)

33. A. Pérez-Rodríguez, A. Romano-Rodríguez, J. R. Morante, M. C. Acero, J. Esteve, J. Montserrat, A. El Hassani
Journal of the Electrochemiacl Society *143* p.1026 (1996)

34. Institut für Ionenstrahlphysik und Materialforschung, Forschungszentrum Rossendorf Dresden, Germany

35. Asociacion de la Industria Navarra (AIN)
Navarra, Spain

36. Centro Nacional de Microelectrónica (CNM)
Barcelona, Spain

37. U. Gösele
Materials Research Society Symposium Proceedings *59* p. 419 (1986)

38. R. C. Newman
Materials Research Society Symposium Proceedings *59* p. 403 (1986)

39. *The Stopping and Range of Ions in Solids*, Eds. J. F. Ziegler, J. P. Biersack, U. Littmark
Pergamon Press, New York (1985)

40. J. P. Biersack
Nuclear Instruments and Methods in Physics Research *174* p. 257 (1980)

41. *Encyclopedia of Materials Characterisation*, Eds. C.R. Brundle, Ch.A. Evans, S.Wilson
Butterworth-Heinemann, Stoneham (1992)

42. Serveis Científico-Tècnics (SCT), Universidad de Barcelona
Barcelona, Spain

43. T. Jawhari, A. Pérez-Rodríguez,
Internet Journal of Vibrational Spectroscopy *2/4* p. 6 (1999)

44. *Practical Fourier Transform Infrared Spectroscopy*, Eds. J. R. Ferraro, K .Krishan
Academic Press, San Diego (1990)

45 *Practical Surface Analysis I: Auger and X-ray Photoelectron Spectroscopy*, Eds. D. Briggs, M. P. Seah
Wiley, New York (1990)

46. *Handbook of X-Ray Photoelectron Spectroscopy*, Physical Electronics (PHI)
PHI publications, Minnesota (1992)

47. J. Pezoldt, B. Stottko, G. Kupris, G. Ecke
Materials Science and Engineering B *29* p. 94 (1995)

48. *Handbook of Auger Electron Spectroscopy*, Physical Electronics (PHI)
PHI publications, Minnesota (1997)

49. *Transmission Electron Microscopy*, Ed. L. Reimer
Springer-Verlag, Heidelberg (1989)

50 *Transmission Electron Microscopy*, Eds. D. B. Williams, C. B. Carter
Plenum Press, New York-London (1996)

51. A. Romano, J. Vanhellemont, H. Bender, J. R. Morante
Ultramicroscopy *31* p. 183 (1989)

52. *Electron Microscopy in Solid State Physics*, Eds. H. Bethge, J. Heydenreich
Elsevier, Berlin (1987)

53. Element of X-Ray Diffraction, Ed. B. D. Cullity
Addison-Wesley Publishing Company, New York (1978)

54. *Practical Surface Analysis II: Ion and Neutral Spectroscopies*, Eds. D.Briggs,M.P.Seah Wiley, New York (1992)

55. *Backscattering Spectroscopy*, Eds. W. K. Chu, J. M. Mayer, N. A. Nicolet Academic Press, New York (1978)

56. G. Binning, C. F. Quate, G. Gerber
Physical Review Letters *54* p. 930 (1986)

CHAPTER 2

SYNTHESIS OF AMORPHOUS SiC AND RECRYSTALLISATION

In this chapter, the study of amorphous SiC obtained by ion implantation of C at different doses and its recrystallisation by thermal and IBIEC processes are reported. A special emphasis in the chemical order degree of the amorphous SiC is made. The analysis of systems synthesised by ion implantation into amorphous substrates requires a previous knowledge of the structure of the stoichiometric amorphous SiC. This has been acquired by the study of single crystal SiC samples that were amorphised by ion implantation. As it has been presented in the first chapter, Raman scattering is a useful technique for this kind of study.

2.1 ION BEAM INDUCED AMORPHISATION OF 6H-SiC

2.1.1 6H-SiC REFERENCE SAMPLE STUDIED BY RAMAN SCATTERING

Figures 2.1 and 2.2 show the Raman spectra measured in a (1000) 6H-SiC wafer. This wafer was obtained from Cree Research Inc[1], and corresponds to the state of the art available in 1997. These spectra have been obtained in backscattering configuration. The 457.9 Ar laser line was focussed on the sample with the x100 objective (NA 0.95) of the optical microscope (MicroRaman configuration). The weak optical absorption of SiC for the visible light determines the collection volume of scattered photons to be limited in depth by the axial focal tolerance of the microscope[2], $d=\lambda/NA^2$, which for the used measuring conditions corresponds to a depth of about 500 nm. Excitation power density on the sample was kept below 0.75 Mw/cm^2 in order to avoid thermal effects in the spectra.

As can be seen in figures 2.1 and 2.2, the Raman spectra measured in the 6H-SiC reference sample show the presence of eight first-order peaks. These peaks are divided into four groups according to the different LO, TO, LA and TA phonon branches in the standard large zone of SiC[3-5]. The symmetry and position of these peaks are indicated in table II-I. Although for the experimental conditions E_1 symmetry modes should not be observed, a weak peak corresponding to the x=0 TO branch appears in the spectra. This could be caused by disorder effects, related to the presence of structural defects already present in the non-implanted commercial wafer, as well as, by deviations from the ideal conditions of the experimental set-up, for instance of alignment.

Branch	x = 0.0	x = 0.33	x = 0.67	x = 1.0
LO	A_1 967 cm^{-1}	B_1	A_1	B_1
TO	E_1 797.5 cm^{-1}	E_2 789 cm^{-1}	E_1	E_2 767.2 cm^{-1}
LA		B_1	A_1 504 cm^{-1} A_1 514 cm^{-1}	B_1
TA		E_2 142 cm^{-1} E_2 147 cm^{-1}	E_1	E_2

Table II-I Symmetry and position in the large zone of the modes observed in 6H-SiC.

Figure 2.2 also shows the presence of several weak features in the 1000-1850 cm^{-1} region. These correspond to four broad band labelled 'a' to 'd', which can be fitted with gaussian curves, and a structure with eight peaks, labelled 'e' to 'l', at higher wavenumbers. As will be shown later, these features vanish when the scattering region is amorphised (the long-range crystal order is destroyed). They are probably related to second-order Raman processes, appearing in the same spectral region as the second-order Raman lines from 3C-SiC[6], but at different wavenumbers.

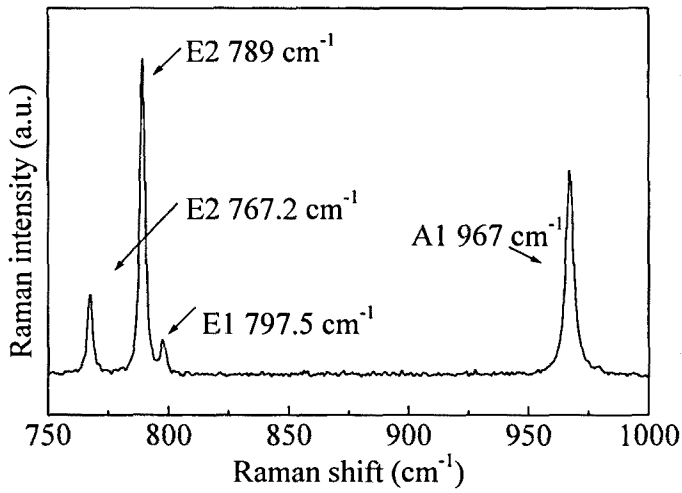

Figure 2.1 Raman spectrum from the reference 6H-SiC sample, showing the main first order Raman peaks.

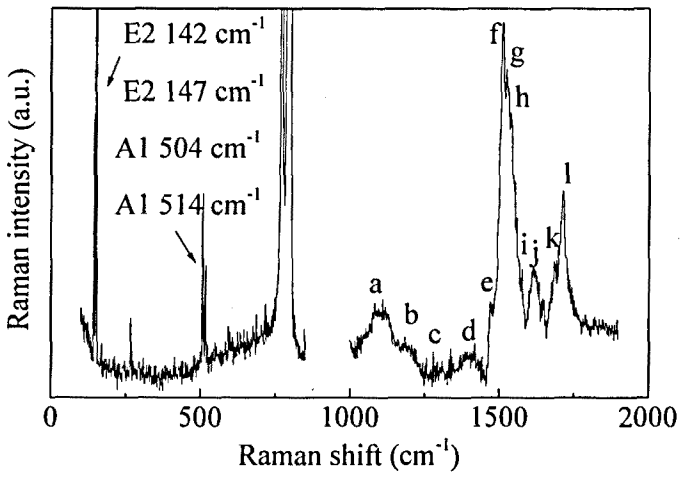

Figure 2.2 Raman spectra from the reference 6H-SiC sample in the spectral regions 50-800 cm^{-1} and 900-1850 cm^{-1}.

2.1.2 Ge-ION IMPLANTED 6H-SiC

Once the 6H-SiC reference sample has been characterised, the level of damage produced by the ion implantation has to be observed and analysed. The analysis has been performed as a function of the implantation dose and the annealing temperature. In this sense, 200 keV Ge^+ ions have been implanted at different doses from 10^{12} to 10^{15} cm^{-2} in a Si substrate. To amorphise the implanted layer Ge was selected because of its expected low value of threshold dose for amorphisation, which is related to its higher mass, and because the Ge ions do not introduce any electrical active defect in SiC.

2.1.2.1 AS-IMPLANTED SAMPLES: RAMAN SCATTERING ANALYSIS

In this first section, pieces from 6H-SiC (0001) wafers were implanted with different doses of Ge^+ ions between 10^{12} and 10^{15} cm^{-2}. Implantation energy was 200 keV, and all implantations were performed at RT. TRIM simulation for this implantation energy is shown in figure 2.3. Direct multiplication of the ion distribution by the implanted dose gives the theoretical concentration profile of the implanted specimen.

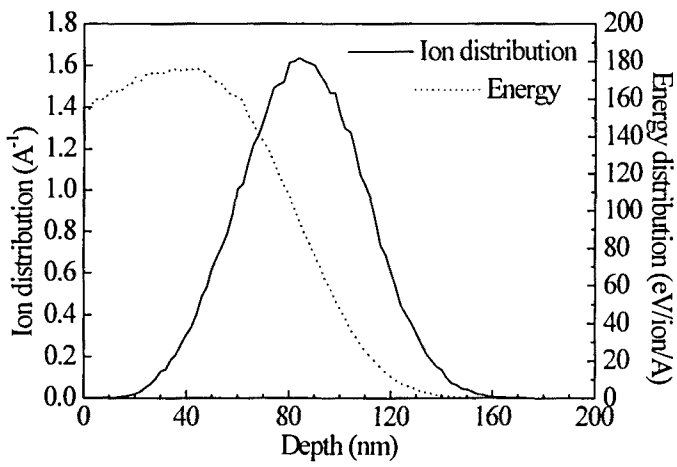

Figure 2.3 TRIM simulation of Ge^+ implanted in 6H-SiC at energy of 200 keV.

Raman spectra measured in samples implanted with doses between 10^{13} and 10^{15} cm^{-2} are plotted in figure 2.4. As it was expected, samples implanted at the lowest doses (not shown in this figure) exhibit Raman spectra similar to those from the reference. The only change observed in the spectra is a decrease in the intensity of the Raman peaks as the implanted dose increases. This decrease is related to the damage induced by the ion implantation, being probably determined by a decrease in the Raman polarisability tensors due to the breakdown of bonds and atomic displacements[7].

For crystalline damaged layers, the degree of damage induced by the implantation process can be quantified by the normalised intensity of the crystalline modes, I_n. This is defined as,

$$I_n = \frac{(I_0 - I)}{I_0}$$

where I_0 and I are the intensity of a certain crystalline mode measured in the reference and the implanted samples, respectively. For a very low damaged material, I is almost equal to I_0 and, as a result, I_n=0. In the other limit, if the scattering volume is fully amorphised, the crystalline modes vanish from the spectra and I_n=1. So, in general, I_n provides a quantification of the damage in the scattering volume between 0 (absence of damage) and 1 (fully amorphisation), which corresponds to the loss of long range order.

Figure 2.5 shows the behaviour of this parameter from the LO peak (967 cm^{-1}) versus the implanted dose. This behaviour is representative of that observed for all the crystalline modes in figures 2.1 and 2.2. The relative uncertainty in the measurement of a crystalline peak (lorentzian fitting) in the used equipment is of about 5%, which gives an uncertainty of I_n below 10%. This is mainly determined by deviations in the light spot focussing at the surface of the sample.

As shown in figure 2.5, for implantation doses below $3x10^{12}$ cm^{-2} the intensity of the peaks for the implanted samples is very similar to that from the reference, giving a value of I_n close to 0. This corresponds to the existence of a low damage level for implanted doses in this range. For higher doses, the intensity of the peaks decreases significantly, and this leads to an increase in I_n. For the highest implantation dose, I_n is close to 1. As already indicated, this corresponds to the amorphisation of the material in the scattering volume, with the disappearance of all the crystalline peaks. The minimum dose for which this occurs corresponds to the threshold dose for amorphisation. Interpolation of the data for doses between 10^{14} and 10^{15} cm^{-2} gives a threshold dose of about $2.5x10^{14}$ cm^{-2}.

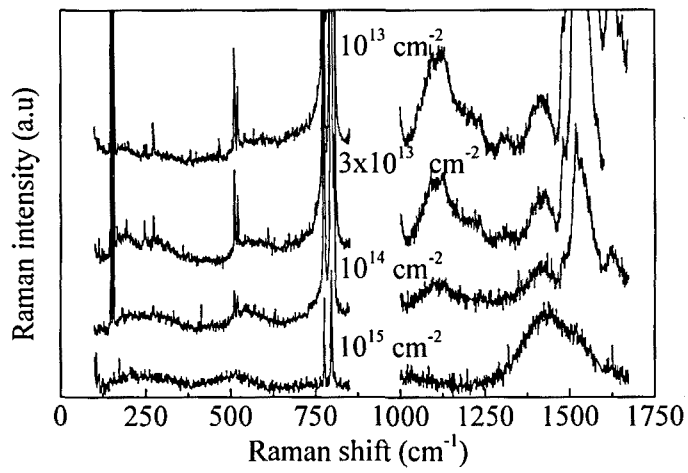

Figure 2.4 Raman spectra from the samples implanted at doses higher than 10^{13} cm^{-2}. The spectra are arbitrarily shifted, and the arbitrary units of Y scale from the spectra in the 900-1700 cm^{-1} region are 2.5 times higher those in the 50-900 cm^{-1} region.

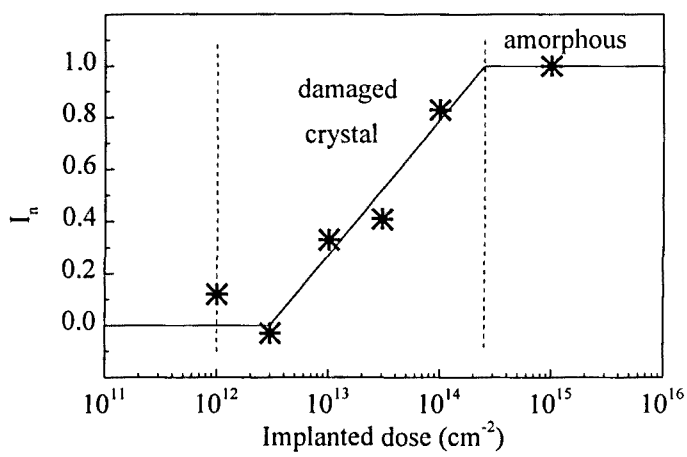

Figure 2.5 Relative intensity variation of the LO peak in relation to the reference sample versus the implantation dose, showing the damaged crystal and the amorphous regions.

Amorphisation of the implanted region is also accompanied by the appearance of three broad bands in the spectra. In figure 2.4, the spectrum measured in the sample implanted at the highest dose, higher than the threshold dose for the amorphisation, shows the presence of three bands centred at about 200, 500 and 1430 cm^{-1}.

These bands can be fitted with gaussian curves and have values of FWHM of 150, 90 and 160 cm^{-1}, respectively. This spectrum is similar to those previously reported for amorphous $Si_{1-x}C_x$ alloys obtained by different techniques[8,9] and has been interpreted according to a three-mode behaviour related to the different Si-Si, Si-C, and C-C vibrational modes[9,10]. The lowest two bands are similar to the TA and TO bands from amorphous Si (at about 160 and 480 cm^{-1}). The measurements reported for the amorphous $Si_{1-x}C_x$ alloys indicate that the wavenumber of the acoustic-like band increases with the C content, while the TO band is distorted. These bands are interpreted as Si-Si vibrational modes. Moreover, changes in the optical-like Si-Si band region are caused by the contribution of Si-C related modes in this region. However, in these measurements the Si-C modes at around 750 cm^{-1} are not observed. This could be due to the low Raman efficiency of these modes.

The band appearing in the 1300-1600 cm^{-1} spectral region is related to C-C vibrational modes. The position and shape of this band agrees with those previously measured on amorphous SiC layers deposited by other techniques, such as glow discharge and sputtering[9,10]. Chehaidar et al[9] have performed a theoretical simulation of this band assuming sp^2 and sp^3 coordinations of C, corresponding to amorphous-like diamond and amorphous-like graphite, respectively. According to this simulation, the position of this band should be 1260 cm^{-1} for sp^2 coordination and 1580 cm^{-1} for sp^3 coordination. From comparison between shape and position of the simulated and the experimental spectra, these authors have proposed the existence of a mixture of sp^2 and sp^3 coordination of the C. This existence has also been reported by Gorman et al[10], in agreement with the data reported from C films[11-14].

The spectra in figure 2.4 also show the presence of three peaks close to the Si-Si related amorphous bands for implantation doses below the threshold. In principle, this could be due to the existence of highly disordered domains in the implanted layer, even at doses below the threshold. The comparison of these bands with those obtained implanting other ions (such as B or Al) provides some evidence that their structural origin is not related to any chemical impurity and will be considered in following sections.

2.1.2.2 STRUCTURE OF ION BEAM DAMAGED AND AMORPHOUS SiC

In summary, the Raman spectra measured in the as-implanted samples provide evidence on the existence of three different levels of damage depending on the value of the implantation dose:

a) dose < $3x10^{12}$ cm^{-2}: low damage level
b) 10^{13} < dose < 10^{14} cm^{-2}: medium to high damage level
c) dose > 2-$3x10^{14}$ cm^{-2}: formation of a continuous amorphous layer.

The existence of these three different damage levels has also been observed from positron annihilation measurements[15]. Moreover, the value of the threshold dose for amorphisation in the range 2-$3x10^{14}$ cm^{-2} agrees with data from previous works[16,17]. Spitznagel et al[16] report a minimum deposited energy of about $2x10^{21}$ keV/cm^3 for amorphisation. According to the TRIM simulation for a 200 keV Ge^+ ion implantation into SiC, this corresponds to an implantation dose of $1.2x10^{14}$ cm^{-2}. However, the change of density under irradiation has not been taken into account in this simulation, and this could explain the lower threshold value predicted. Experimentally, a continuous buried amorphous layer has been observed by RBS and TEM techniques[17], for an implantation dose higher than $3x10^{14}$ cm^{-2}. So, the particular value of the threshold dose for amorphisation is between 10^{14} and $3x10^{14}$ cm^{-2}, in agreement with the presented estimation ($2.5x10^{14}$ cm^{-2}).

On the other hand, Raman scattering gives also strong evidence of the presence of Si-Si and C-C bonds in the amorphous network. This implies the existence of a partial loss of chemical order in addition to that of the long-range order for amorphous SiC. In this context, different authors have reported the structural analysis of amorphous SiC films, as a function of the preparation procedure and the C content. Chehaidar et al[9] have observed the existence of a chemical order in amorphous Si rich films deposited by glow discharge. In this case, all the C atoms are bonded to Si, forming with the Si-Si bonds a tetrahedrally connected network. However, for samples with stoichiometric composition, complete chemical order is not achieved, as Si-Si, Si-C and C-C bonds are detected. This is in agreement with the molecular dynamics simulations performed by Finocchi et al[18] for amorphous SiC at stoichiometric composition. These simulations confirm that the system can not be classified neither as chemically ordered, since 40-45% of bonds are homonuclear, nor as random, since a high degree of short to medium range order exists.

Other authors have reported the existence of highly ordered amorphous layers obtained by sputtering deposition, mainly with Si-C bonds, similar to what is found in the corresponding crystal[19]. These data agree with those from Sproul et al[20] and Laidani et al[21], who corroborated the preference of C to be bonded to Si, for layers deposited by plasma magnetron deposition or vacuum evaporation.

The existence of two different amorphous states in SiC with distinct chemical order configurations has been reported by Bolse et al[22]. These authors have studied 6H-SiC samples implanted at low temperatures with different Na^+ ion fluences, analysing the implanted samples by RBS, step height measurements and Raman scattering. From their analysis, they have reported the formation of an amorphous network at low fluences, which conserve the chemical short-range order of crystalline SiC. An increase in the fluency drives the system from this metastable state to an atomically disordered structure, with the formation of homonuclear bonds.

In the present work, the presence of the broad bands in the spectra from the samples implanted at dose above the threshold for amorphisation shows the formation of a relaxed amorphous structure with loss of chemical order. The absence in this case of a metastable chemically ordered amorphous state could be related to the higher degree of damage induced by the heavier Ge ions. According to Heera and Skorupa[23], the amorphisation in this case is determined by the accumulation of highly disordered amorphous zones directly produced by collision cascades. This is strongly supported by the presence of disorder-like bands in the spectra, already at doses below the threshold for amorphisation. Quantification of the amount of homonuclear and heteronuclear bonds in amorphous SiC has been performed by XPS measurements for ion beam synthesised amorphous films, and will be presented in the following sections.

It is also interesting to remark the very low intensity of the crystalline peaks from the samples implanted at the highest doses, in spite of the lower thickness of the ion implanted layer (which should be below 100 nm in accordance to TRIM), when compared to the estimated penetration depth of the scattered light (of about 500 nm). For the sample implanted at the dose of 10^{15} cm^{-2}, only the most intense peaks are observed, with a very low intensity, as can be seen in figure 2.4. This could be due to a strong enhancement of optical absorption in the amorphous layer. The thickness of the surface amorphous layer in this sample is about 143 nm as observed by TEM[24]. Assuming that this sample has a similar reflectivity as the non-implanted one and neglecting multiple reflections in the surface amorphous layer, the comparison between the intensity of the crystalline peaks in the spectra from the implanted and non-implanted samples gives a value for the absorption coefficient in this layer of the order of 1/(70 nm) for a wavelength of 457.9 nm[25].

An enhancement of optical absorption in amorphous SiC has been reported from measurements on β-SiC membranes after and before amorphisation by ion implantation[26]. This is interpreted as a direct consequence of the relaxation of the k-selection rule for the optical transitions, determined by the loss of long range order. However, the absorption values reported in the mentioned work are much lower than those estimated from the intensity of the Raman crystalline lines. This could be caused by an enhancement of absorption in the amorphous layer by multiple reflections in the present structures. Moreover, the presence of a damaged SiC region below the amorphous layer would also decrease the intensity of the crystalline peaks from the substrate. This is in agreement with positron annihilation and infrared measurements[24,27], which show the existence of a damaged region below the amorphous layer in the implanted samples.

2.1.2.3 ANNEALED SAMPLES: RECRYSTALLISATION AND DAMAGE RECOVERY

The study of the Ge^+ implanted wafers has also been extended to the annealed samples in order to investigate the recovery of the ion beam induced damage and recrystallisation of the implanted layers. Damage recovery and recrystallisation by thermal annealing are important features in SiC technology, where ion implantation constitutes the main process for achieving selective doping of the material.

In this sense, samples implanted at doses below (10^{14} cm^{-2}) and above (10^{15} cm^{-2}) the threshold for amorphisation were annealed at 500, 950 and 1500°C in an Ar atmosphere during 10 minutes. Figures 2.6 and 2.7 show the Raman spectra measured in the annealed samples. For both doses, there is a strong increase in the intensity of the crystalline peaks and a decrease in the amorphous disorder-like bands as the annealing temperature increases. The complete disappearance of the amorphous bands is observed after annealing at 1500°C.

The increase of the intensity of the crystalline peaks is related to the recovery of the crystalline lattice with the annealing. However, a complete recovery of the lattice is not achieved even at the highest annealing temperature. In figure 2.8, the variation of the relative intensity I_n of the LO peak is plotted versus the annealing temperature. As it is shown, for an annealing temperature of 950°C, the intensity of the crystalline lines in the spectra from both samples is very similar, with a relative intensity of the LO peak of approximately 0.2. Increasing the annealing temperature up to 1500°C does not cause a further decrease of I_n.

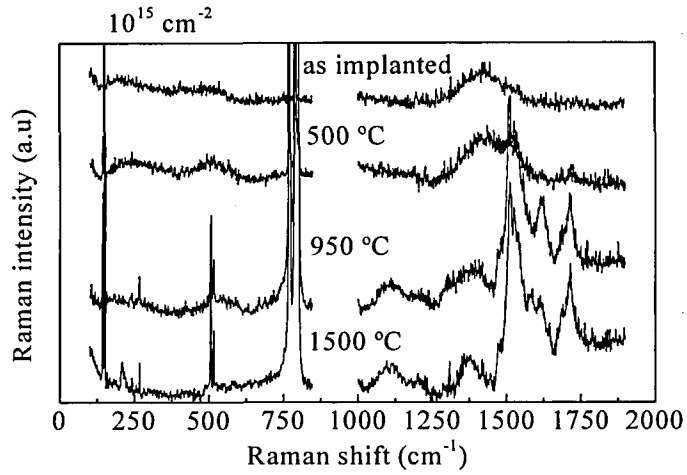

Figure 2.6 Raman spectra from the samples implanted at the dose of 10^{14} cm^{-2} and annealed at different temperatures.

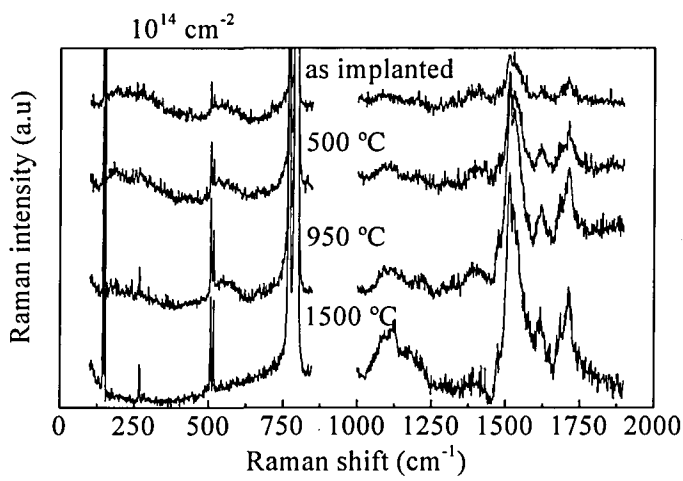

Figure 2.7 Raman spectra from the samples implanted at the dose of 10^{15} cm^{-2} and annealed at different temperatures.

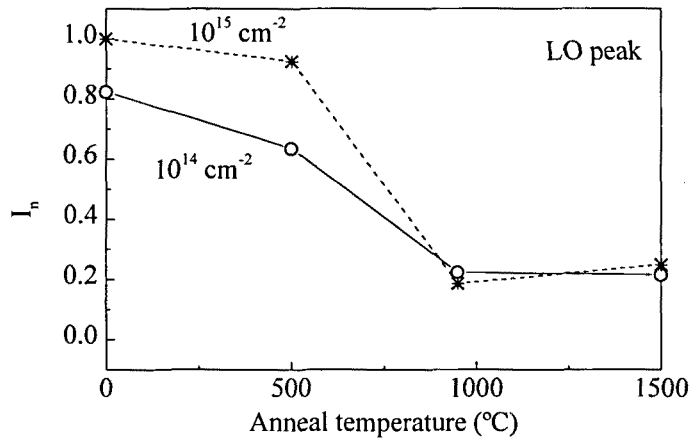

Figure 2.8 Relative intensity variation of the LO peak in relation to the reference sample versus the annealing temperature for the samples implanted at 10^{14} and 10^{15} cm^{-2}.

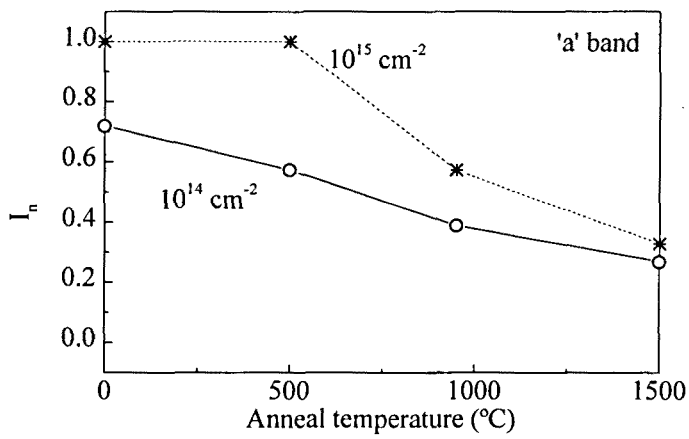

Figure 2.9 Relative intensity variation of the band labelled 'a' (in figure 2.2) in relation to the reference sample versus the annealing temperature for the samples implanted at 10^{14} and 10^{15} cm^{-2}.

This behaviour contrasts with that of the second-order peaks, as can be observed in figures 2.6 and 2.7. For the sample implanted with the dose of 10^{14} cm^{-2}, a gradual recovery of the structure in the 1000-1850 cm^{-1} spectral region takes place with the annealing. For the highest annealing temperature, the shape of the spectrum in this region is very similar to that of the reference sample, shown in figure 2.2. For the samples implanted with a dose of 10^{15} cm^{-2}, the spectra in this region (1000-1850 cm^{-1}) are very much distorted in relation to the reference, even after annealing at 1500°C, and show a lower relative intensity of the band labelled 'a' in reference figure, at about 1116 cm^{-1}.

In figure 2.9, I_n of the 'a' band is plotted versus the annealing temperature. As it is shown, the sample implanted at the lowest dose is characterised by lower values of I_n. This indicates a higher residual damage in the samples implanted at the highest dose. Moreover, in both cases the samples with lowest residual damage are those annealed at the highest temperatures.

The similar level of residual damage (as deduced from the normalised intensity of the first order LO mode) in samples implanted at doses of 10^{14} and 10^{15} cm^{-2} and annealed at 1500°C might be related to the existence in the samples implanted with the lowest dose of significant disorder effects, as shown in the corresponding Raman spectra. The lack of a complete recovery in the intensity of the Raman modes can be correlated with the presence in these samples of structural defects such as stacking faults and vacancy-type defects, which have been observed from Positron Annihilation and XTEM observations[23]. The difficulty for a complete recrystallisation of amorphous SiC can be due to the loss of chemical order in the amorphous phase. Recrystallisation implies the break of all the homopolar Si-Si and C-C bonds. In this sense, it is necessary to bear in mind the high energy of C-C bonds, which is of about 3.7 eV for sp^2 co-ordination, which indicates a very high stability of these bonds, higher than that of Si-C or Si-Si ones. This agrees with the high stability of the region amorphised by ion implantation, which requires an annealing at the highest temperature (1500°C) in order to observe the complete disappearance of the amorphous bands in the spectra.

The lack of a correct epitaxial recristallisation in these samples has been corroborated by TEM observations, which show the appearance of zones of highly defective columnar 6H-SiC and misoriented crystalline grains of 3C-polytype[28]. According to Heera and Skorupa[23], the distorted epitaxial crystallisation regrowth starts at about 900°C, and it is accompanied by polycrystallisation and twin formation. This behaviour indicates that, in contrast with the Si technology, in SiC it is not possible to achieve a solid phase epitaxial regrowth of the amorphised film. This is critical for SiC technology as it determines the need to avoid amorphisation in the implanted layers.

2.1.3 Al-ION IMPLANTED 6H-SiC

The possibility in Raman scattering to quantify the level of residual damage in a non-destructive and simple way has also been applied to the study of ion beam induced damage in 6H-SiC implanted with Al^+ ions. In principle, this allows to complete the study performed on the Ge^+ implanted samples, in order to clarify the possible dependence of the chemical impurity on damage and disorder-induced bands, in the implanted region.

On the other hand, the low mobility of impurities in SiC forces to use ion implantation for a selective doping of the active areas in the devices. The high stability of ion beam induced damage and the absence of a complete epitaxial recrystallisation of the amorphised films has motivated a strong interest in implanting at high temperatures. In principle, there are two main candidates for p-type doping in SiC, B and Al. Although the lower mass of B in relation to Al would imply a lower level of damage in the implanted layer, Al is much more interesting for p-doping due to its lower ionisation energy.

Taking this into account, the study has been focussed on the analysis of Al^+ ions implanted in 6H-SiC samples as a function of the implantation temperature, between RT and 1200°C. The implanted substrates have been n-type 6H-SiC layers (thickness of 5 μm, $n=7x10^{15}$ cm^{-3}) epitaxially grown on 6H-SiC (0001) wafers from Cree Research[1]. In order to obtain a flat Al concentration in the implanted region, a 4-fold implantation has been used, with the following energies and doses parameters,

(i) E=500 keV, $\phi=1.1x10^{15}$ cm^{-2},
(ii) E=360 keV, $\phi=6.5x10^{14}$ cm^{-2},
(iii) E=260 keV, $\phi=4.8x10^{14}$ cm^{-2},
(iv) E=180 keV, $\phi=4.4x10^{14}$ cm^{-2}.

By this way, a 400 nm thick layer buried at a depth of 200 nm with a constant Al concentration of about $5x10^{19}$ cm^{-3} is achieved, as can be seen in figure 2.10, where the profiles simulated by TRIM are plotted.

According to the data obtained from the samples implanted with Ge^+ and annealed, pieces from the implanted wafers have been annealed in vacuum at 1500°C for 10 minutes. Instead of an Ar atmosphere, vacuum has been chosen in order to avoid any possible etching of the SiC surface by oxidation from the O residual in the annealing chamber at these high temperatures[23].

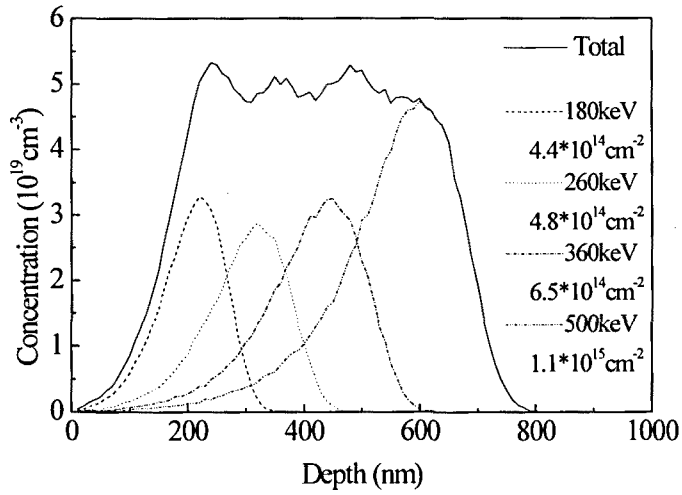

Figure 2.10 TRIM simulation of Al^+ implanted in 6H-SiC.

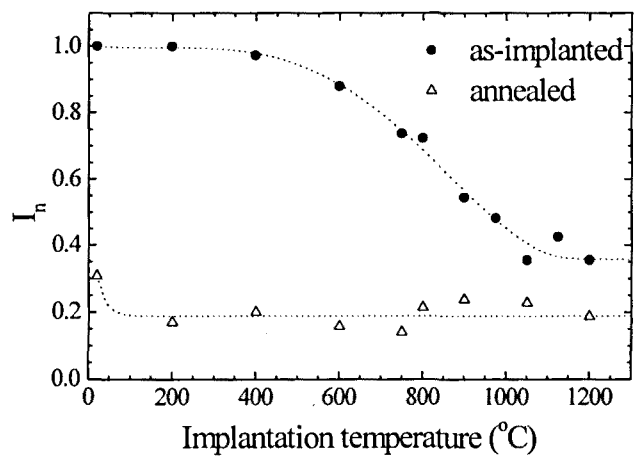

Figure 2.11 Normalised relative intensity of the TO Raman line versus implanted temperature for the as-implanted (circle) and the annealing (triangle) samples.

2.1.3.1 AS-IMPLANTED SAMPLES: ROLE OF IMPLANT TEMPERATURE

Figure 2.11 shows the relative intensity I_n of the TO peak (789 cm^{-1}) versus the implantation temperature (T_{imp}) for the different as-implanted and annealed samples. The Raman spectra have been obtained with experimental conditions similar to those used in the Ge^+ implanted samples, but for the used objective in the Raman microprobe (x50, NA=0.55). According to this, the axial focal tolerance is of about 1600 nm, which in principle allows to investigate the whole depth of the implanted layer. However, it is necessary to bear in mind the strong increase observed in the optical absorption in highly damaged or amorphous SiC, and in these cases, the penetration depth of scattered light can be much lower.

For the as-implanted samples, implanting at temperatures lower than 200°C leads to the amorphisation of the implanted layer. This is observed from the disappearance of the crystalline modes (and hence I_n=1), and from the presence of broad amorphous Si-Si and C-C related bands in the Raman spectra. For temperatures of 200°C or higher, amorphisation is avoided and, in the temperature range between 200°C to 1000°C, a monotonous decrease in I_n is observed, which is related to the decrease in the residual damage of the as-implanted layer. For temperatures higher than 1000°C, I_n saturates down to a minimum value of about 40%. This behaviour agrees with the quantified damage from the RBS measurements[29].

The decrease in damage obtained as the implantation temperature increases in the temperature range between 100 and 1000°C is probably caused by an enhanced dynamic recombination of the point defects generated during the implantation process. On the other hand, the saturation of I_n for T>1000°C can be related to the formation of extended defects at these temperatures. The formation of such defects has been corroborated by cross-section TEM observations[30], which show the presence of extended defects as dislocation loops. This would be related to agglomeration of point defects forming defect clusters.

A similar behaviour has been reported by Itoh et al[31]. They have observed the formation of vacancy clusters in cubic SiC layers after implantation of N^+ and Al^+ ions at temperatures higher than 800°C. The formation of these clusters is independent of the implanted species, and their size increases with implantation temperature. This is interpreted in terms of migration of point defects like vacancies and interstitials. Defects related to C vacancies in 6H-SiC have been found to anneal at temperatures up to 500°C, probably by recombination with mobile interstitials[32]. On the other hand, different kinds of defects related to Si vacancies anneal at temperatures of around 750°C and 1500°C[33]. This has been interpreted as caused by the migration of the vacancies towards sinks as the N atoms form defect complexes that anneal out at a highest temperature.

Migration point defects as intertitials and vacancies can also explain the formation of extended defects in 6H-SiC layers implanted with Sb^+ ions at RT and 850°C and annealed at 1500°C[34]. In this case, for both implantation temperatures, the damage from the as-implanted samples consists of point defects that after the annealing agglomerate forming platelets and small dislocation loops. For the samples analysed in this work, the change in the nature of the induced defects suggests that the interstitials become mobile mainly for implantation temperatures higher than 1000°C.

Figure 2.12 shows the Raman spectra measured in the broad spectral region from 50 to 1900 cm^{-1}, from different as-implanted samples at RT, 400 and 800°C, together with the spectrum corresponding to the reference one. As already indicated, the spectrum from the sample implanted at RT does not show any crystalline mode, and only broad gaussian modes, related to Si-Si and C-C vibrational modes in amorphous SiC, appear.

Moreover, the spectra from the sample implanted at the highest temperature show the presence of three additional bands in the 50-600 cm^{-1} region. These bands have been labelled A, B and C. They are centred at about 185, 270 and 540 cm^{-1} and have values of FWHM of the order of 70-100 cm^{-1}. For implantation temperatures higher than 1000°C, a significant decrease in the intensity of the bands is observed. This occurs mainly for the B and C bands, being A still detectable at these temperatures.

These bands are similar to those observed in the spectra from the samples implanted with Ge^+ at doses below the threshold for amorphisation[35] (seen in figure 2.4), which points out their intrinsic nature. The decrease in their contribution for implantation temperatures higher than 1000°C, when interstitials become mobile, suggests that these bands are related to interstitial-like defects. In principle, the vibrational frequency of an interstitial C-like defect is expected to be higher than that of an interstitial Si-like defect, due to the lower mass of C. Moreover, C interstitial is expected to become mobile at a lower temperatures than Si interstitial. Taking all this into account, these bands could be attributed to Si and C interstitial related defects, respectively, although further experiments are required to confirm this point[36].

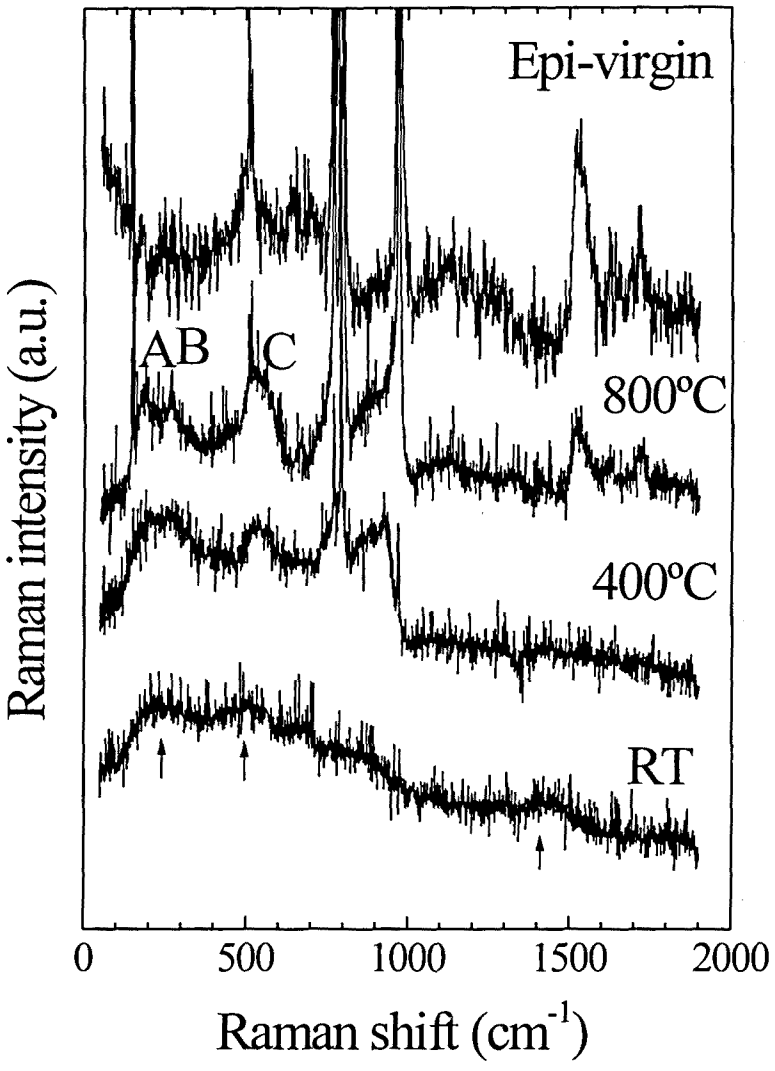

Figure 2.12 Raman spectra from the as-implanted samples, showing the presence of amorphous and disorder induced bands. The spectra are arbitrarily shifted.

2.1.3.2 ANNEALED SAMPLES: DAMAGE RECOVERY

After annealing, the Raman spectra do not show any detectable contribution besides the crystalline vibrational modes. The TO mode I_n values from these samples are also show in the previous figure 2.11. In this case, almost all the samples show very similar values of I_n, corresponding to low damage levels, and only the sample implanted at RT shows higher values of I_n after annealing.

The similar values of I_n for the samples obtained with implantation temperatures higher than RT and annealed suggest a similar content of defects in these layers, in spite of the differences found for implantation temperatures below and above 1000°C. The low values of I_n obtained from these values suggest a significant recovery of the crystal lattice. Residual defects after annealing as vacancy clusters[31] could give rise to the observed residual values of I_n of about 20%. Moreover, the lower defect recovery observed in the sample implanted at RT is related to the amorphisation of the sample during the implantation, with the partial destruction of Si-C bonds and the formation of Si-Si and C-C bonds. The defective nature of the recrystallised layer could be related to the degradation of the electrical activation of the implanted Al^+ ions. This agrees with previous observations by Kawase et al[37], which show high leakage current values from diodes obtained in layers amorphised during implantation and recrystallised at 1500°C.

Hall effect and conductivity measurements have been performed in order to confirm the degradation of the electrical activation of the implanted Al ions for the sample implanted at RT and annealed. All this corroborates the need to avoid the amorphisation of the implanted layer before annealing, which is related to the lack of a solid phase epitaxy process in SiC. For the samples implanted at higher temperatures, the electrical measurements give similar values of effective Hall concentration ($3.5x10^{17}$ cm^{-3} at 50°C) and electrical conductivity[36] (1.5Ω cm at 50°C). This agrees with the similar levels of residual damage in the samples, as estimated from the normalised intensity of the Raman modes, and contrasts with the structural differences observed before annealing.

2.2 CHEMICAL ORDER DEGREE IN AMORPHOUS SiC

The data obtained from the ion beam amorphised SiC show the presence of structural differences in the chemical order in relation to the SiC crystalline phases. These issues are critical for the recrystallisation behaviour of the structures, as this is determined by the different characteristics of the possible involved bonds, mainly the bond length and the binding energy. In order to deepen in the study and characterisation of chemical order in amorphous SiC, the detailed analysis of amorphous films formed by C implantation into pre-amorphised Si substrates has been performed. In this case, the ion implantation technique has more advantages with respect to other techniques of material's production, because it allows the formation of an amorphous $Si_{1-x}C_x$ layer with gradual composition in a straightforward way, related to the gaussian-like distribution of the implanted ions in the material. Then, the in-depth analysis of the implanted samples allows their study as a function of the chemical composition. Previously to the results, the theoretical limit cases of fourfold co-ordination in binary systems will be presented.

2.2.1 THEORETICAL SYSTEMS

For a fourfold co-ordinated $A_{1-x}B_x$ binary system, three different limiting cases of chemical arrangement[8,38,39] exist:

i) a complete phase separation,
ii) a perfect mixing, and
iii) a complete chemically ordered system.

In the first case, only homonuclear A-A and B-B bonds are observed with probabilities (1-x) and x, respectively. The second case corresponds to the absence of chemical order, in which a random distribution of bonds occurs. Then, the probability of occurrence of the different bonds is given by $(1-x)^2$ for A-A, $2x\cdot(1-x)$ for A-B and x^2 for B-B. In the third case, a maximum concentration of heteronuclear bonds is observed, due to its higher stability. In this case, the relative concentration of the different bonds depends on the value of x, as all the minority atoms are heterobonded. For $x<0.5$ (an A rich material), the probabilities of occurrence of the bonds are 1-2x (A-A), 2x (A-B) and 0 (B-B). For $x>0.5$ (a B rich material), these are given by 0 (A-A), 2(1-x) (A-B) and 2x-1 (B-B). A comprehensive explanation of these three possible limit configurations is shown in figure 2.13.

As a consequence, the study of the chemical structure and co-ordination requires the analysis of samples with different composition, x.

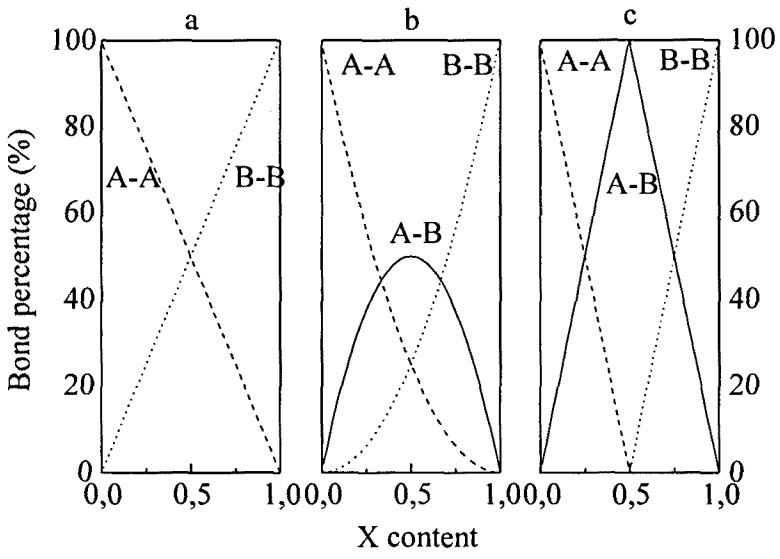

Figure 2.13 Probability of occurrence of the difference types of bond in a fourfold co-ordinated $A_{1-x}B_x$ system for the three limit cases: a) complete phase separation, b) perfect mixing and c) complete chemically ordered system.

2.2.2 CARBON IMPLANTED IN Ge-PREAMORPHIZED SILICON

In this study, the (100) Si wafers were previously amorphised by implanting $5x10^{14}$ Ge^+ ions/cm^{-2} with energy of 200 keV. During implantation, the wafers were cooled down to keep them close to RT. This implantation produced an amorphous Si surface layer of about 175 nm thick, as observed by TEM and Raman. Subsequently, part of the wafers was implanted with C at an energy of 25 keV and a dose of $4x10^{17}$ cm^{-2}. This implantation was also performed at RT. Figure 2.14 shows the TRIM simulated C profile. According to this simulation, the threshold dose for the formation of stoichiometric SiC in the implanted peak is of about $3.7x10^{17}$ cm^{-2}. As a result, a $Si_{1-x}C_x$ gradually composed layer with a maximum x just over 0.5 is expected in the implanted region.

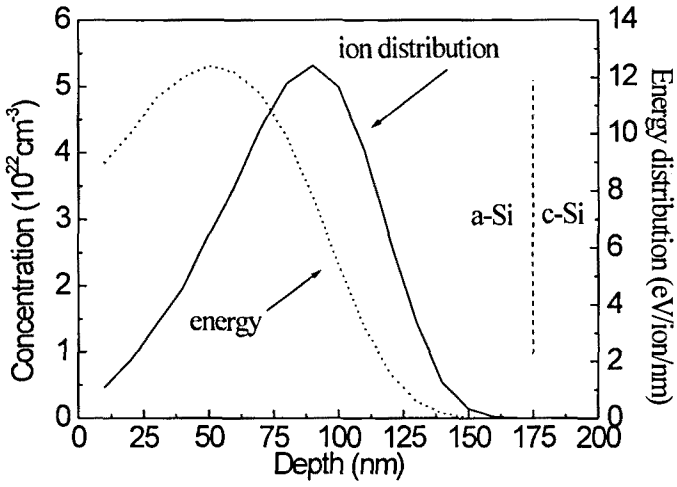

Figure 2.14 TRIM simulation of C^+ implanted in Si substrate, at 25 keV and $4x10^{17}$ cm^{-2}.

The distribution of the C implanted ions has been investigated mainly by XPS, by measuring the Ar2p, C1s, Si2p and O1s spectra. As already indicated in the first chapter, in-depth XPS data were achieved by measuring the spectra after sputtering the samples to different depths with an Ar^+ ion beam at 4 keV. In figure 2.15, typical XPS profile spectra are shown. Axes are binding energy in eV, depth in cycles and counts in arbitrary units. Cycles are proportional to sputtering time (or depth) and the area of the peaks is related to the composition in percentage. It is remarkable that the Ar spectra (not shown) referred to the Ar deposited in the sample measured at different depths, always show the same shape and position, indicating the absence of charge effects during these measurements in the implanted layers. Moreover, no significant O contribution has been measured, except at the surface due to the native surface oxide and surface contamination.

The Si and C concentration profiles from the C as-implanted sample are plotted in figure 2.16, as measured from the area of the Si2p and C1s peaks after their baseline correction and taking into account their different sensitivity factors. A surface C peak appears and, at the buried implanted region, there is a maximum content of C of about 55%. This agrees with the fact that the implantation dose was above the threshold value for stoichiometric concentration.

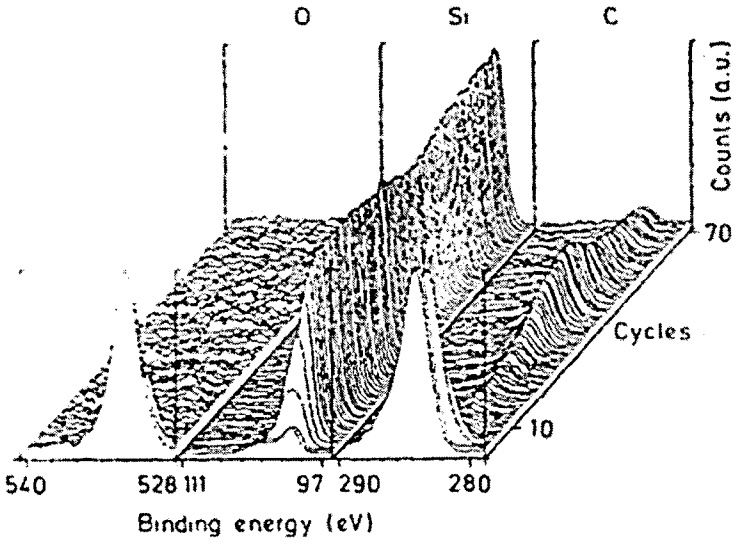

Figure 2.15 XPS spectra for C implanted Si sample. O1s, Si2p and C1s are measured at different depths.

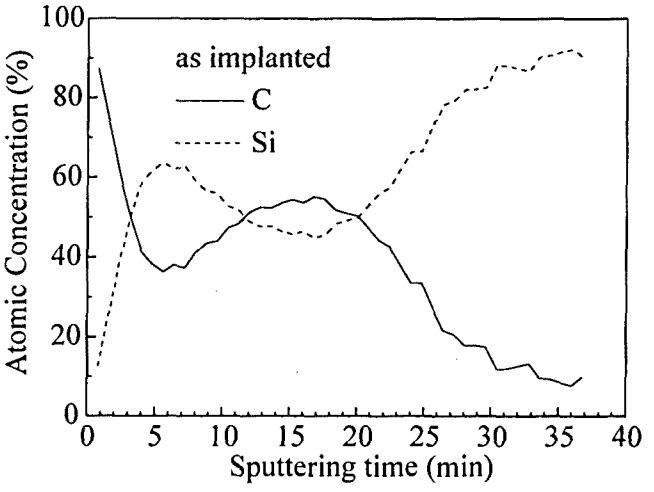

Figure 2.16 Si and C profiles as measured by XPS versus sputtering time from the sample C as-implanted at RT, 25 keV and $4x10^{17}$ cm^{-2}.

Moreover, the C1s and Si2p XPS spectra measured at different depths show changes in their shape and energetic position, in addition to the changes in the peak area. This indicates the existence of changes in the chemical environment of both Si and C atoms in the implanted layer, determined by the presence of the different Si-C, C-C and Si-Si bonds. The fitting of the XPS spectra has allowed the quantification of the different bond contributions. For this, the Si2p spectra have been fitted with two gaussian-like components indicated in Table II-II.

Bond contribution	Peak (eV)	FWHM (eV)
Si-Si	99.3	1.5
Si-C	100.2	1.5
C-Si	283.0	1.6
C-C	284.2	1.5

Table II-II Peak energy and FWHM of gaussian components of XPS Si2p and C1s spectra.

The first component in the table corresponds to those measured in the Si reference wafers, as well as in the Si crystalline substrate far from the implanted region. The second component agrees with those reported for stoichiometric SiC[21,40-42]. According to these data, the first component has been assigned to Si atoms bonded to Si, and the second one to Si atoms bonded to C. In a similar way, the C1s spectra have been fitted assuming the C-Si and C-C contributions indicated in the table. These correspond to the spectra measured in SiC and amorphous C layers, in agreement with the data previously reported in the literature[21,40-42].

Figure 2.17 shows the distribution of the different Si-Si, C-C and Si-C bonds in the C as-implanted layer, as determined from the fitting of the XPS spectra. As expected, the same amount of Si-C bonds is obtained from the fitting of the Si2p and the C1s peaks. According to this figure, about 70% of bonds are Si-C, being this value almost constant in the C implanted region. In these figures, the bond distributions simulated assuming a perfect mixing model and a complete chemically ordered structure have also been plotted. As it is shown, the structure of the implanted layers does not correspond to any of these theoretical simple models, being the bond concentration profiles between those predicted by the perfect mixing and complete chemically ordered cases, in all the cases.

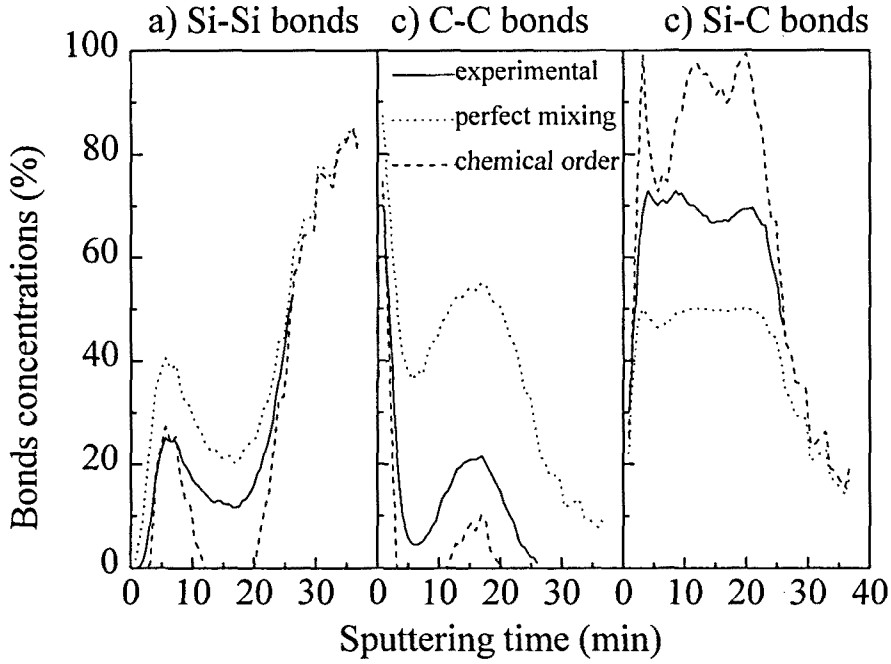

Figure 2.17 Relative distribution profiles of Si-Si, C-C and Si-C bonds versus sputtering time, determined by the fitting of the XPS spectra and simulated assuming the perfect mixing and the complete chemically ordered models.

The percentage of heteropolar bonds as a function of the composition of the $Si_{1-x}C_x$ alloy is plotted in figure 2.18, with those corresponding to the perfect mixing and complete chemically ordered cases. This figure, together with the previous ones, shows the existence of a partial chemical order in the SiC amorphous layer obtained by ion implantation into amorphous Si.

For the composition range $0.35<x<0.6$, there is a saturation of the percentage of heteropolar bonds at 70%, in between the values expected for the complete chemically ordered case (100% of heteropolar bonds for x=0.5) and for the perfect mixing case (50% of heteropolar bonds for x=0.5). This result agrees with the previous Raman scattering measurements performed on ion-beam amorphous SiC (in section 2.1.2).

Moreover, the presence of a 70% of heteronuclear bonds in amorphous SiC has also been reported by Zorba et al[27] from the analysis of the FTIR spectra measured on samples similar to those studied in the previous section (6H-SiC amorphised by Ge^+ ion implantation). This indicates that amorphous SiC synthesised by C^+ ion implantation into pre-amorphised Si has a similar structure to that of ion-beam amorphised 6H-SiC films.

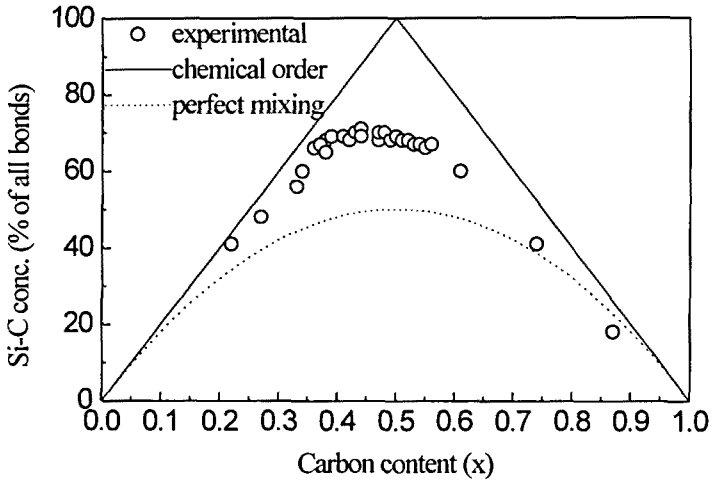

Figure 2.18 Percentage of heteropolar bonds versus chemical composition 'x' of the $Si_{1-x}C_x$ alloy, as determined from the fitting of the XPS spectra, together with those predicted in the perfect mixing and complete chemically ordered cases.

The existence of an intermediate situation in between the complete chemical order and the complete mixing cases in amorphous stoichiometric SiC has been theoretically predicted by Finocci et al[18]. However, the experimental data in the present work show a higher degree of chemical order in the amorphous SiC alloy, obtaining a percentage of homopolar bonds of about 70%, which is higher than that simulated by Finocci et al (of about 55-60 %).

On the other hand, Takeshita et al[39] have interpreted the XPS data from glow discharged amorphous SiC layers in terms of the complete chemical order with the homogeneous dispersion model (COHD). In this model, the spectra arise from five possible contributions corresponding to the different tetrahedral bonding configurations ($Si\text{-}Si_{4-n}C_n$ and $C\text{-}C_{4-n}Si_n$ with n=0-4) averaged according to the different bond probabilities predicted for the different theoretical models[38].

Due to the small energy difference between the contributions from consecutive tetrahedras, which are of the order of the energy resolution in the experimental measurements (about 0.2-0.3 eV), Takeshita et al adopted a weighted average method to fit the peak energies of the experimental spectra assuming a complete chemically ordered system. In this method, only the peak position of the spectra was taken into account. Although a good fitting was obtained for the peak position of the Si 2p line, the data for the C1s line did not fit with the model, observing the presence of changes in the peak position of the C1s peak for Si rich layers, for which the model predicts the absence of Si-C heteropolar bonds. To explain these data, the authors claimed the presence of induction effects and shifts in the Fermi level affecting the position of the C1s line.

In the present work, all the spectra have been fitted to determine the different possible contributions. Five possible contributions have been considered. However, this fitting always leads to only two significant contributions, whose characteristics are those indicated in table II-II. For the Si 2p spectra, these contributions correspond to $Si\text{-}Si_4$ and $Si\text{-}C_4$. For the C1s spectra, and taking into account the data previously reported[21,40-42], the contribution at 283.0 eV can be identified with $C\text{-}Si_4$. However, the second contribution (at 284.2 eV) appears at an energy somehow lower than that assumed by Takeshita et al[39] for the $C\text{-}C_4$ one. This disagreement could be related to the high uncertainty of this contribution, which is very small in almost all the spectra. Moreover, in contrast with the previous data from Takeshita et al[39], the results obtained from the Si2p and C1s spectra show the same behaviour, obtaining the same percentage of heteropolar bonds in both cases. In the present case, the presence of only two significant contributions in the XPS spectra strongly suggests the existence of a tendency towards partial chemical ordering with phase separation. This situation is characterised by a strong trend of Si to be tetrahedrally co-ordinated to 4 Si atoms ($Si\text{-}Si_4$) or to 4 C atoms ($Si\text{-}C_4$), and C to be co-ordinated to 4 C atoms ($C\text{-}C_4$) or to 4 Si atoms ($C\text{-}Si_4$). No significant contribution of the intermediate tetrahedral configurations ($Si\text{-}Si_iC_{4-i}$ or $C\text{-}C_iSi_{4-i}$) is detected in the compositional range $0.35<x<0.6$. For C-poor $Si_{1-x}C_x$ ($x<0.35$), the majority of bonds are $Si\text{-}Si_4$ and almost no $C\text{-}C_4$ bonds are detected. In this case, almost all the C tends to be tetrahedrally co-ordinated to Si. This is in agreement with the structural analysis of $Si_{1-x}C_x$ substoichiometric amorphous films obtained by different techniques such as magnetron sputtering[9]. Conversely, the majority of C bonds are $C\text{-}C_4$ for C-rich $Si_{1-x}C_x$ ($x>0.36$).

2.3 RECRYSTALLISATION OF AMORPHOUS SiC

As already indicated, the recrystallisation mechanisms in amorphous SiC are strongly dependent on the structural and chemical ordering of the system. For amorphous films produced by ion implantation in single crystal 6H-SiC, the absence of a Solid Phase Epitaxyal (SPE) crystallisation is clear, and seems to be related to the lack of a complete chemical order when SiC is amorphised. For amorphous SiC films grown in Si substrates, recrystallisation always occurs in a polycrystalline phase, being SiC grains mainly β-SiC, and the needed temperature strongly depends on the C chemical content in the films[43]. In this sense, the presence of C atoms in the Si network determines a drastic increase in the temperature needed for recrystallisation in comparison with that required in Si, which would be related to the high content of C-C bonds in the structure. In general, this leads to the formation of complex nanocrystalline system with Si, β-SiC grains and C-graphitic domains, as a function of the initial C content.

In this section, the study of recrystallisation of ion beam synthesised SiC grains on Si is performed by two different processes: thermal annealing and Ion Beam Induced Epitaxial Crystallisation (IBIEC). While by thermal processes high temperatures are necessary to reach a whole reconstruction of the structure, by using IBIEC processes seems possible to reduce these high temperatures.

2.3.1 THERMAL RECRYSTALLISATION

Thermal recrystallisation has been mainly investigated in Si (100) wafers implanted at RT with a high dose of C atoms (150 keV, $4x10^{17}$ cm^{-2}). For these implantation conditions, the layer is amorphised during the implantation process. Figure 2.19 shows the TRIM simulated profile of the implanted atoms. According to TRIM, the implanted dose is not enough to form a stoichiometric SiC film close to the projected range because the threshold dose for the formation of such a SiC layer is $8.9x10^{17}$ cm^{-2}. Pieces from these wafers have been annealed in a conventional furnace at 950°C and 1150°C during 10 hours.

Figure 2.20 shows the infrared absorption spectra from different wafers. These spectra are characterised by the presence of an absorption peak at about 700-800 cm^{-1}.

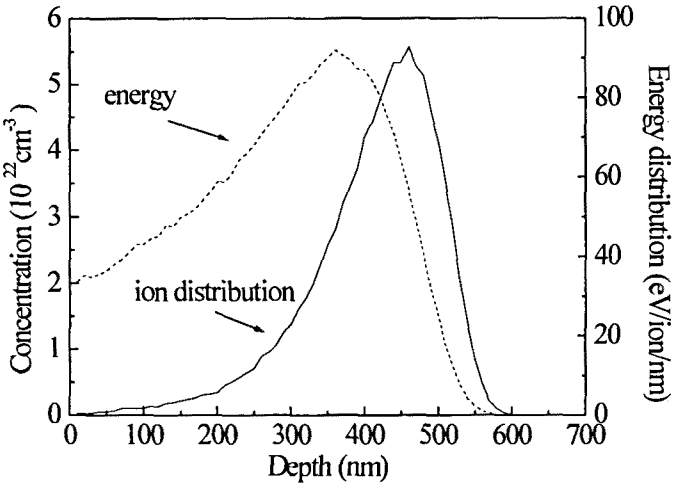

Figure 2.19 TRIM simulation of C^+ implanted at 150 keV and $4x10^{17}$ cm^{-2} in Si.

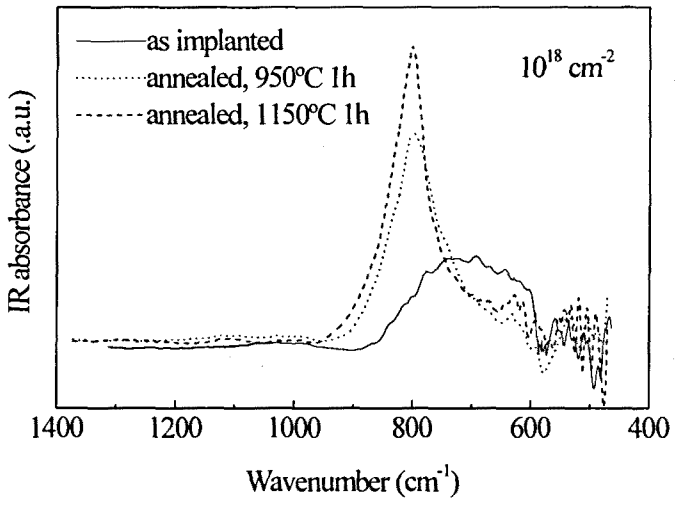

Figure 2.20 Infrared absorbance spectra for Si sample C implanted at 150 keV and $4x10^{17}$ cm^{-2}, before and after the annealing procedure.

This band at about 700-800 cm^{-1} is related to the Si-C stretching vibrational TO mode. For single crystal SiC, this mode is also Raman active, and corresponds to the TO (E2) at 789 cm^{-1} in figure 2.1. For amorphous SiC, the loss of shift range order determines a significant broadening of this band. It has a characteristic gaussian shape with a FWHM of the order of 160 cm^{-1} and the peak appears at lower frequencies, at about 700 cm^{-1}. The presence of this band in the as-implanted sample points out the direct synthesis of an amorphous SiC network by the implant process.

With annealing, the shape of the spectra becomes lorentzian, showing crystallisation of SiC. This is also accompanied by a drastic decrease in the FWHM of the mode, as well as a shift of the peak towards the value 789 cm^{-1}. This indicates that recrystallisation has already taken place at 950°C. By increasing the anneal temperature up to 1150°C, the spectrum becomes similar to the theoretically simulated for single crystal β-SiC, which is determined by an improvement of crystalline quality (decrease of residual stress and structural defects in the SiC grains).

The formation of an amorphous phase after the RT implantation is also clearly deduced from Raman measurements. The spectra measured in samples as-implanted and annealed at the highest temperature are plotted in figure 2.21. These spectra have been measured in backscattering Raman configuration with the 514 nm line from the Ar^+ laser. The spectra from the as-implanted samples show the characteristic bands of amorphous Si, superimposed to the attenuated first order peak from crystalline Si (c-Si, about 520 cm^{-1}). The second order peaks of crystalline Si are not visible, due to the amorphisation of Si in the scattering volume. In addition, a broad band in the 1350-1580 cm^{-1} region appears, which corresponds to C-C bonds. This indicates the amorphisation of the implanted samples for the RT implantation, with the presence of Si-Si and C-C bonds.

After annealing, the amorphous Si contribution in the spectra disappears and the first and second order peaks from c-Si are restored. This can be seen in the spectrum plotted in figure 2.21, which clearly shows the peak at 302 cm^{-1} (2TA(X)) and the second order band at the 900-1000 cm^{-1} region, associated with overtones and combinations involving optical phonons[44], in addition to the first order line at 520 cm^{-1}. Moreover, no peaks directly related to Si-C or C-C bonds are observed. The absence of any Si-C contribution in the spectra is likely to be related to the strong difference in optical absorption between crystalline Si (with very strong absorption for the 514 nm light) and SiC (which has a very weak absorption in the visible region). This determines that almost all photons are absorbed in the Si regions.

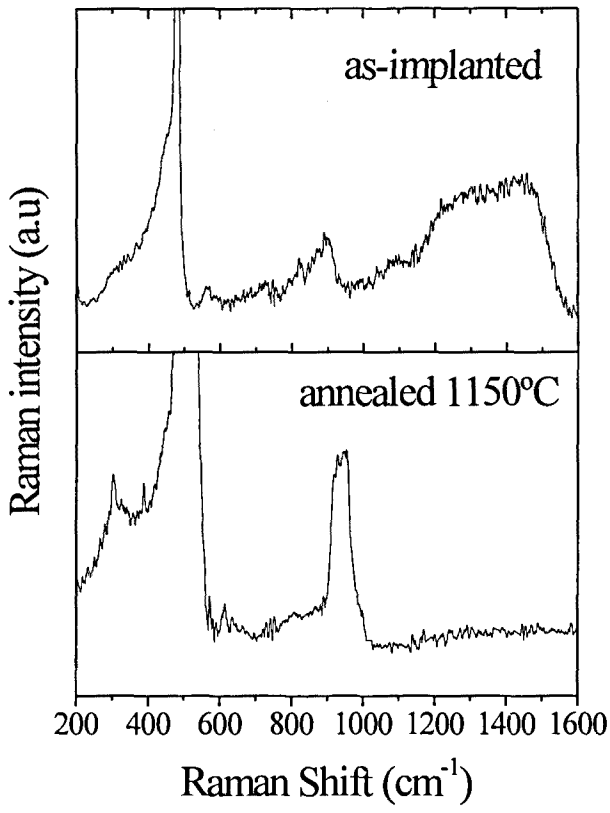

Figure 2.21 Raman scattering spectra from samples as-implanted and annealed at 1150°C.

A cross-section TEM image of the annealed sample is shown in figure 2.22. The first remark to be made is the small surface rugosity. Down to a thickness of 150 nm the layer is Si with precipitates, mostly spherical or octahedral in shape. Transmission electron diffraction diagrams did not reveal any crystallinity from these precipitates. The second layer is a 190 nm thick buried polycrystalline layer, limited on the top and bottom by regions with twins defects, the upper one is about 40 nm thick, while the lower is 70 nm thick. Both regions are formed after the annealing from the recrystallisation of the amorphous layer formed during the RT implantation.

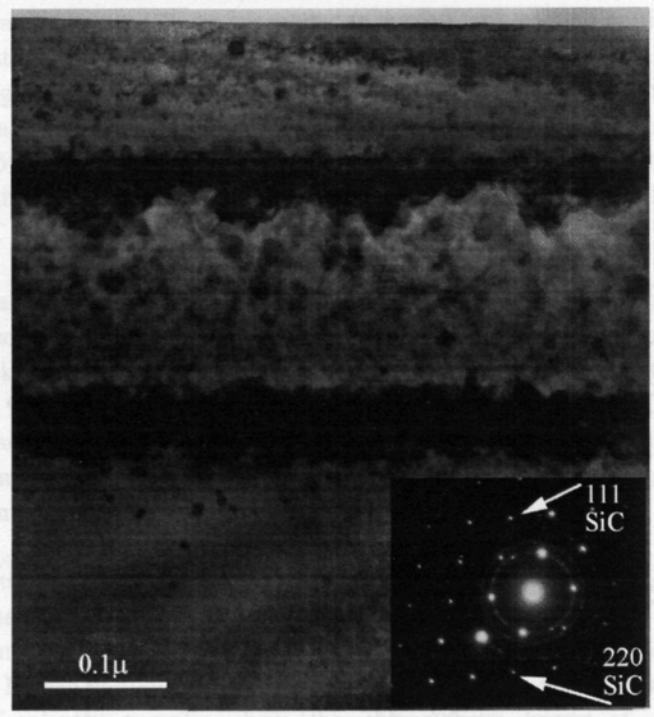

Figure 2.21 Cross section TEM image of the C implanted ($4x10^{17}$ cm^{-2}) sample at RT and annealed at 1150°C for 10h.

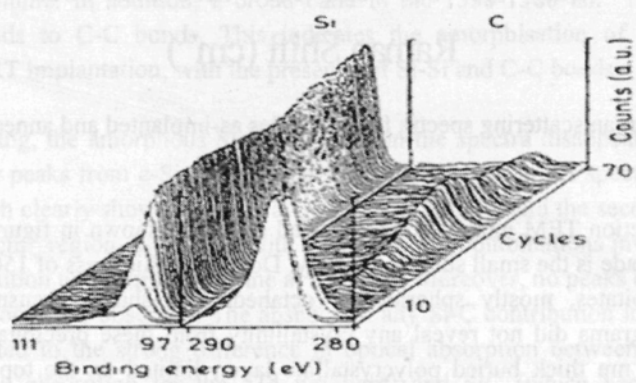

Figure 2.23 Si2p and C1s XPS spectra measured at different depth in the sample as-implanted at RT, 150 keV and $4x10^{17}$ cm^{-2}.

The inset in the figure is a diffraction diagram from the top Si (spots) and from the buried layer (rings), and shows the polycrystalline nature of this layer. The presence of polycrystalline β-SiC, already deduced from FTIR results, is confirmed by the presence of some extra rings. These crystalline SiC grains are randomly oriented. Finally, below the lower twinned layer some small precipitates are also visible, probably being amorphous SiC.

Figure 2.23 shows the XPS in-depth spectra measured in an as-implanted sample. The O spectra (not shown in the figure) reveal the absence of O contribution except at the surface, due to the presence of the native surface oxide and surface contamination. Moreover, the Ar spectra (not shown in the figure) measured at different depths have always the same shape and position. This confirms that no charge effects take place during the XPS measurements in the implanted layers, and there are no changes in the position of the Fermi level as the measured depth increases. According to this, the changes observed in the spectra have to be assigned to changes in the chemical environment. This has been observed in all the measured samples. Moreover, the C1s peaks observed in the two first measured cycles correspond to surface contamination. After those, there are two regions with a significant C content, a thin region just below the surface and the buried region corresponding to the implantation peak. In the subsurface region, the intensity of the peak decreases with depth and appears at values above 284 eV. By increasing the depth, the peak shifts towards 283 eV, becoming similar to the peak measured in the buried region. According to the previous table II-II, this indicates the presence of a C rich layer in the surface region, with a dominant contribution of C-C bonds, and correlates with the features observed in the Raman spectra.

As the depth increases, the C content decreases, and the peak tends to the value corresponding to SiC. In the buried layer, only the SiC contribution is obeserved in the peak. In agreement with C1s, the Si2p spectra after deconvolution show the presence of the two contributions, assigned to the $Si\text{-}Si_4$ and $Si\text{-}C_4$ configurations in table II-II. The fitting of the spectra with these contributions has allowed to determine the in-depth distribution of the percentage of Si atoms in both Si and SiC phases.

The percentages for the samples implanted at the higher doses, as measured by XPS, are plotted in figure 2.24. The SiC phase shows a surface maximum (with about 80% of Si atoms bonded to C) that corresponds to the surface C rich SiC region. At the implantation peak, about 47% of Si atoms are bonded to SiC, and 53% are bonded to Si. After annealing, the surface peak disappears and the percentage of Si atoms in the SiC phase slightly increases to about 52%, the remaining being Si atoms bonded to Si.

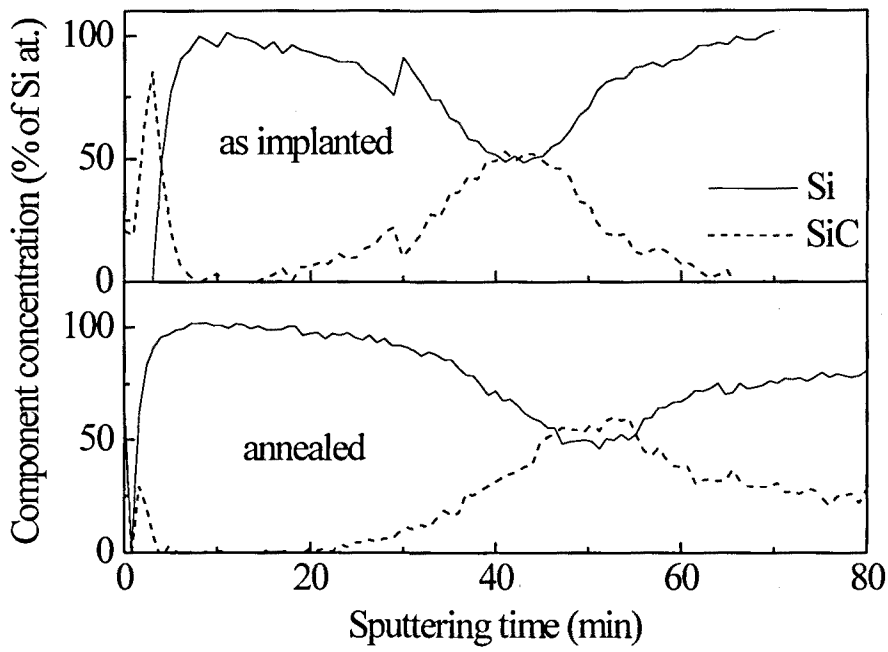

Figure 2.24 Percentage of Si atoms in Si (solid line) and SiC (dotted line) phases as measured by XPS, versus sputter time from samples implanted at RT and $4x10^{17}$ cm^{-2}.

According to these XPS data, a stoichiometric continuous buried layer is not achieved as expected, in spite of the implanted dose. This is directly connected with the excess of C close to the surface.

All these data point out the existence of two different mechanisms during the implantation process:

a) C migration towards the surface, similar to a surface gettering mechanism, and
b) formation of a buried amorphous SiC layer of gradual substoichiometric composition.

Both mechanisms are competitive, and are found to take place. The phases induced by the high dose implantation at RT are amorphous, according to the Raman and FTIR data. The co-existence of both mechanisms leads to the formation of a C rich surface layer, in addition to the buried one. The high content of C in this surface layer determines a dominant contribution of C-C bonds, according to the previous analysis performed in section 2.2. By increasing in depth, the C signal moves towards the C-Si_4 component as a consequence of the decrease in the C content, which causes an increase in the amount of Si-C bonds. At the buried peak, both Si-Si_4 and C-Si_4 tetrahedral configurations exist, and no C-C_4 contribution is detected. This is related to the substoichiometric composition of the $Si_{1-x}C_x$ layer, which fixes a very low probability of occurrence of the C-C bond, being almost all C tetrahedrally co-ordinated to Si.

An annealing at 900°C already leads to the disappearance of the C-surface film, as well as, to the formation of a buried polycrystalline layer with randomly oriented Si and β-SiC grains. Out-diffusion of C from the implanted samples has been previously observed as a result of the formation of C-O bonds with residual O content in the annealing atmosphere, which tend to out-diffuse as CO from the sample[45]. Finally, it is worth remarking the increase in the crystalline quality of the SiC grains, which is achieved at the highest annealing temperature, as shown in the TEM images.

2.3.2 ION BEAM ASSISTED RECRYSTALLIZATION: IBIEC PROCESS

Apart from the thermal recrystallisation considered before, another possibility way of reconstructing the structure from the amorphous phase to the crystalline one is the IBIEC process. The interest of this process lies on the fact that the temperature can be reduced and the crystalline quality of the recrystallised films in Si technology can be increased, avoiding some of the problems related to the thermal recrystallisation of SiC layers, which have been indicated in previous sections. The following section is a review of IBIEC and its use mainly in Si technology, while in section 2.3.2.2 the use of this process for the recrystallisation of ion beam synthesised amorphous films in Si is presented.

2.3.2.1 IBIEC: ION BEAM INDUCED EPITAXIAL CRYSTALLIZATION

Solid Phase Epitaxial (SPE) crystallisation is the transition process of an amorphous film to a crystalline phase similar to that of the substrate, produced by a planar motion of the amorphous-crystalline (a-c) interface. The growth rate of epitaxial recrystallisation is strongly dependent on temperature and it presents an Arrhenius-like behaviour. At low temperatures, this value is too low and the amorphous to crystal transition is kinetically inhibited.

However, epitaxial recrystallisation can also be promoted at low temperatures by means of ion beam irradiation. This phenomenon represents an example of a dynamic annealing process and it is usually referred to as ion-beam induced epitaxial recrystallisation (IBIEC)[46]. A schematic illustration of the disordering-ordering mechanism induced by ion beam bombardment is plotted in figure 2.25.

In principle, two effects drive the planar a-c interface movement, IBIEC and ion beam induced amorphisation (IBIA). The velocity of the a-c interface movement depends on three important parameters: the target temperature, the ion dose rate and the nuclear energy deposition of the ion beam near the a-c interface. It seems that the same basic processes are responsible for IBIEC as well as for IBIA. Then, the ion dose rate and the target temperature determine whether IBIEC or IBIA occurs[47]. At the well-defined reverse temperature (T_R) both crystallisation and amorphisation processes are in balance and the a-c interface remains on this place. At target temperatures above T_R crystallisation always occurs, and at temperatures below T_R amorphisation takes place. This critical temperature of dynamic equilibrium is strongly dependent on the ion dose rate.

2.3.2.2 IBIEC PROCESSING OF ION BEAM SYNTHESISED AMORPHOUS SiC FILMS

IBIEC has been investigated in amorphous films synthesised by C ion implantation in preamorphised Si substrates. For this, a preliminary Ge implantation at an energy of 200 keV and a dose of $5x10^{14}$ cm^{-2} was performed, leading to a 175 nm thick amorphous layer. Later, C was implanted at RT with an energy of 25 keV and dose of $4x10^{17}$ cm^{-2}. These films have been structurally characterised, and the analysis of the chemical ordering in the $Si_{1-x}C_x$ film has been presented and discussed in section 2.2.2.

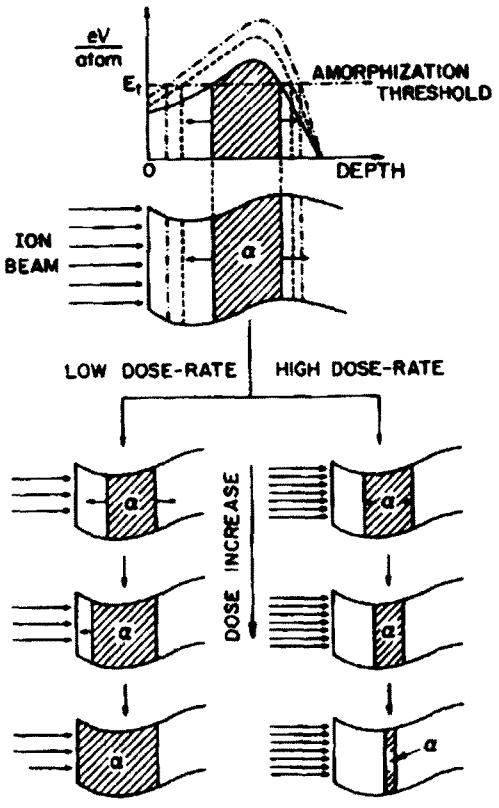

Figure 2.25 Disordering-ordering mechanism induced by ion bombardment in Si.

For IBIEC, pieces from the implanted samples have been subjected to a Si irradiation at 700°C with an energy of 300 keV and a dose of 10^{17} cm^{-2}. The projected range of the Si ions has been estimated by TRIM as 455 nm, well below the amorphous-crystalline interface. Only part of the samples were irradiated with Si, and the part of the sample that was not irradiated has been analysed in order to determine the effects of thermal annealing at 700°C on the amorphous layers.

Figure 2.26 shows the FTIR spectra measured in the as-implanted samples and recrystallised by thermal annealing and an IBIEC process, together with their fitting with gaussian and lorentzian curves.

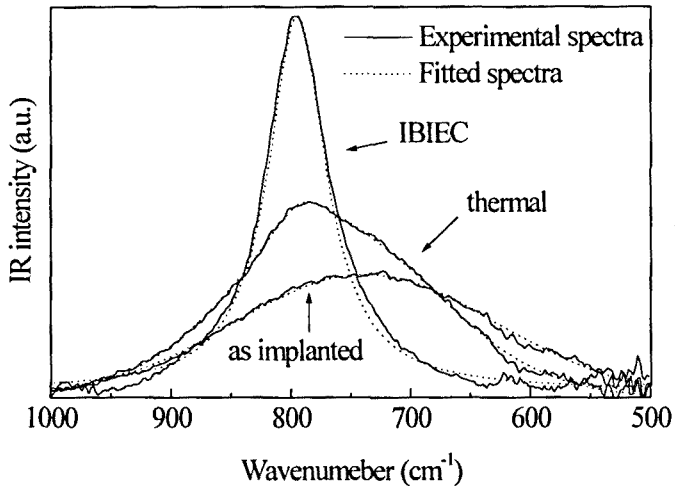

Figure 2.26 Infrared absorbance spectra from the samples as-implanted, thermally annealed and IBIEC processed, together with their fittings (dashed lines).

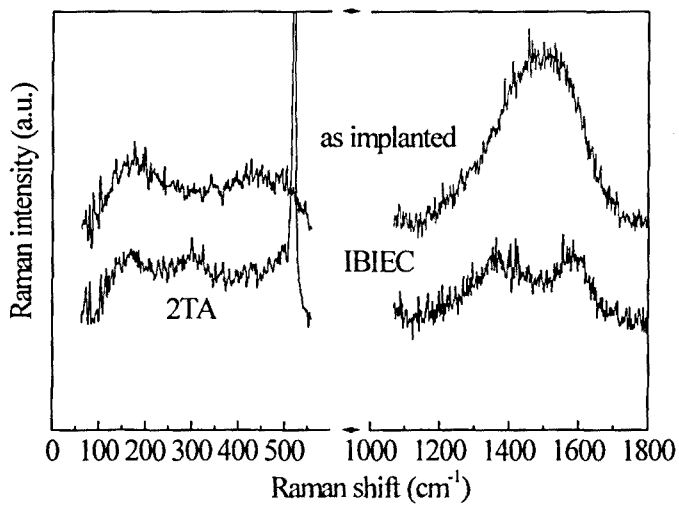

Figure 2.27 Raman spectra in the 100-600 and 1200-1800 cm^{-1} spectral regions from the samples as-implanted and IBIEC processed.

As it is shown, the spectrum of the C as-implanted sample is characterised by a broad absorption band, gaussian in shape, centred at about 737 cm^{-1} with a FWHM of 300 cm^{-1}. As already indicated, this corresponds to the Si-C related absorption band, and indicates the presence of Si-C bonds in an amorphous phase after implantation[8]. When annealing this sample at 700°C, a lorentzian contribution (ω_0=795 cm^{-1}, FWHM=48 cm^{-1}) appears in addition to the gaussian band. This indicates a certain thermal recrystallisation of SiC. From the ratio between the amorphous (gaussian) and crystalline (lorentzian) contributions, about 10% of amorphous SiC is estimated to recrystallise. For the IBIEC processed sample, no gaussian signal is observed at all, and only the lorentzian signal from crystalline SiC appears. Its small FWHM indicates a strong crystallisation of the SiC layer by the IBIEC process. Moreover, the different spectra have a similar area, which suggests that all the samples have the same amount of Si-C bonds.

The Raman spectra of these samples are characterised by the presence of bands in the 50-600 and 1300-1600 cm^{-1} spectral regions, which are characteristic of an amorphous material. This can be seen in figure 2.27, where have been plotted the spectra measured in these regions from the C as-implanted and IBIEC processed samples. The Raman spectra measured from the thermally annealed sample (not shown in the figure) are similar to those from the C as-implanted one. For these last samples, the spectra show characteristic features of amorphous SiC, with the presence of broad bands at about 160 and 480 cm^{-1} related to the Si-Si vibrational modes, as well as a broad contribution at 1300-1600 cm^{-1} related to the C-C vibrational mode. This confirms the existence of an amorphous $Si_{1-x}C_x$ network in the as-implanted films already observed from FTIR, which is not significantly distorted by thermal annealing.

For the IBIEC processed sample, there is a strong decrease in the intensity of the amorphous bands. Moreover, the spectrum also shows the presence of the first and second order (2TA) peaks from the crystalline Si substrate (at 520 cm^{-1} and 302 cm^{-1}, respectively). This is due to the recrystallisation of the Si region below the implanted layer (as will be shown in the next section). The absence of any crystalline SiC mode, in spite of the evidence of SiC recrystallisation provided by FTIR, is caused by the weak optical absorption in crystalline SiC, which is orders of magnitude lower than in Si. However, Raman spectra still show amorphous bands. This indicates the presence of a residual amorphous material in the IBIEC processed sample. The C-C spectrum shows a double band centred at 1380 and 1590 cm^{-1}. This is very similar to the spectra reported for amorphous graphitic C[7,8], and has been recently simulated for amorphous C with sp^2 co-ordination. All this strongly suggests C-C bonds in the amorphous material to be in sp^2 co-ordination.

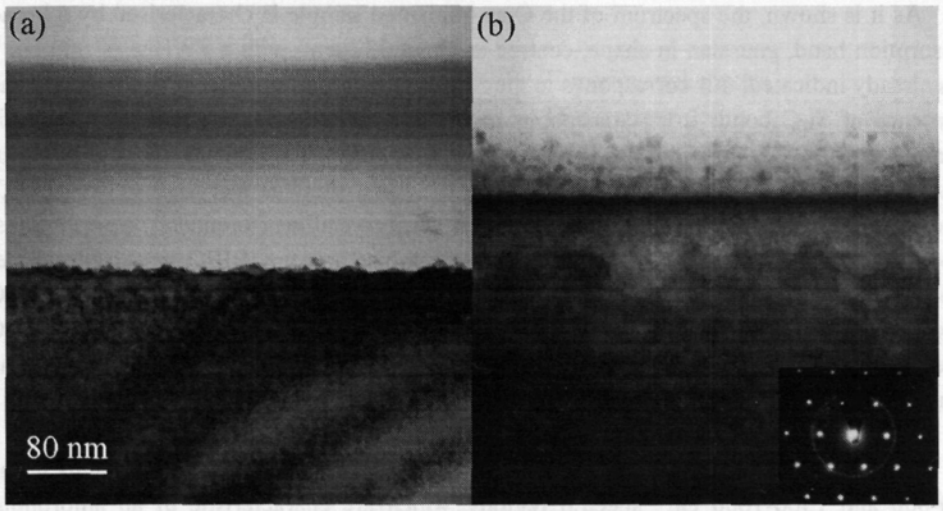

Figure 2.28 *Cross-section TEM image from the samples as-implanted* (a) *and IBIEC processed* (b). The inset is a diffraction pattern from the SiC and Si areas in (b).

Figure 2.28 corresponds to the cross-section TEM image of the as-implanted sample. As it is shown in this figure, there are two different amorphous regions on the crystalline Si substrate. The top darker one, of about 90 nm thick, corresponds to the C implanted layer. An even darker band appears in this region at a depth of about 60 nm, which corresponds to the C implantation peak. Moreover, another dark band can also be observed at the surface. This corroborates the presence of a higher C content at the surface of the sample, as observed from XPS (in section 2.2.2). Between the amorphous C implanted layer and the crystalline substrate, an amorphous Si region is observed. This is the second amorphous region in figure 2.28.

TEM observation of the thermally annealed sample corroborates the recrystallisation of the lower amorphous Si region. However, recrystallisation stops at the C implanted amorphous layer. Moreover, a high density of end-of-range (EOR) defects is observed at the original amorphous/crystalline interface. These defects have been extensively reported in the literature[49-51] and are characteristic of the SPE process. For the IBIEC processed sample the implanted layer also recrystallises, observing SiC nanocrystalline grains.

The TED pattern from this region (inset in the figure) shows the presence of rings corresponding to the randomly oriented SiC grains, in addition to the Si spots. The size of the grains changes with depth, being larger in the central region corresponding to the C implantation peak, with sizes of about 10-20 nm. Below this layer, crystalline Si is observed, though it appears heavily damaged due to the Si irradiation performed during IBIEC. However, no EOR defects related to the enhanced recrystallisation of Si by IBIEC are observed in the amorphous-crystalline interface region.

The chemical-physical analysis of the samples has been performed by XPS measurements. The Si and C XPS profiles after IBIEC processing are plotted in figure 2.29. These profiles are very similar to those from the as-implanted sample, which were discussed in section 2.2.2. The main change is the decrease of the surface C peak related to the C diffusion and gettering at the surface observed for RT implantations.

Figure 2.30 shows the different bond contributions in the IBIEC processed sample, as obtained from the fitting of the XPS spectra. The distribution of bonds is very similar to that from the C as-implanted one shown in figure 2.16. The similar amount of Si-C bonds from the C as-implanted and the IBIEC processed samples is consistent with the fact that the FTIR absorption bands measured on these samples have the same area, as already indicated. The shape of the FTIR spectrum of the IBIEC processed sample points out that all Si-C bonds are in a crystalline phase. Then, according to the Raman spectra, homonuclear C-C and Si-Si bonds, already present in the C as-implanted layer, are not broken by the IBIEC process, remaining in an amorphous phase. Only in those regions with a dominant concentration of Si-C bonds, these bonds are reorganised in a crystalline structure, forming the grains observed by TEM.

According to these data, the IBIEC process is not able to break the homonuclear bonds in the implanted layer, and no significant diffusion of Si or C atoms is observed. This behaviour might be determined by the high stability of the C-C bond, mainly in sp^2 co-ordination, being the energy of this bond very much higher than that of the Si-Si or Si-C ones, 6.42 eV in front of 2.35 and 3.21 eV, respectively. In fact, the change in the shape of the C-C contribution in the Raman spectra from the as-implanted and IBIEC processed samples (shown in figure 2.26) indicates the relaxation of C-C bonds from a mixed sp^2-sp^3 co-ordination characteristic of C-C in the SiC amorphous network to a highly stable graphitical sp^2 co-ordination.

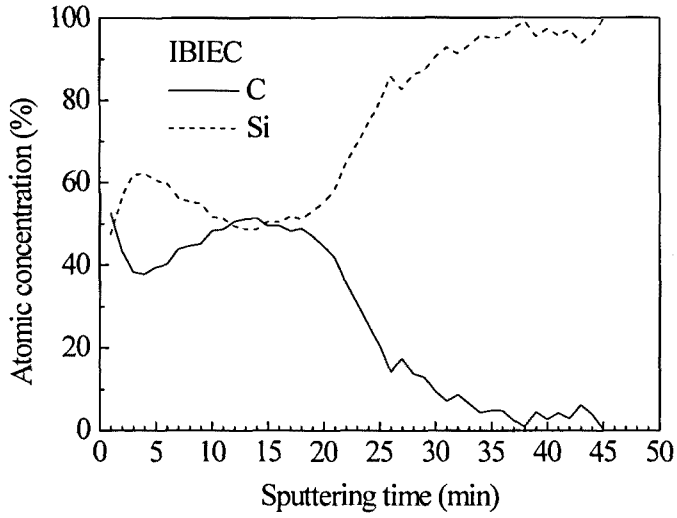

Figure 2.29 Si and C profiles as measured by XPS versus sputter time from the IBIEC processed sample.

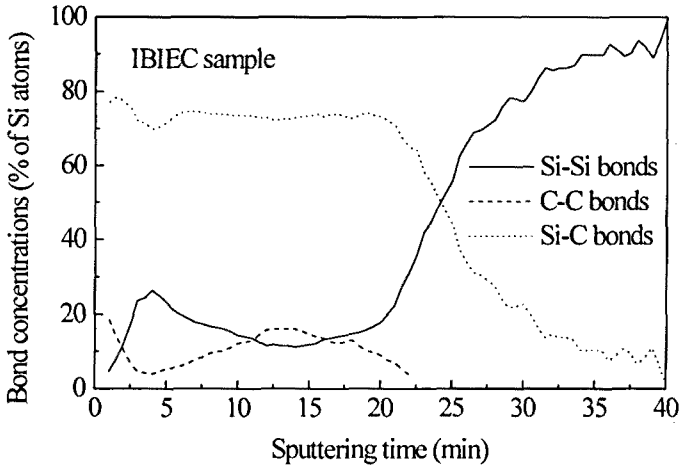

Figure 2.30 Relative distribution profiles of Si-Si, C-C and Si-C bonds in the IBIEC processed sample versus sputter time, determined from the fitting of the XPS spectra.

Thus, the presence of this residual phase in the processed structure is a direct consequence of the lack of a complete chemical order in amorphous SiC. The incapability of the thermal or IBIEC processes to break these hononuclear bonds constitutes a severe limitation for the application of these layers, as graphitic C can degrade the electrical characteristics of the films.

Finally, although a significant reduction in the recrystallisation temperature can be achieved by IBIEC (from 900°C down to 700°C), no enhancement of crystalline quality is observed in the recrystallised film, which shows a structure very similar to that of the thermally recrystallised layers (in section 2.3.1). This agrees with IBIEC in SiC single crystal where irradiation at temperatures higher than 1000°C is needed to avoid random nucleation and grain growth[52].

2.4 CONCLUSIONS

The analysis performed on 6H-SiC samples shows the suitability of Raman scattering to characterise the ion beam processes in SiC, being very sensitive to the presence of damage as well as to the amorphous phases in the scattering volume. Raman scattering measurements have allowed to observe the existence of three different levels of damage as a function of the implantation dose in SiC implanted with Ge^+ ions at RT and 200 keV:

i) low damage level, at doses equal or below $3x10^{12}$ cm^{-2},
ii) medium to high damage level, at doses between 10^{13} and 10^{14} cm^{-2},
iii) formation of a continuous amorphous layer, at doses higher than the amorphisation threshold of about $2\text{-}3x10^{14}$ cm^{-2}.

Moreover, the spectra from the amorphous SiC layers are characterised by the presence of broad bands which have been related to Si-Si and C-C vibrational modes in an amorphous network. This clearly shows the absence of a complete chemical order in the ion beam synthesised amorphous phase. The shape and position of this C-C mode suggest the existence of a mixed sp^2-sp^3 complex hibridation in the C homopolar bonds.

By thermal annealing, recrystallisation and damage recovery occur. However, a residual damage is observed, which cannot be removed at the highest annealing temperature of 1500°C. This points out the high stability of ion beam induced damage. For the amorphous layers, epitaxial recrystallisation cannot be achieved even at 1500°C, which could be related to the loss of chemical order in the amorphous network, bearing in mind the high stability of the C-C bonds.

These features determine the need to avoid amorphisation when doping by ion implantation 6H-SiC wafers, and this can be achieved by heating the wafer during the implantation process. In this framework, the Raman scattering analysis of ion beam amorphised 6H-SiC has been extended to the study of wafers implanted with Al^+ ions as a function of the implantation temperature. The results obtained show the dependence of the ion beam induced damage on the implantation temperature. For temperatures in the range RT-1000°C, point defects are mainly formed and an increase in the implantation temperature leads to a decrease of the residual damage. For higher temperatures, a saturation of damage is observed, which is probably related to the formation of extended defects. Formation of extended defects requires the mobility of point defects as vacancies and interstitials, which probably takes place for implantation temperatures higher than 1000°C.

Annealing at 1500°C leads to a similar level of residual damage, except for the sample implanted at RT, which was the only one amorphised during the implantation. This correlates with the electrical analysis of the layers, which show similar hole concentration and conductivity values for all the samples implanted at temperatures high enough to avoid amorphisation. For the sample implanted at RT, electrical activation of the implanted Al degrades due to the high residual damage in the implanted layer.

The results obtained in ion beam amorphised SiC that show the loss of chemical order have been corroborated for ion beam synthesised amorphous $Si_{1-x}C_x$ films on Si substrates. In this case, the detailed XPS analysis of Si samples implanted with C ions at doses above the threshold for peak stoichiometric composition reveal the existence of an intermediate situation between the perfect mixing and a complete chemically ordered material. For the composition range $0.35<x<0.6$, there is a saturation in the percentage of heteropolar bonds at 70%. This agrees with the data from FTIR analysis of ion beam amorphised 6H-SiC.

Moreover, the analysis of the XPS peaks in terms of the different possible tetrahedrally bonding configurations ($Si\text{-}Si_{4-n}C_n$ and $C\text{-}C_{4-n}Si_n$ with n=0-4) indicates the presence, in all the range of compositions analysed, of two main contributions in each Si and C XPS peaks, corresponding to $Si\text{-}Si_4$ and $Si\text{-}C_4$ in Si XPS peak, and to $C\text{-}Si_4$ and $C\text{-}C_4$ in C XPS peak. This shows a clear trend of the amorphous network towards partial chemical ordering with phase separation, instead of homogeneous dispersion.

The in-depth analysis of the Si wafers implanted with C^+ ions at RT reveals the existence of two mechanisms that compete and take place during the implantation process, the formation of a SiC buried layer and the C migration towards the surface. Thermal annealing at temperatures T>900°C allows recrystallisation of SiC in the form of randomly oriented β-SiC nanograins, as well as the disappearance of the C peak at the surface. The recrystallisation of the SiC amorphous layers is compromised by the high stability of the C-C bands, which evolve from a mixed sp^2-sp^3 co-ordination to a highly stable graphitic sp^2 co-ordination. This secondary phase is likely located the in intergrain region.

On the other hand, Ion Beam Induced Epitaxial Recrystallisation (IBIEC), which is a dynamic process that promotes the epitaxial crystallisation at lower temperatures by means of ion beam irradiation, has been used for the recrystallisation of the ion beam synthesised amorphous layers. This has allowed a significant decrease up to 700 °C in the temperature needed for the recrystallisation, for the used irradiation conditions (Si^+ ions, 300 keV, 10^{17} cm^{-2}). However, no significant improvement in the crystalline quality has been observed in relation to the samples thermally recrystallised at 1150°C.

2.5 REFERENCES

1. *Application notes*, CREE Research Inc.
CREE publications, Durham NC (1999)

2. T. Jawhari, A. Pérez-Rodríguez
Internet Journal of Vibrational Spectroscopy *2/4* p. 6 (1999)

3. D. W. Feldman, J. H. Parker, W. J. Choyke
Physical Review *170* p. 698 (1968)

4. S. Nakashima, H. Katahama, Y. Nakakura, A. Mitsuishi
Physical Review B *33* p. 5721 (1986)

5. W. S. Yoo, H. Matsunami
Journal of Applied Physics *70* p. 7124 (1991)

6. D. Olego, M. Cardona
Physical Review B *25* p. 1151 (1982)

7. S. Nakashima, M. Hangyo
IEEE Journal of Quantum Electronics *25* p. 965 (1989)

8. J. Bullot, M. P. Schmidt
Physica Status Solidi B *143* p. 345 (1987)

9. A. Chehaidar, R. Carles, A. Zwick, C. Meunier, B. Cros, J. Durand
Journal of Non-Crystalline Solids *169* p. 37 (1994)

10. M. Gorman, S. A. Solin
Solid State Communications *15* p. 761 (1974)

11. R. O. Dillon, J. A. Woollam, V. Katkanant
Physical Review B *29* p. 3482 (1984)

12. D. Beeman, J. Silverman, R. Lynds, M. R. Anderson
Physical Review B *30* p. 870 (1984)

13. D. S. Knight, W. B. White
Journal of Materials Research *4* p. 385 (1989)

14. R. E. Shroder, R. J. Nemanich, J. T. Glass
Physical Review B *41* p. 3738 (1990)

15. Y. Pacaud, W. Skorupa, A. Pérez-Rodríguez, G. Brauer, J. Stoemenos, R. C. Barklie
Nuclear Instruments and Methods in Physics Research B *112* p. 321 (1996)

16. J. A. Spitznagel, S. Wood, W. J. Choyke, N. J. Doyle, J. Bradshaw, S. G. Fishman
Nuclear Instruments and Methods in Physics Research B *16* p. 237 (1986)

17. V. Heera, R. Kögler, W. Skorupa, J. Stoemenos
Materials Research Society Symposium Proceedings 339 p. 197 (1994)

18. F. Finocchi, G. Galli, M. Parrinello, C. M. Bertoni
Physical Review Letters *68* p. 3044 (1992)

19. A. E. Kaloyeros, R. B. Rizk, J. B. Woodhouse,
Physical Review B *38* p. 13099 (1988)

20. A. Sproul, D. R. Mc Kenzie, D. J. H. Cockayne
Philosophical Magazine B *54* p. 113 (1986)

21. N. Laidani, R. Capelletti, M. Elena, L. Guzman, G. Mariotto, A. Miotello, P. M. Ossi
Thin Solid Films *223* p. 114 (1993)

22. W. Bolse, J. Conrad, T. Rödle, T. Weber
Surface and Coatings Technology *74* p. 927 (1995)

23. V. Heera, W. Skorupa
Materials Research Society Symposium Proceedings *438* p. 241 (1997)

24. Y. Pacaud, G. Brauer, A. Pérez-Rodríguez, J. Stoemenos, R. C. Barklie, M. Woelskow, W. Skorupa
Institute of Physics Conference Series *142* p.537 (1996)

25. A. Pérez-Rodríguez, E. Roca, T. Jawhari, J. R. Morante, R. J. Schreutelkamp
Thin Solid Films *251* p. 45 (1994)

26. Ch. Wagner, G. Krötz, H. Sonntag, H. Möller, G. Müller, S. Kalbitzer,
Digest of Technical Papers Eurosensors IX *2* p.194 (1995)

27. T. Zorba, C.L. Mitsas, I.D. Siapkas, G.Z. Tezarkis, D.I. Siapkas, Y. Pacaud, W.Skorupa
Applied Surface Science *102* p. 120 (1996)

28. Y. Pacaud, W. Skorupa, J. Stoemenos
Nuclear Instruments and Methods in Physic Research B *120* p. 181 (1996)

29. H. Wirth, M. Voelskow, D. Panknin, W. Skorupa, O. González-Varona, A. Pérez-Rodríguez, J. R. Morante
Journal of Applied Physics, to be published (1999)

30. D. Panknin, H. Wirth, A. Mücklich, W. Skorupa
Materials Science and Engineering, to be published (1999)

31. H. Itoh, T. Ohshima, Y. Aoki, K. Abe, M. Yoshikawa, I. Nashiyama, H. Okumura, S. Yoshida, A. Uedono, S. Tanigawa
Journal of Applied Physics *82* p.5339 (1997)

32 A. Van Veen, H. Schut, J. De Vries, R. A. Hakvoort, M. R. Ijpma,
AIP Conference Proceedings *218* p. 171 (1990)

33. A. Kawasuso, H. Itoh, S. Okada, H. Okumura
Journal of Applied Physics *80* p. 5639 (1996)

34. E. Glaser, A. Heft, J. Heindl, U. Kaiser, T. Bachmann, W. Wesch, H. P. Strunk
Institute of Physics Conference Series *142/3* p. 557 (1996)

35. A. Pérez-Rodríguez, Y. Pacaud, L. Calvo-Barrio, C. Serre, W. Skorupa, J. R. Morante
Journal of Electronic Materials *25* p. 541 (1996)

36. H. Wirth
Ph. D. Thesis, FZR Dresden (1998)

37. D. Kawase, T. Ohno, T. Iwasaki, T. Yatsuo
Institute of Physics Conference Series *142* p. 513 (1996)

38. K. Mui, F. W. Smith
Physical Review B 35 p. 8080 (1987)

39. T. Takeshita, Y. Kurata, S. Hasegawa,
Journal of Applied Physics *71* p. 5395 (1992)

40. E. Ech-chamikh, E.L.Ameziane, A. Bennouna, M. Azizan, T.A. Nguyen, T. López-Rios
Thin Solid Films *259* p. 18 (1995)

41. W. Y. Lee
Journal of Applied Physics *51* p. 3365 (1980)

42. R. C. Lee, C. R. Aita, N. C. Tran
Journal of Vacuum Science Technology A *9* p. 1351 (1991)

43. K. Yoshii, Y. Suzaki, A. Takeuchi, K.Yasutake, H. Kawabe
Thin Solid Films *199* p. 85 (1991)

44. P. A. Temple, C. E. Hathaway
Physical Review B *7* p. 3685 (1973)

45. A. Pérez-Rodríguez, B. Garrido, C. Bonafos, M. López, O. González-Varona, J. Montserrat, R. Rodriguez, J. R. Morante
Journal of Materials Science: Materials in Electronics, in press (1999)

46. F. Priolo, E. Rimini
Materials Science Reports *5* p. 319 (1990)

47. R. Kögler, V. Heera, W. Skorupa, E. Glasser, T. Bachmann, D. Rück
Nuclear Instruments and Methods in Physics Research B *80/81* p. 556 (1993)

48. V. Heera, R. Kögler, W. Skorupa, R. Grötzschel
Nuclear Instruments and Methods in Physics Research B *80/81* p. 538 (1993)

49. J. Desseaux-Thibault, A. Bourret, J. M. Penisson
Institute of Physics Conference Series *67/2* p. 71 (1983)

50. H. Bender, J. Vanhellemont
Physica Status Solidi A *107* p. 455 (1988)

51. A. De Veirman
Ph. D. Thesis, University of Antwerpen (1990)

52. V. Heera, R. Kögler, W. Skorupa, J. Stoemenos
Applied Physics Letters *67* p. 1999 (1995)

CHAPTER 3

DIRECT SYNTHESIS OF CRYSTALLINE SiC

As discussed in the previous chapter, the recrystallisation of ion beam synthesised amorphous SiC presents some problems related to the high stability of C-C bonds in the amorphous phase. This determines the presence in the recrystallised films of graphitic C domains that are probably located in the intergrain regions. In principle, the presence of this secondary phase has to be avoided, due to the possible degradation of the electrical characteristics of the layers.

In order to prevent the formation of homonuclear bonds, ion implantation can be performed at temperatures high enough to avoid the amorphisation of the implanted film. Different authors have reported the implantation of Si wafers with C^+ ions at temperatures higher than 800°C, observing the direct formation of β-SiC grains in the implanted layer with a special orientation in relation to the Si substrate[1-3]. However, implanting at these high temperatures can present some problems related to the enhancement of surface erosion by sputtering during the implantation. This can be important when implanting with high dose values, which are needed to obtain a continuous stoichiometric SiC layer. On the other hand, ion beam heating at high temperatures can lead to the formation of complex defects such as voids or rod-shaped defects[2]. Implanting at these high temperatures also needs implantation machines with complex heating stages.

More recently, Simon et al[4] have reported the formation of crystalline SiC by implanting at temperatures higher than 400°C. However, this is deduced from infrared spectroscopy, and no direct observation of the precipitates and their relationship with the Si lattice is presented. De Veirman[5] has presented some TEM results from implantation at 500°C, but for much lower implanted doses.

Finally, Lindner et al[6-8] have investigated the formation of a buried β-SiC layer by implanting at temperatures in the range between 330°C and 440°C and annealing at 1250°C for several hours. These authors have found that the presence of crystalline SiC precipitates in the as-implanted state is a prerequisite for the formation of the buried crystalline layer after annealing.

Taking into account these results, this chapter focuses on the study of the layers formed by implanting C^+ ions in the Si wafer at a temperature of 500°C. This temperature was chosen so as to avoid the presence of any amorphous phase in the as-implanted state. As is shown in next sections, the formation of a high crystalline quality SiC layer by ion implantation has been achieved, and this has also allowed the synthesis of first microstructures in Si technology, for the micromechanical assessment of the synthesised layers.

3.1 ION BEAM SYNTHESIS OF SiC BY CARBON ION IMPLANTATION AT 500°C: SUBTHRESHOLD IMPLANTATION

In a first step, the implantation of Si wafers with C^+ ions at doses below the threshold one for the formation of a stoichiometric SiC film has been investigated. (001) B-doped device grade Czochralski Si wafers (16-24 ohms·cm) were implanted with different doses between $1x10^{17}$ and $5x10^{17}$ cm^{-2} and at an energy of 300 keV. As calculated by the TRIM simulation, which is shown in figure 3.1, the projected range and straggling are of 707 nm and 115 nm, respectively. For this energy of implantation, TRIM estimates a threshold dose of about $1.1x10^{18}$ cm^{-2}.

As in the previous cases, these and the following implantations in the rest of the chapters have been performed at a tilt of 7° to minimise channelling effects. Samples from the implanted wafers were annealed at different temperatures (up to 1150°C) in a conventional furnace during 10 hours in N ambient. To avoid contamination from the implanted surface during annealing, the surface native oxide layer was removed in HF and a PECVD (Plasma Enhanced Chemical Vapour Deposition) SiO_2 film (1 μm thick) was deposited before annealing.

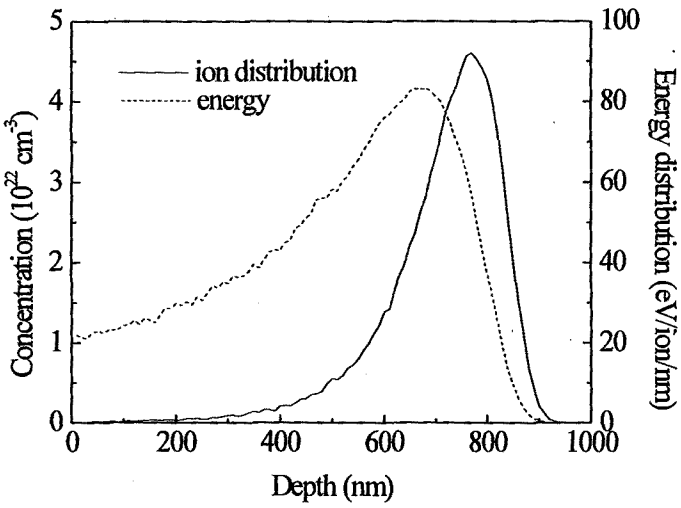

Figura 3.1 TRIM simulation of C^+ implanted at a dose of 10^{18} cm^{-2} in Si.

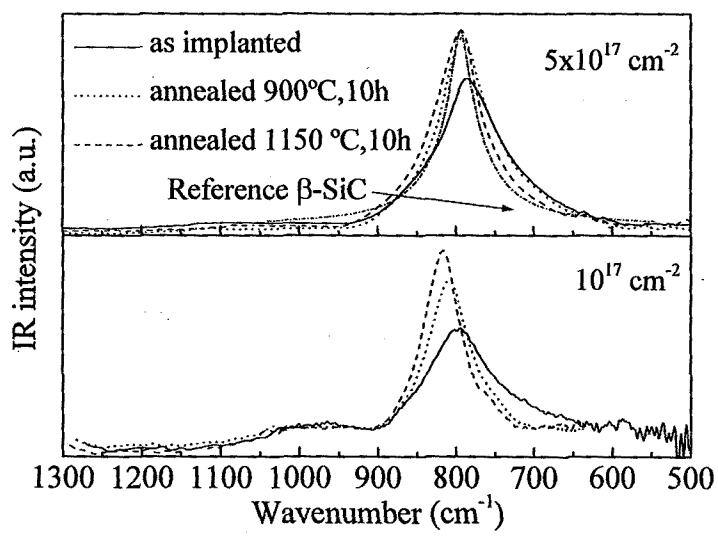

Figure 3.2 Infrared absorbance spectra from implanted samples together with a reference crystalline β-SiC simulated spectrum.

The as-implanted and annealed samples have been analysed by different spectroscopic techniques (FTIR, Raman), electron microscopy and X-ray diffraction. As in the previous chapter, the physico-chemical analysis of the samples has been performed by in-depth XPS measurements.

3.1.1 SPECTROSCOPIC DATA: FTIR AND RAMAN RESULTS

Figure 3.2 shows the infrared absorption spectra from different C as-implanted and annealing samples. In all cases, the spectra are characterised by the presence of the SiC absorption mode which shows a Lorentzian shape characteristic of a crystalline network. For the sample implanted at the dose of $5x10^{17}$ cm^{-2}, the spectrum from the as-implanted sample is rather similar to that of the annealed ones, the SiC peak appears at a wavenumber of 785 cm^{-1} with a FWHM of about 94 cm^{-1}. These values suggest the formation of crystalline SiC already after implantation at 500°C. After annealing, the peak becomes sharper and approaches the value of 797.5 cm^{-1} of the TO phonon of β–SiC. This can be seen in the figure where the reference spectrum from a single crystal β–SiC is also shown[9]. These changes are determined by the improvement of crystalline quality with annealing.

The spectra measured on the samples implanted at lower doses are similar. However, the final position of the SiC absorption peak after annealing at 1150°C appears at a higher wavenumber, about 822 cm^{-1}. According to previous data[10], this could be determined by the lower concentration of SiC precipitates in the implanted layer.

The absence of any amorphous phase in the as-implanted samples is corroborated by Raman scattering. As shown in figure 3.3 no amorphous signal is detected in the Raman spectra, which show the first and second order peaks from crystalline Si (at about 520 and a plateau centred in 950 cm^{-1}, respectively). The asymmetric shape and shift of the first order Raman peak and the lower intensity of all the peaks in relation to the spectrum from not implanted Si indicate the presence of a high density of structural defects. After annealing, the spectra become very similar to that measured in a non implanted Si wafer, due to the improvement of crystalline quality. The corresponding structure in figure 3.3 shows two second order Si peaks, corresponding to LA (315 cm^{-1}) and TO (450 cm^{-1}) modes together with the first order c-Si peak that shows a small residual shift of about 0.15 cm^{-1} towards the low frequency side. This could be determined by the presence of both residual structural defects and residual strain in the Si matrix.

Moreover, for all the implanted and annealed samples no contribution is detected in the Raman spectra in the 1200-1800 cm^{-1} region, which corroborates the absence of C-C vibrational modes in the spectra. The absence of the corresponding Si-C vibrational modes is related to the much higher optical absorption of visible light in Si. According to this, only Si modes from the surface Si layer and substrate regions contribute to the spectra.

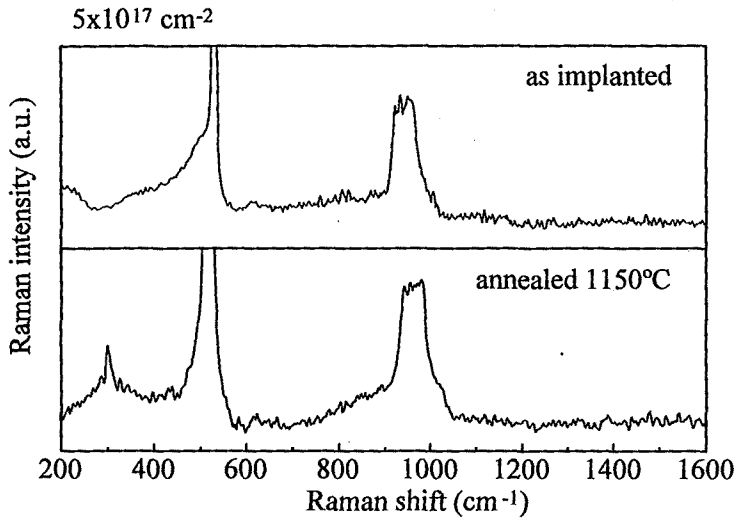

Figure 3.3 Raman spectra from samples implanted at 500°C and a dose of $5x10^{17}$ cm^{-2}.

3.1.2 XPS ANALYSIS

The chemical composition of the implanted layers has been investigated by in-depth XPS measurements (performed at similar conditions than in previous chapter). Firstly, and in contrast with the structure observed in the implantations at RT (in section 2.2), no C rich surface region is observed at all and the C1s peak only shows the contribution from SiC (C-Si_4). Conversely, the Si2p peak can be fitted with two contributions which, according to table II-II, correspond to Si atoms in c-Si and SiC phases (Si-Si_4 and Si-C_4, respectively). Similar spectra are obtained from both the as-implanted and annealed samples. This agrees with the FTIR and Raman measurements, which only show vibrational modes from crystalline Si and crystalline SiC already from the as-implanted wafers.

Figure 3.4 shows the percentage of Si atoms in the Si and SiC phases versus the sputtering time from the sample implanted at the highest dose ($5x10^{17}$ cm^{-2}), as-implanted and annealed. In both cases, very similar depth profiles are obtained what points out the high thermal stability of the implanted layer. As it is shown in the figure, for the as-implanted sample about 63% of Si atoms are in the SiC phase in the implanted peak, and after annealing this percentage increases to about 68%. Then, the buried implanted layer is formed by both Si ad SiC crystalline phases, what agrees with the fact that the implanted dose is below the threshold value for stoichiometric SiC composition at the implanted peak.

The absence of a C rich surface region suggests that C migration towards the surface is inhibited at 500°C in front of the chemical reaction with the Si host atoms, forming SiC. When implanting at 500°C, all the implanted C is bonded to Si forming crystalline SiC, and the distribution of implanted ions is almost not affected by the thermal annealing. In this case, C is stabilised in the SiC crystaline network formed during the implantation, and the high stability of crystalline SiC, with very low mobility of vacancies and interstitials, accounts for the small changes observed after annealing.

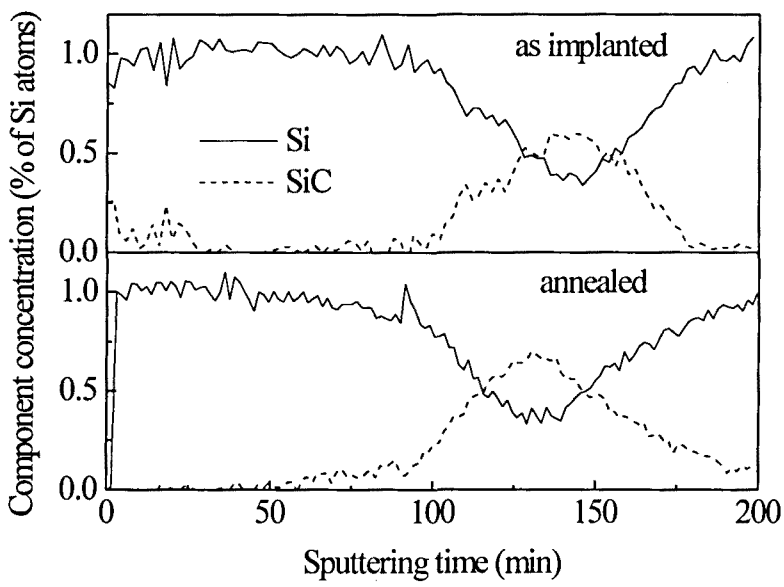

Figure 3.4 Percentage of Si atoms in Si (solid line) and SiC (dotted line) phases as measured by XPS versus sputter time from HT samples implanted at $5x10^{17}$ cm^{-2}. The etching rate was 6 and 4.9 nm/min for as-implanted and annealed samples respectively.

3.1.3 TEM AND XRD ANALYSIS

Figure 3.5 shows cross-section TEM images of the samples implanted at the dose of $5x10^{17}$ cm^{-2}, as-implanted and annealed. Already after implantation, a 500 nm thick buried layer is formed, which contains a very high density of spherical precipitates, of about 7-10 nm in size.

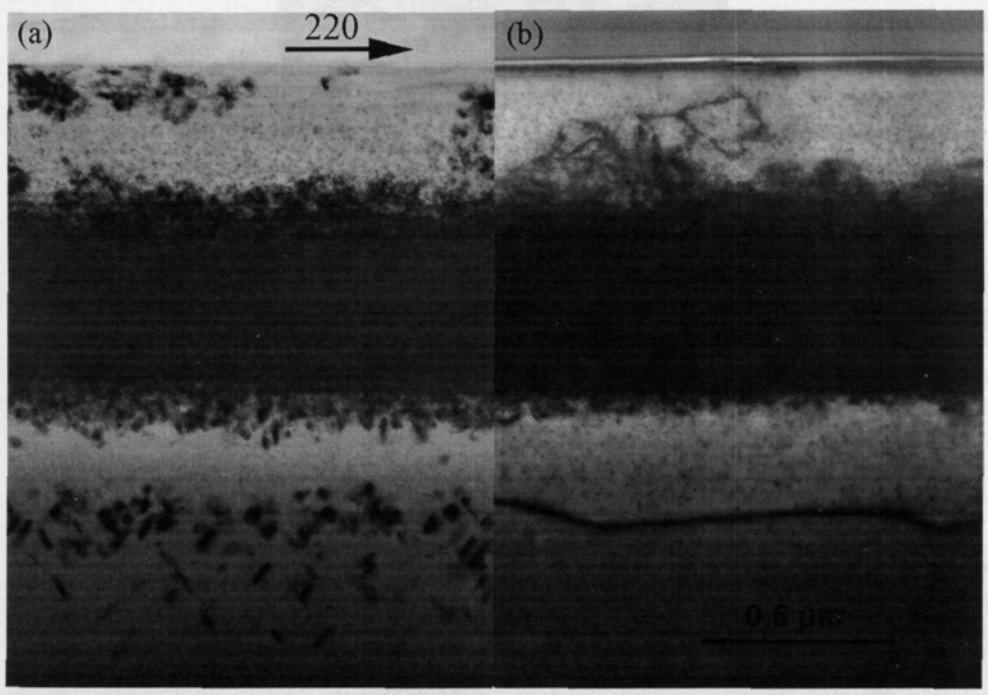

Figure 3.5 Cross-section TEM image of the samples implanted at a dose of $5x10^{17}$ cm^{-2}, a) as-implanted and b) annealed at 1150°C

The electron diffraction pattern shown in figure 3.6 is obtained in a cross-section from this buried area. The pattern confirms that the precipitates are crystalline β-SiC, with an almost perfect alignment in relation with the Si substrate. The relationships between the two lattices are as follows,

$$[001]_{Si} \| [001]_{\beta\text{-}SiC}$$
$$(110)_{Si} \| (110)_{\beta\text{-}SiC}$$

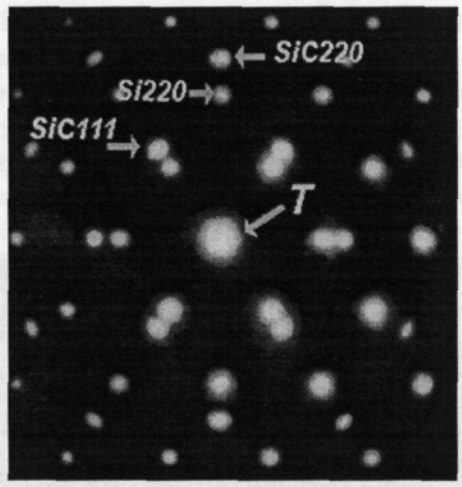

Figure 3.6 Electron diffraction pattern of the buried zone of the as-implanted sample showing the presence of Si and β-SiC spots.

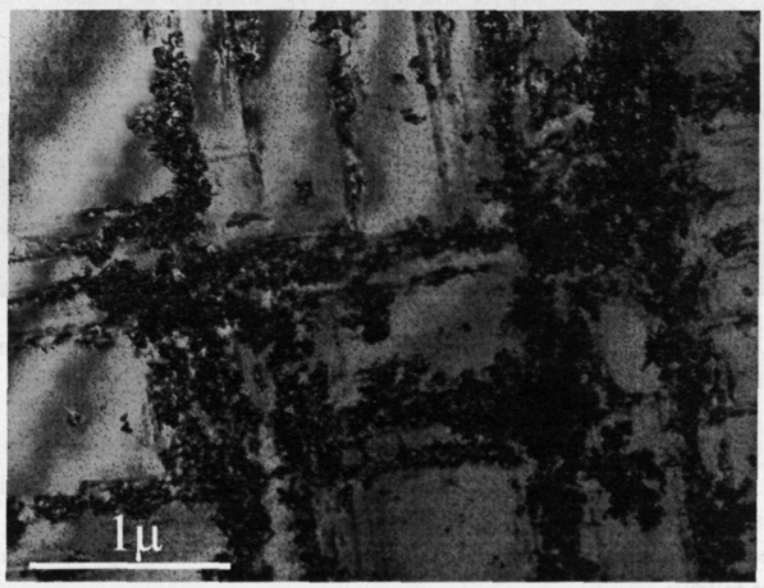

Figure 3.7 Plan view image showing the network-like distribution of the {113}-type defects in the as-implanted sample.

Proceeding towards the surface, the density of precipitates diminishes and a zone denuded of precipitates, of about 70 nm, is seen at the surface. Starting at the surface and down to a depth of about 180 nm, {113}-type defects, also called rod-like defects, are shown. Below the buried layer, a zone denuded of defects is visible at first place, and after that {113}-type defects are formed again. These defects, which are an agglomeration of Si self-interstitials, have also been observed below and, sometimes, above the buried layer synthesised for SOI structures by O and N ion implantation[11]. Plan-view TEM images from this sample show that the upper {113}-type defects are not uniformly distributed throughout the sample but form a network-like distribution, with bands along <110> directions. This result can clearly be seen in figure 3.7, in which some β-SiC precipitates present in the upper Si layer are also visible.

Upon annealing, though some changes occur in the structure, the buried layer remains apparently unchanged despite the annealing temperature and time. The main features observed are the disappearance of the {113}-type defects, as they are only stable up to temperatures of about 700°C, and the formation of dislocations at their place, but mainly below the buried layer. The electron diffraction of the buried zone of this sample, which is plotted in figure 3.8, again shows the presence of β-SiC spots with the same orientation relationship to the Si lattice, although a strong increase in their intensity is evident, indicating an improvement in the crystallinity.

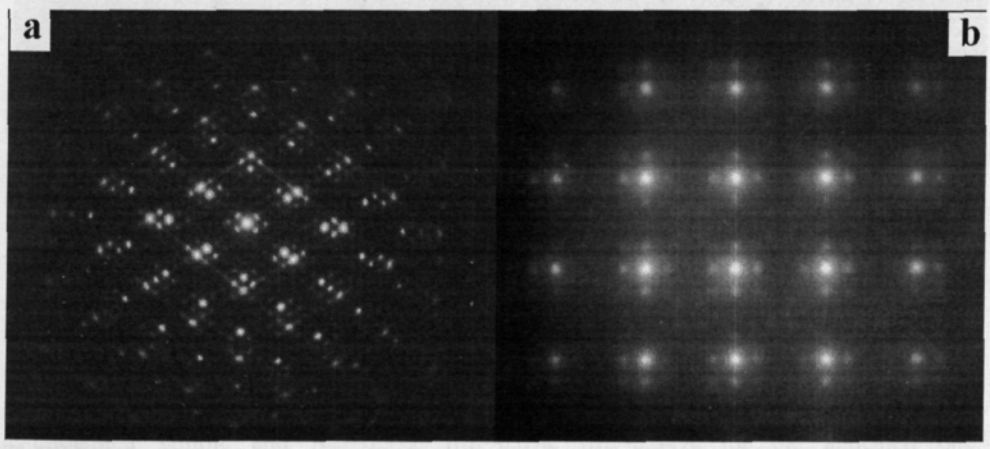

Figure 3.8 Electron diffraction patterns from the annealed sample a) in cross-section (buried layer) and b) in plan-view (both buried and top layers). There is presence of Si and β-SiC spots, and the orientation relationship between the two lattices is visible.

In these images, it is worth remarking the similar intensity of both Si and SiC spots. This gives a clear indication of the high crystalline quality of the SiC crystals, which is comparable to that of the Si network. The very good alignment between the two materials is also verified by the presence of a Moiré fringe pattern in the <111> directions. However, some small misalignments are visible in some of the precipitates.

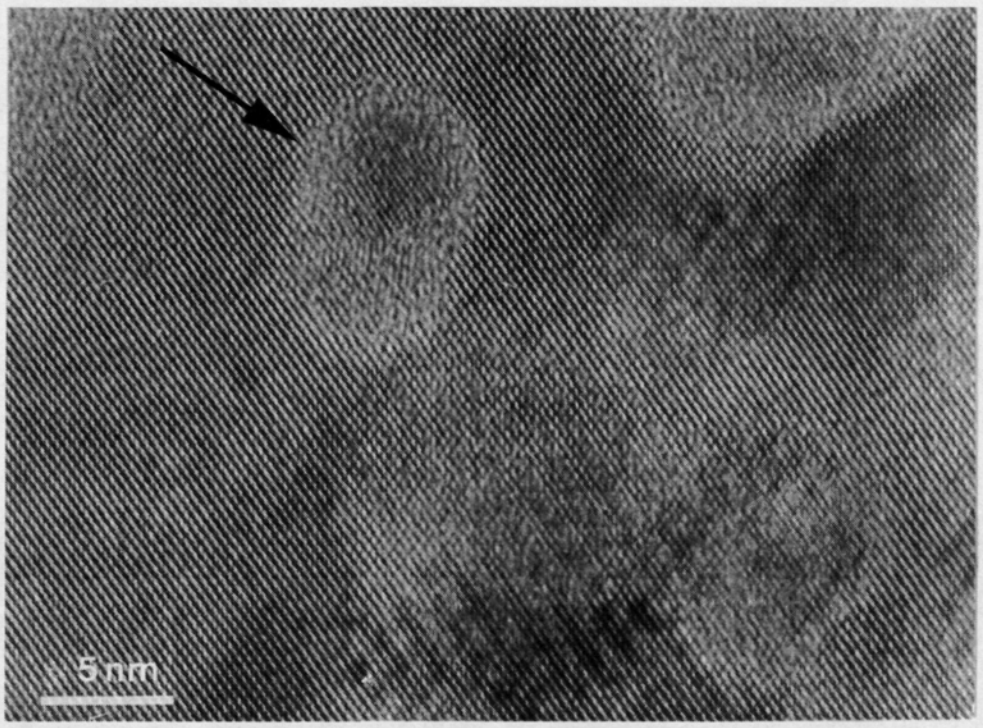

Figure 3.9 HREM image showing the β-SiC precipitates at the buried layer. Moiré fringes are caused by the overlapping of the two lattices and the resolved lattice of one of the precipitates. An arrow indicates the amorphous-like interface surrounding a precipitate.

With respect to the β-SiC precipitates, it is important to noticet that the images obtained by conventional TEM do not show any strain contrast around them. Furthermore, High Resolution TEM (HREM) images show that an amorphous-like region surrounds the precipitates as shown in figure 3.9.

From this result, it is possible to conclude that the β-SiC precipitates are well aligned with the Si lattice, but have incoherent interfaces to it and, thus, show no strain effects related to the mismatch between both lattices

In figure 3.9, a β-SiC grain is surrounded by an 'envelope' which shows no crystalline contrast. Probably, this envelope adapts the mismatch between both lattices, because β-SiC grows with almost its own lattice parameter. This fact could explain the reason why no strain contrast is visible around the grains. As already indicated, the grain size does not change with the annealing procedure. Assuming that the envelope is already formed after the implantation, it should move outwards in order to allow the grains to grow, which would involve the consumption of some crystalline Si.

However, this process is highly unlikely, as the Si lattice is quite stable with temperature. For this reason, the precipitates are almost of the same size before and after the annealing and only their crystallinity can change. An increase in the implantation dose would cause the grains to be closer and eventually SiC grains would coalesce in the buried layer. Furthermore, a very low density of defects is observed in the β-SiC precipitates, showing their very good quality. Only a few twins have been found in some of them. On the other hand, for the lower implantation doses (10^{17} cm^{-2}), the TEM results are similar to those of the higher implantation dose. A variation in the density of the precipitates is visible, as a consequence of the lower amount of C introduced and the lower C concentration at the implantation peak. Furthermore, the self-interstitial defects above the buried layer do not appear in the as-implanted sample.

The XRD measurements (θ-2θ scans) performed on the samples implanted at the highest dose show the presence of the (004) Si substrate peak, together with the (002) β-SiC peak, confirming the preferential orientation of the precipitates with the lattice. For the lower dose, no peaks corresponding to the SiC are visible, probably because the concentration of SiC is low. For the as-implanted sample, the (002) β-SiC peak intensity is quite low, while it strongly increases and slightly narrows for the annealed one, that corroborates the increase of crystallinity with the annealing shown by TEM and FTIR.

From the position of the (200), (111) and (220) peaks from 2θ-ω measurements, the strain in the SiC crystals has been estimated to be of about η_{200}=0.9%, η_{111}=0.6%, η_{220}=0.6% for the as-implanted sample and η_{200}=0.3%, η_{111}=0.6%, η_{220}=0.04% for the annealed one. Accordingly, the SiC crystals are under a positive strain that is partially relieved by the annealing process.

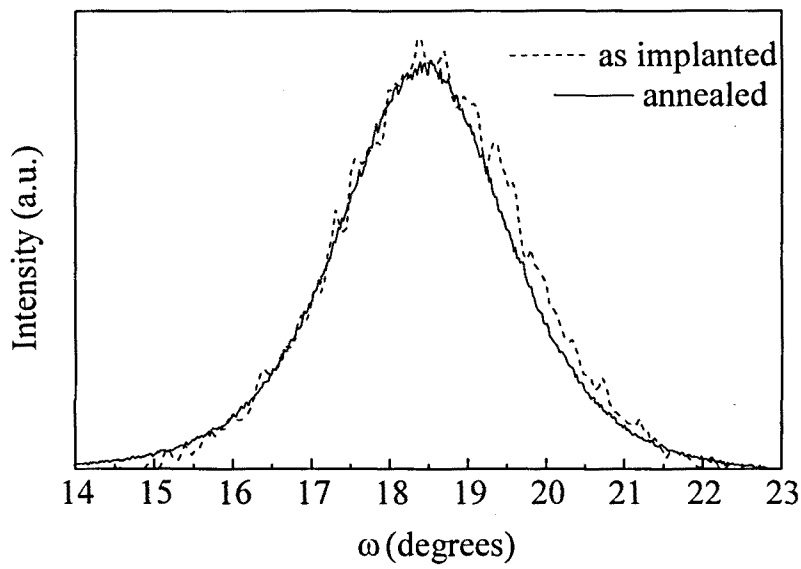

Figure 3.10 ω-scans performed on both samples around one of the {111} peaks, represented normalised to the peak intensity. The intensity of the sample annealed is about 10 times larger than that of the as-implanted one.

Moreover, ω- and Ω-scans have been performed around the (002), four {220} and four {111} β-SiC peaks from both, as-implanted and annealed samples. In order to estimate the degree of misalignment, the spectra have been fitted using a gaussian function. Again, the intensity of these scans is much lower for the as-implanted sample. The FWHM of the fitted gaussians, after a correction for the instrumental width, is about 2.9° after the implantation and reduces to 2.4° after the annealing. ω-scans performed around one of the {111} peaks are plotted in figure 3.10. Assuming that the FWHM gives the average misorientation of the crystallites around the peak position, β-SiC precipitates are interpreted to be oriented to the Si within an angle of about ±1.2°. This value is significantly lower than that reported by other authors[1,3], who report a FWHM of 4.8° and a misalignment of 3.5°. In both cases the implantation temperature was higher than the one used in this work (850-900°C) and no post-implantation annealing was performed.

To summarise, the analysis of the samples implanted at 500°C reveals that, in spite of the relatively low implantation temperature as compared to the conditions used by other authors[1,2], high crystalline quality β-SiC precipitates are directly formed in the buried layer. In comparison with previous works, SiC synthesised at 500°C shows a much lower density of defects as twins or voids, and a better crystalline orientation in relation to the Si lattice, with a lower misalignment. The high crystalline quality of the SiC grains is also related to the relatively low value of residual strain in the crystals, which contrasts with the very high lattice mismatch, of nearly 20%, between both cubic lattices of Si and β-SiC. This agrees with the absence of an epitaxial relationship between both Si and SiC lattices, as revealed by HREM. The high degree of crystalline orientation of the SiC crystals with the Si network has been explained assuming the existence of a simple topotactic transformation which implies the generation of four Si interstitials (Si_i) per unit cell[3]. These interstitials react with other C atoms forming β-SiC in the available empty space. Consequently, each Si atom is replace with a SiC molecule, and a Si unit cell is transformed into two β-SiC unit cells, which results in a volume increase of 3.25%.

In spite of the expected volume increase involved in this transformation, the presence of a positive (tensile) strain in the SiC crystals suggests that not all the Si interstitials are able to react with the implanted C atoms, and an excess of interstitials is injected from the buried layer leaving some empty space which causes tensile deformation of the SiC grains. This agrees with the observation of {113}-type defects in the Si regions above and below the buried layer, which are related to self-interstitial saturation in the Si network.

Injection of interstitials from the implanted layer is characteristic of high dose ion implantation processes and has already been observed[12] in Si wafers implanted at high doses with different species such as O or N. Thus, Si interstitials migrate from the implanted layer towards both upper and substrate Si regions, and the tensile strain in the SiC grains in the buried layer is accompanied by a compressive strain in the Si network. The annealing leads to a partial relaxation of strain in both Si and SiC networks, and the exceeding interstitials in the top Si layer can relax in the free surface of the sample. For the Si substrate region, the absence of a free surface where excess of interstitials can be accommodated causes the formation of dislocations.

3.2 ION BEAM SYNTHESIS OF SiC BY CARBON ION IMPLANTATION AT 500°C: STOICHIOMETRIC IMPLANTATION

The high crystalline quality of the β-SiC grains formed by substoichiometric C ion implantation into Si constitutes a very promising result for the ion beam synthesis of a continuous stoichiometric SiC layer. This experiment has been defined by taking into account the high stability of the C implanted profile and the absence of significant surface segregation or diffusion when the implantation is performed at 500°C. According to this, a four fold implantation process has been defined in order to achieve a 300 nm thick buried layer with a flat stoichiometric C profile. The implantation parameters have been defined by TRIM and figure 3.11 shows the simulated profile. The implanted doses were adjusted to obtain a constant stoichiometric SiC composition at the implanted region. This has been done in order to avoid the presence of an excess of C in the SiC layer. This excess can lead to a high density of C interstitials in the SiC crystals or to the formation of C precipitates. In both cases, the high stability of such defects in the SiC lattice would avoid their release by thermal annealing.

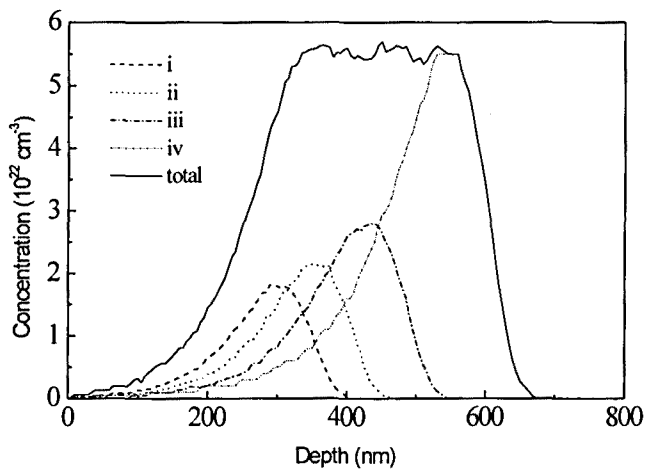

Figure 3.11 TRIM simulated profile of C^+ implanted in Si, at different energies and doses doses i) E_1= 100 keV, ϕ_1= 2.6x10^{17} cm^{-2}, ii) E_2= 120 keV, ϕ_2= 3.3x10^{17} cm^{-2}, iii) E_3= 150 keV, ϕ_3= 4.7x10^{17} cm^{-2}, iv) E_4= 195 keV, ϕ_4= 10^{18} cm^{-2}.

The implanted Si wafers were subsequently annealed for 6 hours at 1150°C under a N atmosphere. In agreement with the results presented in the previous section, the structural analysis of these samples reveals the direct formation of a β-SiC layer with abrupt SiC/Si interfaces, being this layer formed by SiC crystals with the same crystalline orientation as the Si network.

3.2.1 SPECTROSCOPIC DATA AND AFM RESULTS

The high crystalline quality of the implanted layer has been corroborated by FTIR. Figure 3.12 shows the FTIR spectrum measured in the annealed sample. It has a typical lorentzian shape, centred at 796 cm^{-1} and with a FWHM of about 50 cm^{-1}. These features are similar to those reported for single crystal β-SiC[9].

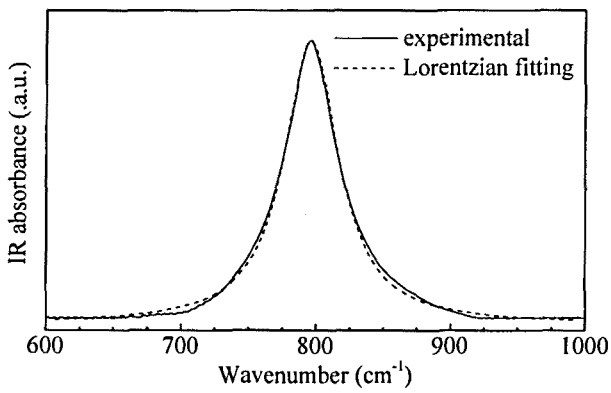

Figure 3.12 FTIR spectrum for the annealed sample.

The C in-depth profile has been measured by XPS and is plotted in figure 3.13 for both as-implanted and annealed samples. These measurements show the presence in the implanted samples of a thick flat C profile, stable under annealing, with a SiC stoichiometric concentration and sharp interfaces with the top Si and substrate regions. From these measurements, the thickness of the SiC layer is estimated to be of about 300 nm, while that of the top Si layer is of about 250 nm, what agrees well with the TRIM simulation.

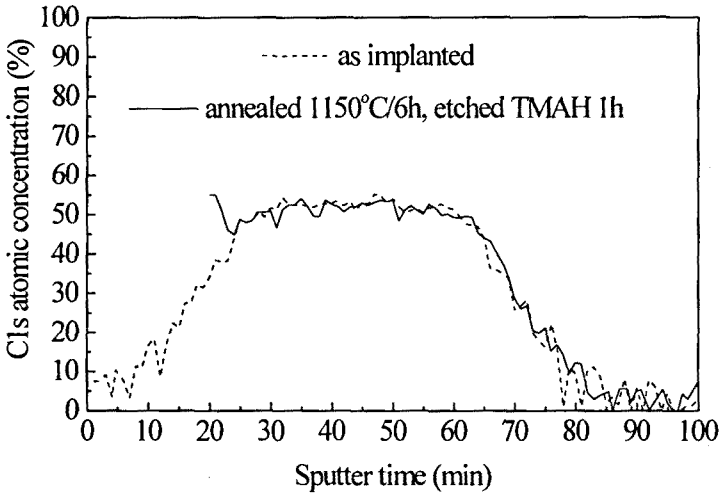

Figure 3.13 C and Si in-depth XPS profile for as-implanted and annealed samples.

The formation of a stoichiometric SiC film with abrupt SiC/Si interfaces can also be deduced from chemical etching experiments. The XPS profile in figure 3.13 from the annealed sample was measured after the removal of the top Si substrate by etching in TMAH (tetramethil ammonium hydroxide, at 25% wt and 80°C). TMAH is a well-known anysotropic etchant in Si technology with a higher compatibility with CMOS technology than other etchants such as KOH or etihylendiamine pyrocatechol (EDP) solutions.

The extreme chemical inertness of the SiC network causes a very high etchant selectivity of these solutions between Si, which is anysotropically etched, and SiC, which is almost not etched at all. Figure 3.14 shows an AFM image of the etched surface, which is characterised by a surface roughness value of about 6 nm (RMS). A similar surface roughness has been measured in the SiC/Si back interface. For this, the surface of the top Si layer was thermally bonded to a silica wafer, and the Si substrate was completely removed by chemical etching. These low values of surface roughness are related to the abruptness of both Si/SiC interfaces, as already suggested from the in-depth XPS measurements.

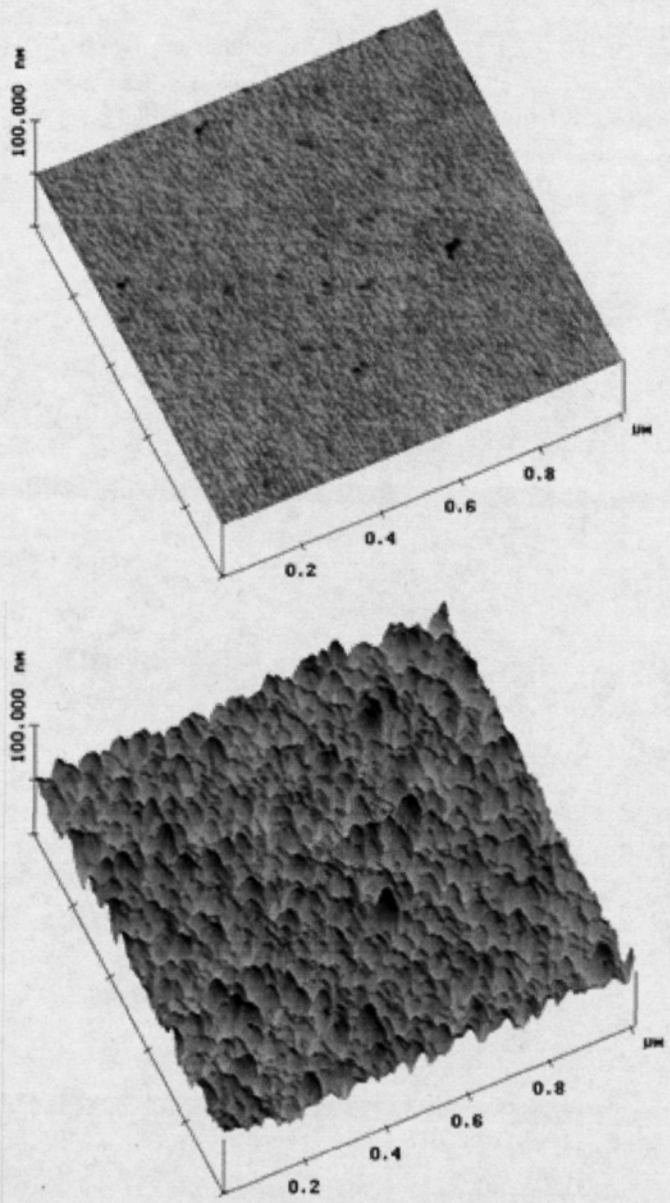

Figure 3.14 AFM images of the etched surface for the annealed sample (bottom) and a typical Si single-crystal surface (top).

3.2.3 TEM AND XRD ANALYSIS

The cross section TEM image of the annealed sample can be seen in figure 3.15. A compact buried layer with well-defined interfaces is clearly seen, because of the clear contrast between this layer and the upper damaged Si. This buried layer is formed by SiC crystals with sizes in the range of 5-10 nm.

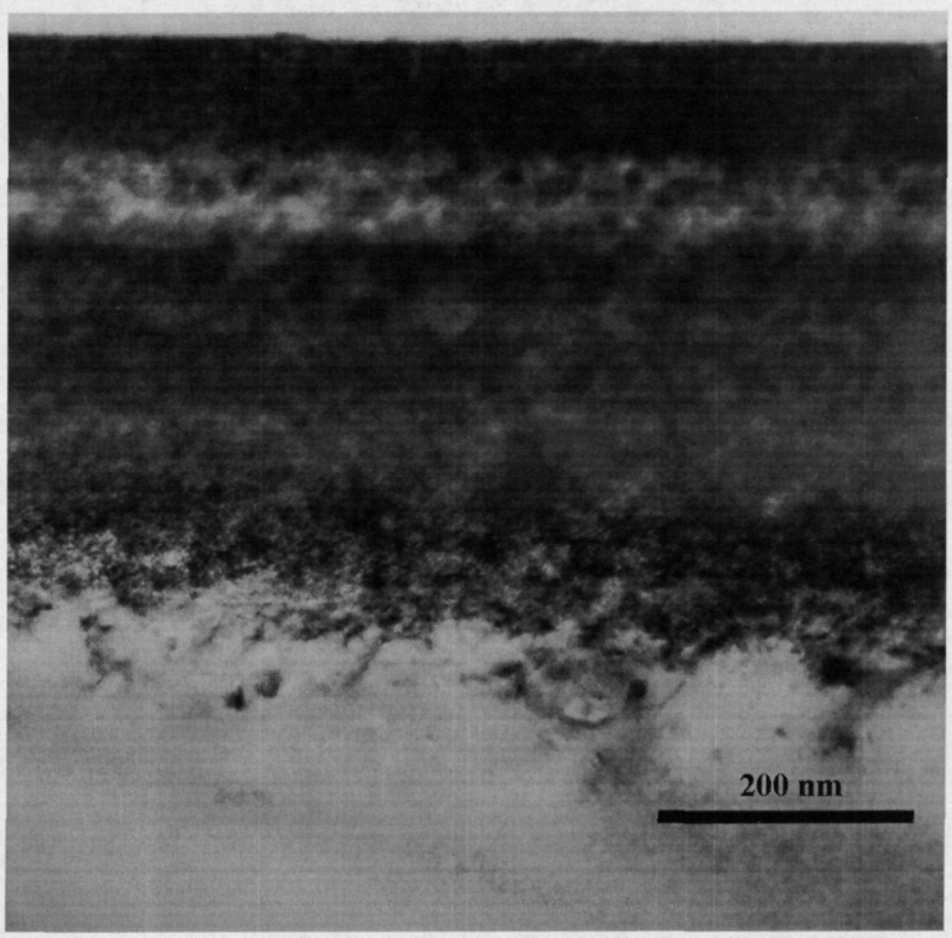

Figure 3.15 Cross-section TEM image of the annealed sample.

The crystalline orientation of the crystals is revealed from the TED pattern, shown in figure 3.16. In this case, only spots from the β-SiC network are observed, which corroborates the formation of a continuous SiC stoichiometric layer. Moreover, all the crystals have the same crystalline orientation, which corresponds to that of the original Si network.

As already observed in the previous section, no epitaxial relationship is found between the grains and an intergrain region with no crystalline contrast is seen. The nature of these amorphous-like intergrain regions, which are extremely thin, is not clear at all. In principle, Raman scattering measurements do not reveal any contribution in the C vibrational region, what suggests that these intergrain regions are not related to amorphous C.

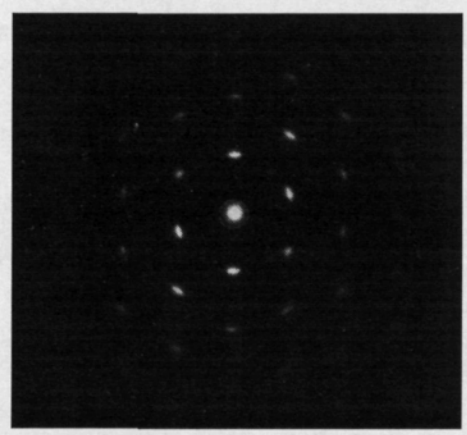

Figure 3.16 TED pattern in the buried layer of the annealed sample.

Finally, XRD measurements have also been performed to determine the residual strain in the SiC network as well as the average missorientation of the SiC crystallites. θ-2θ scans confirmed the preferential orientation of the precipitates within the lattice. From the position of the (200), (111) and (220) peaks, strain in the SiC crystals has been estimated to be of η_{200}=0.47%, η_{111}=-0.006%, η_{220}=0%. Accordingly, the SiC crystals are under a low positive strain. Moreover, ω- and Ω-scans have been performed around the (002), four {220} and four {111} β-SiC peaks.

In order to estimate the degree of misalignment, the spectra have been fitted using a gaussian function, with a FWHM of about 3.4°. Assuming that the FWHM gives the average misorientation of the crystallites around the peak position, β-SiC precipitates are interpreted to be oriented to the Si forming an angle of about ±1.7°.

Comparing with the data of the substoichiometric dose (described in section 3.1.3) it is worth remarking the significant release of strain observed in this case for (111) and (220) directions. This agrees with the result of Prewinkel et al[8] from samples implanted at different doses above and below the threshold value for stoichiometric composition. According to these authors, a transition from isotropic to uniaxial stress and strain occurs at the threshold dose for the formation of stoichiometric SiC films. For higher doses, strain and stress in lattice planes parallel to the surface nearly vanish, while in the normal direction a constant strain of 0.7-1% is observed in the as-implanted samples. This behaviour is suggested to be related to the coalescence of the SiC precipitates to a continuous stoichiometric SiC layer.

On the other hand, the formation of nanocrystals in the SiC buried layer could be related to the elastic energy accumulated in the layer[13]. According to the presented data, the topotactic transformation of the Si lattice to a SiC lattice is accompanied by a stress in the crystal, which is mainly tensile. This is probably related to an injection of interstitial Si from the implanted region, which is characteristic of high does ion implantation processes. The elastic energy accumulated in the grains can be partially released by the grain boundaries and according to this, the formation of a nanocrystalline layer is energetically more favourable than the formation of a simple crystal layer.

The high homogeneity of the SiC layers can also be detected from optical inspection of chemically etched wafers. Figure 3.17 shows a photography of a quarter of a 2" Si wafer which was implanted with a 1" circular diaphragm after annealing and etching in TMAH. The grey-black surface in the sample is etched Si, which is rough by the anisotropic etchant procedure, and the shiny green polished surface is the SiC layer. The homogeneity in the thickness of the layer and the low SiC/Si roughness can be inferred from the absence of any change in colour of this layer. Very small changes in thickness, as low as 10 nm, can be optically detected as changes in colour of the surface, because the colour of the thin layer on Si is extremely dependent on the thickness of the layer, due to interference effects.

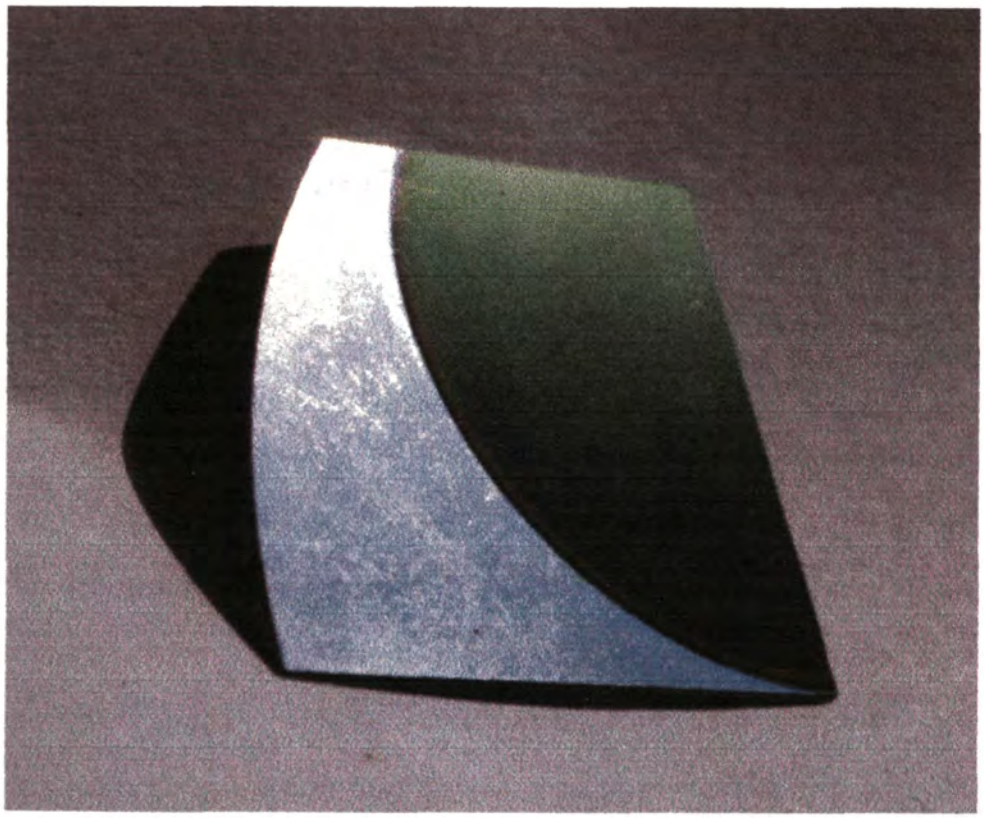

Figure 3.17 Photography of a quarter of a 2" Si wafer implanted with a 1" circular diaphragm after annealing and etching in TMAH.